ALBORÁN SEA SHELF HYDRODYNAMIC PROCESSES

Mª de los Ángeles Serrano García

Doctoral Thesis

ADVISOR:
Dr. Manuel Díez-Minguito

Programa de Doctorado: Dinámica de Flujos Biogeoquímicos y sus Aplicaciones. Departamento de Estructuras e Ingeniería Hidráulica
Universidad de Granada
Granada (España)

November 2016

A Carmen,
A Nacho,
A mis padres

La doctoranda María de los Ángeles Serrano García y el director de la tesis Dr.Manuel Díez Minguito, garantizamos, al firmar esta tesis doctoral, que el trabajo ha sido realizado por la doctoranda bajo la dirección del director de la tesis y hasta donde nuestro conocimiento alcanza, en la realización del trabajo, se han respetado los derechos de otros autores a ser citados, cuando se han utilizado sus resultados o publicaciones.

En Granada, a 4 de Noviembre de 2016,

Director de la Tesis

Fdo.: Dr. MANUEL DÍEZ MINGUITO

Doctoranda

Fdo.: MARÍA DE LOS ÁNGELES SERRANO GARCÍA

Summary

The Alborán Sea is a back-arc region located in the western Mediterranean Sea. This region is connected to the Atlantic Ocean through the Gibraltar Strait and opens to the east into the Balearic Basin through the Alborán Trough. In the Alborán Sea, oceanic motions involve a great variety of both spatial and temporal scales. The influence of tides, subinertial flow induced by atmospheric pressure gradients and wind stress, and the wind waves near the coast has been intensively studied. However, a detailed study of long-period waves, as Continental Shelf Waves (CSWs), propagating along the continental shelves of the Alborán Sea is still lacking. This type of waves propagates in one direction with the coast on the right (Northern Hemisphere). The presence of two narrow, opposite, and approximately parallel continental shelves provides an additional interest to the study site, because of the possible interaction of these kind of waves travelling in opposite directions. Then, this Thesis studies the existence of these waves in the continental shelves of the Alborán Sea. Another special feature of the Alborán Sea is that it is indented by transverse incisions. Some of these incisions are large enough to be considered submarine canyons. Several studies suggest that wind modifies the circulation in submarine canyons and drives cross-shore transports and vertical motions. However, little is known on the role of local atmospheric pressure gradients on the circulation of a submarine canyon. This Thesis also explores the role of this forcing in the circulation of a submarine canyon of the Alborán Sea, the Jolúcar canyon. Thus, the general aim of this Thesis is to study hydrodynamic processes over the continental shelves (northern and southern) of Alborán Sea (regional scale) and the local circulation in a submarine canyon indenting in the northern shelf. The objective is addressed using data analysis of field observations, and semi-analytical models.

The study of characterization and propagation of CSWs on the Alborán Sea was performed. A statistical approach was applied to determine both propagation direction and phase speed of free continental shelf waves. The

presence of a westward-travelling signal on the north continental shelf and a west-to-east travelling signal on the south continental shelf of the Alborán Sea was confirmed. Moreover, the cross spectra between residual sea level signals along Alborán Sea have showed significant coherence at long periods. Phase speeds of free CSWs were calculated from significant periods. There is evidence of a seasonal variation in the phase speed of the waves, which may be related to variations in the speeds of ambient currents in the Alborán Sea. The linearized long-waves equations governing hydrostatic motion of an inviscid, barotropic, coastal ocean on a Northern Hemisphere f-plane, including bottom friction and the bottom topography of Alborán Sea continental shelf, were used in the theoretical study. The main results were that the presence of bottom friction, alongshore wind stress, and atmospheric pressure gradient alter the structure of free Continental Shelf Waves. The results from this theoretical analysis have important implications for the construction of numerical models of shelf circulation,

The hydrodynamic processes inside a submarine canyon in the Alborán Sea were studied. Currents data of two field surveys, and measurements of atmospheric pressure and wind stress were analyzed. Spectral and Empirical Orthogonal Functions analyses were applied to identify the most energetic frequencies related to the main forcings and to obtain the relationship between the main dominant modes that drive the Jolúcar canyon circulation, respectively. Results indicated that local atmospheric pressure gradients induced 1/3 of the horizontal circulation in the submarine canyon. Internal waves with a period of about 25 minutes were identified, and were only observed during the daytime. These observations suggest the relationship between physical water motions by internal waves and zooplankton behaviour. A positive vorticity was observed at 30 m depth, which indicates the existence of the cyclonic circulation. Moreover, although two distinct layers were observed in the canyon water column, which indicates both down/ upcanyon flows, the net direction of the canyon flow was downcanyon. It might suggest that canyon might acts as an escape mechanism to any type of substances. The analytical model developed related the canyon circulation with both local wind stress and atmospheric pressure gradient. Thus, the classical analytical solution of wind-induced current profile was extended here by considering the superposition of bottom and surface Ekman layers, and including the influence of barotropic pressure gradients in a non-homogeneous water column. The analytical solutions proposed in this Thesis reproduce well

the main features of currents spatial structure associated with the wind and the local barometric pressure gradient.

Resumen

El mar de Alborán, situado al oeste del Mar Mediterráneo, se considera una cuenca semicerrada altamente dinámica, donde los movimientos oceánicos envuelven gran variedad de escalas espacio-temporales. Existen estudios acerca de cómo se comporta la marea, y también sobre el comportamiento de los flujos subinerciales inducidos por los gradientes de presión atmosférica y el viento. Sin embargo, no existe un estudio detallado de ondas de periodo largo, que se propagan longitudinalmente a lo largo de las plataformas continentales del mar de Alborán, como son las ondas de plataforma continental (CSWs). Éstas son un tipo de ondas atrapadas que se propagan dejando la costa a su derecha. Una primera particularidad de este mar, que aporta un interés añadido al estudio de este tipo de ondas, reside en la existencia de dos plataformas continentales estrechas, opuestas, y aproximadamente paralelas entre sí, de manera que existe una diferencia en el sentido de giro de las CSWs. En esta Tesis se estudia el comportamiento de dichas ondas en esta zona característica. Otra peculiaridad del mar de Alborán es la existencia de incisiones transversales, que en algunos casos poseen dimensiones suficientes para ser denominados cañones submarinos. La mayoría de los estudios realizados sugieren que el viento es el responsable de gran parte de la modificación de la circulación en los cañones submarinos. Sin embargo, no existe un estudio detallado acerca del papel que juega el forzamiento del gradiente de la presión atmosférica en la hidrodinámica de un cañón submarino. En esta Tesis se estudia el papel de dicho forzamiento en la circulación de un cañón submarino localizado en una de las plataformas continentales del mar de Alborán, el cañón de Jolúcar.

En resumen, el objetivo general de esta Tesis es estudiar la dinámica de los procesos hidrodinámicos a dos escalas: regional (plataformas continentales del mar de Alborán) y local (cañón submarino). Para alcanzar este objetivo se han combinado una serie de métodos analíticos y de análisis de datos observados.

En primer lugar, se estudió la caracterización y propagación de CSWs en el mar de Alborán. Para ello, se realizó un análisis estadístico que permitió determinar la cinemática de las CSWs libres, confirmando la presencia de una señal propagándose hacia el oeste en la plataforma continental norte, y otra señal hacia el este en la plataforma continental sur del mar de Alborán. Paralelamente, los espectros cruzados de las señales residuales del nivel del mar entre pares de estaciones indicaron la existencia de oscilaciones de periodos largos, los cuales se utilizaron para calcular las velocidades de fase de las ondas observadas. Además, se observó una variación estacional en las velocidades de fase de las ondas estudiadas, que podría estar relacionada con las variaciones en las corrientes del mar de Alborán. Por otra parte, a partir del análisis teórico, en el que se utilizaron las ecuaciones de conservación de momento y de masa que rigen la circulación barotrópica, incluyendo los términos de rotación y fricción de fondo, y teniendo en cuenta la topografía de fondo media del mar de Alborán, se estudió la respuesta de las CSWs al forzamiento meteorológico. A partir del análisis teórico, se obtuvo que tanto la fricción de fondo, como el viento y los gradientes de presión alteran la estructura de este tipo de ondas libres.

En segundo lugar, se analizaron los procesos hidrodinámicos de un cañón submarino del mar de Alborán mediante el análisis de datos. Además, para estudiar el papel del gradiente local de la presión atmosférica, se desarrolló un modelo analítico, cuyos resultados se compararon con los datos de las observaciones. El análisis de datos se realizó con datos de corrientes de dos campañas de campo, y con datos de viento y presión atmosférica. El tratamiento de las señales medidas incluyó el análisis espectral para detectar las frecuencias de las oscilaciones más energéticas y relacionarlas con los distintos forzadores, y el análisis de componentes principales para obtener los patrones de circulación bajo distintas condiciones. Los resultados de dichos análisis indicaron que los gradientes locales de presión atmosférica inducen 1/3 de la circulación del cañón. Además, se identificaron ondas internas con periodos de 25 minutos, que sólo se observaron durante el día. A partir de estos resultados se puede presuponer que existe una relación entre el comportamiento del zooplancton y las ondas internas. Por otra parte, se estudió la vorticidad, observando la existencia de una vorticidad positiva en el cañón submarino a 30 m de profundidad, que indica la existencia de una circulación ciclónica, que coincide con la profundidad de la picnoclina. Finalmente, los resultados del modelo teórico, que incluye la solución clásica de Ekman, considerando la superposición de las capas superficial y de fondo de Ekman, e incluyendo la influencia de los gradientes de presíon en

una columna de agua no homogénea, reproducjeron bastante bien la estructura espacial de las corrientes observadas en el cañón submarino.

Agradecimientos

Quisiera agradecer al Grupo de Dinámica de Flujos Ambientales, por el apoyo económico recibido para realizar mis estudios de doctorado.

En primer lugar a Miguel Ángel Losada. Nunca imaginé que en Julio de 2012 te conocería y cambiarías el rumbo de mi vida profesional. Gracias Miguel, por haber confiado en mí y darme la oportunidad de trabajar contigo, por dedicarme tu tiempo enseñándome y compartiendo todos tus conocimientos y experiencia acumulada, y sobretodo por abrirme las puertas a este mundo que me fascina. Ahora soy una manchega enamorada del mar! Los dos sabemos que esta tesis no hubiera sido posible sin tus ideas y ayuda incondicional.

Gracias también a mi director de tesis, Manuel Díez-Minguito, por su inestimable ayuda. Manolo, gracias por darme tu apoyo y compañía durante todos estos años. Es un placer poder compartir contigo cada resultado que hemos ido obteniendo , afrontándolos con entusiasmo y mucha ilusión. Gracias por tus buenos consejos y todas tus ideas, cuya aportación ha sido fundamental para el desarrollo de este trabajo.

Quisiera agradecer también a Arnoldo Valle-Levinson por contribuir de manera significativa en el contenido de esta tesis. Arnoldo, es un placer trabajar contigo. Gracias por todas tus aportaciones, explicaciones, y por todo el tiempo que me has dedicado para poder llevar a cabo este trabajo.

A todos mis compañeros del Grupo, gracias por los buenos momentos que pasamos juntos. A Miguel Ortega, gracias por tus observaciones y críticas constructivas durante la preparación de los artículos. Manuel Cobos y Miguel Reyes, gracias por vuestra ayuda desinteresada y por todo vuestro apoyo durante todo este tiempo.

Finalmente, agradecer a mi familia, que representa lo más importante de mi vida, y en especial a ti, Nacho; bien sabes que te doy las gracias por hacerme las cosas más fáciles y apoyarme en cada momento. Gracias por estar ahí.

Y como no, a ti, lector, gracias por continuar leyendo esto que, de alguna manera, indica que estás interesado en saber lo que pienso.

Cabo de Sacratif, Granada

Peter Bojthe

"Ningún mar en calma hizo experto a un marinero"

Anónimo

Contents

References   112

List of Figures

List of Tables

1

Introduction

1.1 Context and Motivation

The Alborán Sea is a back-arc region located in the western Mediterranean Sea (Figure 1.1). This region is connected to the Atlantic Ocean through the Gibraltar Strait and opens to the east into the Balearic Basin through the Alborán Trough [1]. Alborán Sea corresponds to a domain developed from the early Miocene to the present under a convergence regime as a consequence of the continental collision between African and European plates [1, 2]. Thus, this region has developed a complex physiography [3]. Moreover, this tectonic shortening and the progressive emergence of segments of the ancestral Alborán basin have reduced the basin to a 400 - 200 km low straddling the African and Eurasian plate boundary [3]. Similar to many other sub-basins, the Alborán Sea is highly dynamic, featuring complex interactions from tidal, atmospheric, and mixing processes [4]. In the Alborán Sea, oceanic motions involve a great variety of both spatial and temporal scales. The Atlantic Jet that enters in the Alborán Sea through the Strait of Gibraltar forcing the hydrodynamic processes in Alborán Sea [5], and the circulation regime of both the Western and Eastern Anticyclonic Gyres of the Alborán Sea were studied in detail [4, 6, 7]. The tides are

semidiurnal and mainly co-oscillate with the Atlantic waters, which propagate into the Alborán Sea through the Gibraltar Strait [8] (Figure 1.2, ordinary tides waves). Subinertial flows induced by atmospheric pressure gradients and water mass distributions generated by the wind action were investigated by Lafuente et al. [9] and Bárcenas et al [10], respectively. The influence of the wind waves near the coast, which are typically generated during the passing of extratropical storms, has also been intensively studied [11] (Figure 1.2, wind, and wind and ordinary gravity waves).
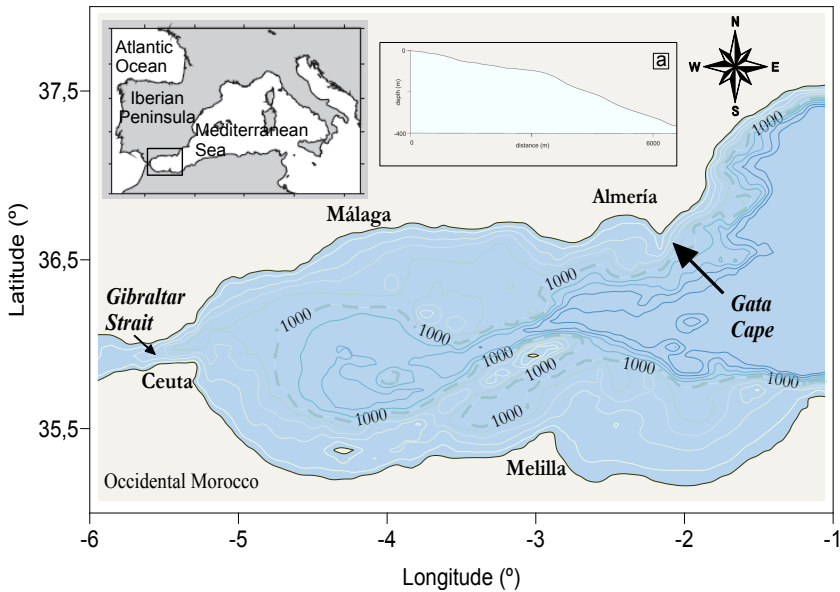
Figure 1.1: Contour map of the Alborán Sea showing the bathymetry. The dashed line indicates the base of the continental slope. Mean bottom topography of the northern continental shelf is shown in the inset panel (panel a).

However, a detailed study of long-period waves propagating along the continental shelves of the Alborán Sea is still lacking (Figure 1.2, shaded area). Among these long-period waves, coastal trapped waves (CTWs) are a subclass of waves that are characterized by a roughly exponential decrease in the amplitude of dynamic pressure anomalies with increasing distance from the coastline [12–15]. There are several types of trapped wave theories that have arisen, each corresponding to an idealized situation of stratification and bottom topography [16]: three barotropic homogeneous types (barotropic Kelvin waves, edge waves,
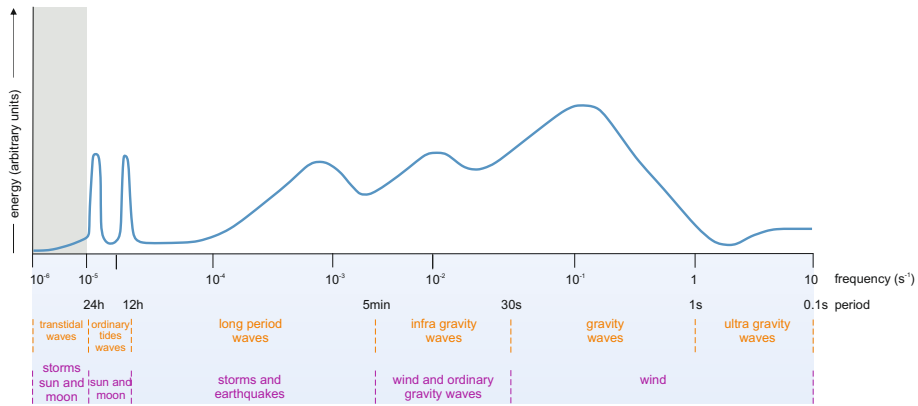
Figure 1.2: *Classification of the qualitative ocean waves power spectrum according to wave period recreated from Shaded area indicates long waves generated in the continental shelf.*

and continental shelf waves) [17], and two baroclinic types (internal Kelvin waves and general coastal trapped waves that are a hybrid of types) [18]. Barotropic Kelvin waves are long-period waves that lean against the edge of the basin over a flat bottomed homogeneous ocean, and typically generate geostrophic currents. As a result of the Coriolis balance, a Kelvin wave can only propagate in one direction, where the coast lies to the right of the propagation direction (Northern Hemisphere, HN). Edge waves are waves that propagate over a sloping bottom and are superinertial. Then, since rotation is not as important for edge waves, they can propagate in both directions along the coast from the source of generation. Continental shelf waves (CSWs) are subinertial waves that propagate over a sloping shelf and slope. These waves are restored by conservation of potential vorticity. CSWs also propagate, like Kelvin waves, in one direction with the coast on the right (Northern Hemisphere). Internal Kelvin waves are similar to their barotropic variety but they propagate over a stratified water column [18]. General CTW develop over a sloping bottom with a stratified water column, and they are a hybrid of CSW and internal Kelvin waves. This Thesis studies the existence of CSWs in the continental shelves of the Alborán Sea. The presence of two narrow, opposite, and approximately parallel continental shelves provides an additional interest to the study site, because of the possible existence of CSWs travelling in opposite directions.

Furthermore, the presence of mountain ranges surrounding the entire northern margin of the Alborán Sea (Figure 1.3 a) affect the shape of the continental shelf, generating deltas and river mouths. Therefore, another special feature of Alborán Sea is that it is indented by transverse incisions at regular

intervals. Some of these incisions are large enough to be considered submarine canyons.

The location of these canyons is shown in Figure 1.3 a, and their main characteristics are shown in Table 1.1. Submarine canyons of the Alborán Sea, particularly those located in the western basin, are relatively small when compared with the great oceanic submarine canyons formed off major deltas [19].
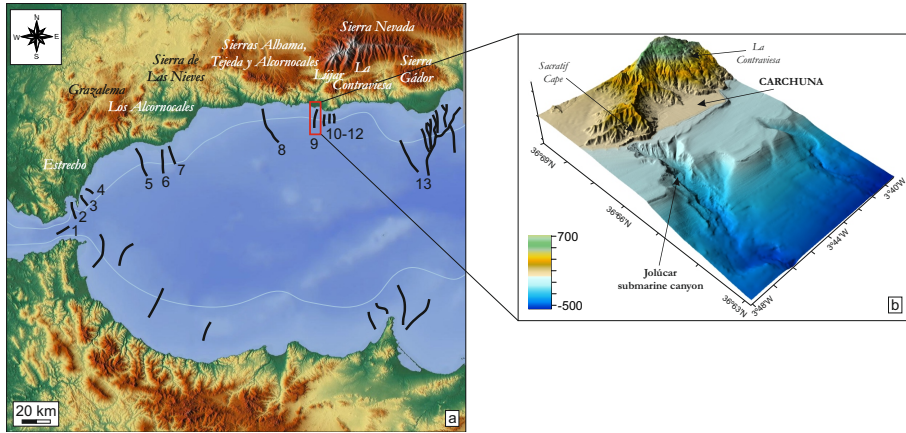
Figure 1.3: *Panel a: Location of both Andalusian mountain ranges and submarine canyons in the Alborás Sea (black lines). Labels 1-9 represent La Línea (1), Guadiaro (2), Guadalmina (3), Torrenueva (4), Fuengirola (5), Torre del Mar (6), Salobreña (7), Motril (8), Jolúcar or Sacratif (9), Calahonda (10-12), and Adra (13) submarine canyons. Blue line indicates the base of the continental shelf. Panel b: Location and bathymetry of the Jolúcar submarine canyon.*

Table 1.1: *Characterization of submarine canyons of northern Alborán Sea.*

Submarine canyon	Lenth (km)	Width (km)	Depth (m)
La Línea	9	0.7	650
Guadiaro	10	1.5	625
Guadalmina	13	0.7	675
Torrenueva	9	1	700
Fuengirola	12	1.5	625
Torre del mar	28	$--$	700
Salobreña	11	$--$	600
Motril	7	1.1	450
Jolúcar	8	1.7	600
Calahonda$_1$	2.5	0.9	300
Calahonda$_2$	1	0.9	300
Calahonda$_3$	1	0.5	300
Adra	55	0.7	600

In general, they are < 13 km in length and lack major tributaries, excepting the Almería canyon, which has a maximum length of 55 km and numerous tributaries. However, these submarine canyons constitute one of the drainage networks with the greatest number of canyons per km^2 in the Mediterranean Sea [19]. Submarine canyons modify the local circulation and enhance or inhibit cross-shelf exchange [20–22]. Several studies have investigated the circulation in submarine canyons at different locations around the world [23, 24]. Freeland and Denman [25] proposed that up-canyon flow could be driven by the cross-shelf pressure gradient that is in geostrophic equilibrium with the along-shelf current. However, Kaempf [26], using a hydrodynamic model to study wind-driven upwelling flow near a canyon, found that the geostrophic adjustment to barotropic pressure gradients drive up-canyon flow, and not the ageostrophic flow driven by a cross-shelf pressure gradient. She and Klinck [27] applied a numerical model to describe the circulation over submarine canyons driven by constant up/downwelling wind stress. They found that, during upwelling winds, near surface flow crosses over a canyon, while a closed cyclone occurs within the canyon. In contrast, downwelling winds create nearly the opposite flow, with an anticyclone within the canyon. Field studies have examined the upwelling over a number of shelf break canyons [28, 29], whereas laboratory models have been used to study wind-driven flow in canyons [30]. These studies suggested that wind modifies the circulation in submarine canyons and drives cross-shore transports and vertical motions [31]. However, little is known on the role of local atmospheric pressure gradients on the circulation of a submarine canyon. This Thesis also explores the role of this forcing in the circulation of a submarine canyon of the Alborán Sea. In particular, the study site is Jolúcar submarine canyon, also known as Carchuna or Sacratif canyon, near Carchuna beach (Granada) (Figure 1.3 b). It is a 8 km long canyon that trends N-S and ends seaward at a water depth of about 600 m. Jolúcar canyon has two main tributaries, which cut the shelf, and extend from water depths of 10 m to approximately 180 m. The study area is influenced by micro-tidal conditions, essentially semi-diurnal (tidal range of approximately 0.5 m). Hence, the main factor expected to force the circulation in the submarine canyon is atmospheric forcing, i.e., wind stress and atmospheric pressure gradients. The study site is often affected by extratropical Atlantic and Mediterranean storms, which generate wind waves under limited fetch conditions (approximately 300 km) from wind speeds of ~18 to 22 m/s. The predominant wind directions are east- and westward and the average wind speed is about 5.5 m/s [32]. The

presence of mountain ranges aligned with the coast in the vicinity of the study area (Figure 1.3) affect the local atmospheric dynamics [33]. The impact of wind and atmospheric pressure on the hydrodynamics of the study site was already highlighted by [11] and [34]. Nevertheless, those studies focused on waves in the nearshore area, away from the submarine canyon. Therefore, the characterization of this region is continued in this Thesis.

This Thesis contributes to the understanding of both local and regional hydrodynamics processes of the continental shelves and, in particular, Alborán Sea continental shelves. Therefore, it helps to develop an integral management of the study area.

1.2 Objectives

The aim of this Thesis is to study hydrodynamic processes over the continental shelves (regional scale) and a the local circulation in a prototypical submarine canyon in the northern Alborán Sea shelf. The objective is addressed using data analysis of field observations, and the development of analytical models from the hydrodynamic governing equations.

In order to reach this overall goal, four research questions are addressed:

1. Are there free long-period trapped waves propagating along the continental shelf of the Alborán Sea?

2. How do free long-period trapped waves propagating along the continental shelf of the Alborán Sea respond to different external forcings?

3. What are the main hydrodynamic processes in the Jolúcar submarine canyon?

4. What is the frequency range of the main hydrodynamic processes in the Jolúcar submarine canyon?

1.3 Outline of the Thesis

Apart from the Introduction (Chapter 1), this Thesis is organized into three parts, in which the above questions are addressed to achieve the general objective.

Part I is devoted to identify and characterize Continental Shelf Waves propagating along continental shelves of the Alborán Sea. Data from observations and a theoretical study are used in order to analyze the main dynamic characteristics of this type of waves. This part is comprised by Chapter 2.

Part II presents the study of hydrodynamic processes of a submarine canyon in the Alborán Sea. This part is comprised by four chapters. Chapter **??** provides

a brief introduction and the state of art. Chapter 3 includes the scaling analysis of Jolúcar canyon and also describes the theoretical flow dynamics of a narrow canyon. Chapter 4 is dedicated to study the atmospheric forced response of circulation in the submarine canyon using observational data and an analytical model. Chapter 5 studies both internal waves and vorticity in the submarine canyon from observations.

Part III presents the main conclusions and suggestions for future research. This part includes Chapter 7.

Finally, appendices contains additional aspects about the different analysis approach, the analytical derivations, and the technical information of the field surveys. These appendices complete the information included in each chapter.

1.4   Publications derived from this Thesis

Journal Papers

- Serrano, MA., Díez-Minguito, M., Ortega-Sánchez, M. and Losada, M.A, (2015). Continental shelf waves on the Alborán sea. *Continental Shelf Research* 111, pp. 1-8. Review article.

- Serrano, MA., Díez-Minguito, M., Ortega-Sánchez, M., Valle-Levinson, A., and Losada, M.A, (2016). Dependence of the circulation in a submarine canyon on the local atmospheric pressure gradients. *Geophysical Research Letters.* (Under review)

- Serrano, MA., Díez-Minguito, Valle-Levinson, A., and Losada, M.A. Superinertial Internal Waves characterization in a narrow submarine canyon in the Alborán Sea. (Under preparation)

Proceeding in international conferences

- Serrano, MA., Bergillos, RJ., Díez-Minguito, M., Ortega-Sánchez, M., and Losada, M.A, (2015). The effects of shelf-indenting canyons in the propagation of long waves: the case of the Jolúcar canyon (Granada, Spain). *ASLO Aquatic Sciences Meeting.* Granada, Spain.

- Serrano, MA., Díez-Minguito, M., Ortega-Sánchez, M. and Losada, M.A, (2015). Estudio de la caracterización y propagación de ondas de plataforma continental en el suroeste del mar Mediterráneo. *Simposio Internacional sobre el Margen Ibérico Atlántico* (MIA). Málaga, Spain (in spanish).

- Serrano, MA., Díez-Minguito, M., Ortega-Sánchez, M. and Losada, M.A, (2016). Tidal and atmospheric induced circulation in a Mediterranean submarine canyon: Observations and theoretical modeling. *Physics of Estuaries and Coastal Seas Conference*. Scheveningen, The Netherlands.

Proceeding in national conferences

- Serrano, MA., Díez-Minguito, M., Ortega-Sánchez, M. and Losada, M.A, (2016). Influence of atmospheric pressure on the circulation of a submarine canyon. *Trobades Cienífiques de la Mediterrania*. Spain

Part I

HYDRODYNAMICS PROCESSES IN THE CONTINENTAL SHELF

2

Continental Shelf Waves in the Alborán Sea

In this chapter, Continental Shelf Waves are identified and characterized on the Northern and Southern continental shelves of the Alborán Sea. Data from sea level gauges and meteorological stations along the continental margins are analyzed with a statistical approach. In addition, a theoretical study, using the linearized long-waves euations governing hydrostatic motion of an inviscid, barotropic, coastal ocean on a Northern Hemisphere f-plane, is applied to know how free continental shelf waves respond to different forcings.

2.1 Introduction and state of art

Continental Shelf Waves, CSWs, also called topographic Rossby waves trapped over the continental margin, are a subclass of so-called coastally trapped waves. These waves are characterized by a roughly exponential decrease in the amplitude of dynamic pressure anomalies with increasing distance from the coastline [12, 13, 15]. CSWs arise as a consequence of the conservation of potential vorticity in presence of a sloping seabed, and are generated by large-scale ($\mathcal{O}$ (100

km)) weather systems moving along or across the continental shelf, which have a period of a few days and comparable spatial variation [35–39].

CSWs typically exhibit amplitudes on the order of centimeters, periods on the order of one to several days, and wavelengths of tens to hundreds of kilometers, depending on the continental shelf width and slope [37, 40]. Consequently, these oscillations have small amplitudes, low frequencies ($\omega \gg f$, where f is the Coriolis parameter), and long wavelengths ($l \gg L$, where L is the width of the shelf/ slope region). Their phases travel parallel to the coast in only one direction, similar to classical Kelvin waves: in the Northern Hemisphere they travel with their right shoulder against the coast [41]. Figure 2.1 shows an example of a CSW propagating over a continental shelf in the Northern Hemisphere. An infinite number of modes are possible. The first mode has a node at the edge of the shelf and an anti-node at the coast. For higher modes, there are other nodes and anti-nodes at intermediate distances. The wave celerity for each mode, $c = \omega/l$, depends only on the shelf width and Coriolis parameter. Since the wave celerity does not depend on the frequency, the waves are non-dispersive. CSWs can travel long distances, for thousand of kilometres [42], influencing water levels and ocean dynamics far away from their generating region [12].
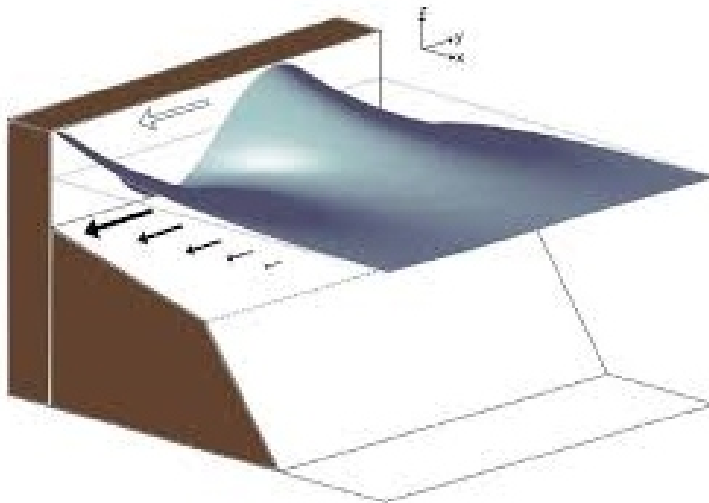
Figure 2.1: *An example of a CSW in the Northern Hemisphere by Pearce [16] , recreated from [64] . The direction of phase propagation is shown by the white narrow along the coast. The water velocity under the crest of the waves is indicated by the black narrows. The vertical displacement of the sea surface is greatly larger in the figure, as in the ocean CSWs amplitudes range is only in the order of centimeters.*

Continental Shelf Waves CSWs were first detected by Hamon [43–45], who showed that sea level did not respond isostatically to atmospheric pressure on the east coast of Australia sea level. That is, an increase of 1 mbar in atmospheric pressure did not necessarily correspond to a decrease in sea surface of 1 cm, as would be expected for static deformations [38]. Specifically, he found that sea level at different stations along the Australian coast was depressed only by about half the expected amount. He also effected a cross-spectral analysis between different coastal stations along the East Australian coast and found that for period longer than 3 days there was a time lag between the adjusted sea level variations at these points on the coast. These results suggested the presence of a low-frequency, non-dispersive left-bounded wave travelling northward along the continental shelf. Robinson [35], using a dynamical model with a shelf topography similar to the Australian coast, showed that the non-barometric sea level behaviour could be related to a resonant response of the adjusted sea level to pressure fluctuations of large scale moving weather systems, and introduced the concept of continental shelf waves [38]. This work generated widespread interest in the topic of CSWs and their presence has been reported on different continental shelves around the world. Thus, the existence of CSWs has been verified by analysis of observations of surface elevation and currents, for example, in the Atlantic coast of Canada [39]), West coast of EEUU ([46]), in the southern Weddell sea [47], the west coast of Scotland [48], and in the Florida coast [49]; by theoretical studies (e.g., [50–52]); and by numerical simulations [53]. Nevertheless, to our knowledge, no studies have examined the presence of CSWs on the continental shelf of the Alborán Sea. This study area is interesting because it features two opposite and approximately parallel continental shelves that are relatively close to each other , which connect at the Gibraltar Strait and open the possibility of interaction between outgoing and incoming CSWs.

Early on, the generation of CSWs was attributed to changing distrubutions in atmospheric pressure [35, 36]. Shortly after, the surface friction of the alongshore wind stress component associated with weather systems acting over a variable-depth shelf was revealed as being the dominant generating mechanism, over atmospheric pressure perturbations [38, 54, 55]. Thus, Gill and Schumann [56] developed a model to investigate the response of coastal currents and sea level to the alongshore wind stress. Their model showed that the first cross-shelf mode of a shelf wave out of an infinite number of modes is typically the dominant expression.

In addition to being an important component of the shelf dynamics [57], the presence of shelf waves may affect coastal ecosystems through enhanced upwelling [58]. Moreover, the results from Weber and Drivdal [59] indicate that these waves can induce a Lagrangian drift that could be relevant for the transport of particulate matter or pollution along the coast [52]. Then, CSWs can have important impacts on the marine bio-resources in the coastal regions. Therefore, the results of this chapter can be very important from both physical and biological aspects.

The purpose of this chapter is to identify and characterize the CSWs on the continental margins of the Alborán Sea using both data from sea level gauges and meteorological stations along the northern continental shelf (NCS) and the southern continental shelf (SCS), and a theoretical study. The specific objectives are the following: 1) to verify the existence of CSWs in the study site; 2) to observe the CSWs using data analyses; 3) to know the main characteristics of the CSWs; 4) to study the theoretical properties of the CSWs analyzing how free CSWs respond to different forcings. Therefore, in this Part I the research questions 1. and 2. defined in section 1.2 are answered to achieve the main goal of this Thesis.

2.2 The Study Area

As mentioned in Chapter 1, the study are of this chapter is the Alborán Sea. In studying the CSWs in the coast of the Alborán Sea, special attention must be paid to the topographic and weather characteristics in this area.

The study area includes both the North continental shelf NCS and South continental shelf SCS of the Alborán Sea (Figure 2.2). The Alborán Basin is narrow and reaches depths of 2000 m. The average NCS is approximately 20 km wide and widens at the far ends, although in some places the width decreases substantially, such as off Cabe Sacratif [1]. In the southern Alborán Sea, the continental shelf is approximately 20-60 km wide between Occidental and Oriental Morocco (Figure 2.2). The climate regime in the Alborán Sea provides a contrast between both the Atlantic and Mediterranean weather systems [60]. The Atlantic weather systems travel from west to east. The time scale is from 2-4 days to 2 weeks, and the predominant wind direction is eastward [61]. The Mediterranean weather systems are typically smaller and shallower than Atlantic systems and have shorter lifetimes [62]. They are generated between the Alborán Sea and North Africa; the time scale is approximately 2-4 days; and the predominant winds blow westward. Summer months are very dry, due to the influence of the Azores anticyclone. In contrast, average precipitation increases during autumn-winter,

in relation to the arrival of Atlantic fronts and to less extend of Mediterranean depressions.
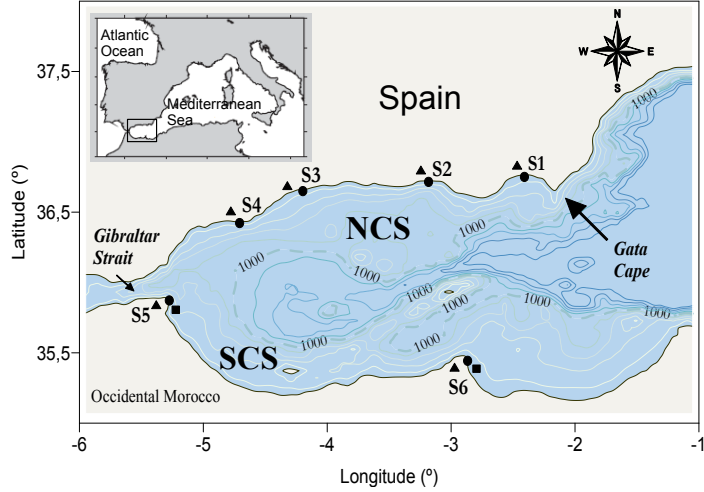
Figure 2.2: *Contour map of the Alborán Sea showing the bathymetry. The dashed line indicates the base of the continental slope. Labels NCS and SCS indicate the Northern Continental Shelf and Southern Continental Shelf, respectively. Circles, squares and triangles indicate the stations for sea level, wind, and atmospheric pressure observations, respectively (the NCS triangles include both wind and atmospheric pressure data). Labels S1?S6 represent the Almería (S1), Motril (S2), Málaga (S3), Estepona (S4), Ceuta (S5), and Melilla (S6) stations.*

2.3 Long waves propagation

The study of the characterization and propagation of CSWs was realized using both observational data analyses and a theoretical study.

2.3.1 Observations

The existence of free continental shelf waves in the Western Mediterranean sea was studied using hourly from six sea level gauges located along the northern and southern coastlines of the Alborán Sea (Figure 2.2, circle). Data were provided by *Puertos del Estado* (Ministerio de Fomento, Spain) and *Instituto Hidrográfico de la Marina* (Spain), hereafter *PdE* and *IHM*, respectively. The atmospheric pressure (Figure 2.2, triangle) was measured every six hours by the meteorological stations of the *Junta de Andalucía* (*Consejería de Medio Ambiente*, Spain), hereafter *JA-CMA*, located near the sea level stations. In the NCS, wind direction and velocity data (at three hour intervals) (Figure 2.2, square) were obtained from observations of the meteorological stations of the *JA-CMA*, which

were located near the sea level gauges. In the SCS, wind data (at three hour intervals) were obtained from the nearest hindcasting points of the model SIMAR (also provided by *PdE*). The analyzed time interval (2011-2012) was limited by the availability of simultaneous data records. Missing data for intervals of less than 12 hours in all series were completed by linear interpolation. Weather data were interpolated to hourly intervals.

The data record chosen for the analysis extends from June 19 to September 19 (hereafter referred to as *P*1 (2209 data points)) and from September 19 to December 19 (hereafter referred to as *P*2 (2185 data points)). *P*1 represents the summer season and *P*2 the autumn/winter season. These intervals were selected because they typically exhibit different meteorological and oceanographic conditions, in the sense of the influence of the different storms entering the region, the dominant wind magnitude of the winds, and the different surface current patterns controlled by the Atlantic water inflow.

Standard harmonic analyses were applied to the sea level data [63] to remove the tidal effects. A fifth zero-phase Butterworth low-pass filtering with a cut-off frequency of 0.9 cpd was performed to remove the remaining high-frequency oscillations. The filtered signals η were adjusted for the effect of the atmospheric pressure on sea level according to the hydrostatic approximation to eliminate the assumed in-phase effect of atmospheric pressure variations on sea level [64]. By calculating the spectral transfer function (hereafter referred to as *TF*) between the input alongshore wind stress and the output adjusted sea level η_{adj}, the wind-coherent signals were removed and then, the residual sea level was examined [65, 66].

The existence of travelling waves was revealed from correlation functions of the lagged cross-correlation, *CC*, between the residual sea levels at various stations by the existence of time lags that correspond to the maximum correlation.

The relationship between the residual sea levels η_{res} at the different stations was expressed in terms of both the coherence squared Φ^2 and the phase difference τ as a function of the frequency (cpd). This provided correlations and time displacements between the data records. The phase shifts were interpreted as lag times using $\tau(\omega) = \theta(\omega)/\omega$, where θ is the phase difference expressed in degrees at frequency ω. The observed phase velocity c at any given frequency was obtained from the phase shift via the equation $c(\omega) = D/\tau(\omega) = \omega D/\theta(\omega)$, where D is the along-shore distance between stations (km) (Figure 2.2).

The 95 % statistical significance level for the squared coherence was also determined. The spectral analysis of the data was performed by applying a

Fast Fourier Transform, averaged with the Welch method, and smoothed using a Hanning window. The input data were used with a Hanning window of length 631 points and a 50 % overlap.

The detailed description of different analysis procedures is found in the Appendix A.

2.3.2 Theoretical analysis

For the purpose of this chapter, the basic characteristics of CSWs on the coasts of the Alborán sea were determined by the linearized long-waves equations governing hydrostatic motion of an inviscid, barotropic, coastal ocean on a Northern Hemisphere f-plane. Making the rigid approximation, the linear shallow water equations become

$$-fv = -g\frac{\partial \eta}{\partial x} + \frac{\tau_x^w}{\rho H} \tag{2.1}$$

$$\frac{\partial v}{\partial t} + fu = -g\frac{\partial \eta}{\partial y} + \frac{\tau_y^w}{\rho H} - \frac{rv}{H} \tag{2.2}$$

$$H\left(\frac{\partial u}{\partial x} + \frac{\partial v}{\partial y}\right) = 0 \tag{2.3}$$

where f is the Coriolis parameter, u and v are the horizontal, depth-averaged velocity components, g is acceleration due to gravity, η is the sea surface elevation, τ is the wind stress, ρ is the density, H is the water depth, and t is time. Conventional bottom friction parametrizations of the form rv/H were used, where r is a friction coefficient. Thus, bottom friction enters in (1.2) in the form of a depth-dependent drag coefficient multiplied by v. These equations describe a balance of the Coriolis force f with the horizontal pressure gradient due to sea surface height η variations, quadratic bottom friction r, and atmospheric forcing F, which includes wind stress τ and atmospheric pressure gradient $\bigtriangledown P_{atm}$.

In formulating the problem, a right-handed coordinate system was chosen such that the positive x-direction points seaward from the coast, and y-axis lies along a straight coastline at x=0. The depth distribution, H(x), is given by

$$H(x) = \begin{cases} \gamma_1 x & 0 \leq x < L_1 \\ \gamma_1 + \gamma_2(x - L_1) & L_1 \leq x \leq L_2 \end{cases} \tag{2.4}$$

where $\gamma_{1,2}$ and $L_{1,2}$ are the slopes and the cross-shelf lengths of the two regions of the continental shelf.

To calculate the structure and dispersion relationship of a CSW, only large-scales, subinertial and non-divergent motions were considered (see Appendix B). These three equations (2.1)-(2.3) have been solved to study the evolution of the coastal boundary in response to different forces. Several studies have described the effects of linear bottom friction on CSWs [67, 68] ; Webster [69] obtained an analytical solution to examine the wind forced circulation with bottom friction for an exponential shelf; Power et al [70] and Power et al [71] investigated the forced, barotropic shelf circulation over both an inclined and a bilinear continental margin using three different alongshore forces: offshore oceanic pressure gradients, offshore currents, and wind stress over the shelf.

Following these studies, four cases of CSWs, which have different alongshore forcing mechanisms, were investigated using a topography similar to Alborán sea: 1) no forcing mechanism. The behaviour of free CSWs was studied. 2) bottom friction. In order to know how free CSWs are modified by bottom friction, different values of this forcing were used. 3) alongshore wind stress and bottom friction. The forced response to wind forcing on two different margins was considered at the frequency of the wind-driven band. First, for different wind speed values, and then for different bottom friction values. Alongshore wind stress was assumed to be independent of "x" and the response was non-dispersive, allowing the use of the long-wave approximation. 4) alongshore atmospheric pressure gradient and bottom friction. The behaviour of CSWs considering different pressure gradient values was analyzed. Alongshore pressure gradient was assumed to be independent of "x". The alongshore pressure gradient at the outer edge of the continental margin enters the problem through the second boundary condition. It was assumed that the wind stress and the pressure gradients forcings propagate alongshore with the form $\tau = \tau_0(i(ly - \omega t))$ and $P = P_0(i(ly - \omega t))$, respectively, where τ_0 and P_0 are constants, l is the wavenumber and ω is the frequency of both the forcing and the response.

Elimination of u and v from (2.1)-(2.3), the following equation for η was obtained

$$H\frac{\partial}{\partial t}\left(\frac{\partial^2 \eta}{\partial x^2}\right) + \frac{dH}{dx}\frac{\partial}{\partial t}\left(\frac{\partial \eta}{\partial x}\right) + f\frac{dH}{dx}\frac{\partial \eta}{\partial y} + r\frac{\partial^2 \eta}{\partial x^2} = 0 \qquad (2.5)$$

This equation was first solved by Robinson [35], when he first coined the term 'contiental shelf wave'. Because of scaling assumptions (large-scales, and subinertial motions), no wind forcing term appears in this equation. Rather, the wind forcing appears as a boundary condition at the coast.

For waves travelling parallel to the coast with the form $\eta(x, y, t) = \phi(x) exp(i(ly + \omega t))$, where ϕ is the cross-shelf structure of the sea surface elevation, l is the alongshore wavenumber, and ω is the frequency, considering (2.4), and transforming x to dimensionless ζ, the equation (2.5) gives

For case 1), no forcing:

$$\zeta^2 \frac{\partial^2 \phi_k}{\partial \zeta^2} + \zeta \frac{\partial \phi_k}{\partial \zeta} + 2\mu \zeta^2 = 0 \tag{2.6}$$

where $\zeta = 2(x^{1/2})$, $\mu = (fl/\omega - f^2/g\gamma_k)$, and k is either the region 1 or region 2 of the shelf, respectively.

For cases 2) (bottom friction) and 3) (alongshore wind stress and bottom friction):

$$\xi \frac{\partial^2 \phi_k}{\partial \xi^2} + \frac{\partial \phi_k}{\partial \xi} - \xi \phi_k = 0 \tag{2.7}$$

where $\xi = 2(\sigma x + i\epsilon)^{1/2}/\sigma$, $\sigma = \omega/f$, $\epsilon = r/f\gamma_k L$, and $L = 1/l$.

The equations (2.6) and (2.7) can be expressed as a linear sum of Bessel and modified Bessel equations of order zero, respectively. Thus

For case 1)

$$\phi_k(z_k) = A_k J_0(z_k) + B_k Y_0(z_k) \tag{2.8}$$

where $z = 2\sqrt{\mu}\sqrt{x}$, A and B are constants which have values governed by the boundary and continuity conditions, and J_0, Y_0 are linearly independent solutions of the first and second kinds, respectively.

For cases 2), 3) and 4)

$$\phi_k(\xi_k) = C_k I_0(\xi_k) + D_k K_0(\xi_k) \tag{2.9}$$

where C and D are complex constants with values governed by the boundary and continuity conditions, and I_0, and K_0 are linearly independent solutions of the first and third kinds, respectively.

Equations (2.8) and (2.9) were solved for the three cases and with the appropriate boundary and continuity conditions. Each case has a different offshore boundary condition while the continuity conditions remain the same. In each case the boundary condition at the coast is that of no normal flow, i.e., $uH \to 0$ at $x \to 0$. For CSWs, the solution is constrained at the edge of the shelf, i.e., $\eta = 0$ at $x = L_2$. Thus, offshore boundary condition indicates that energy of CSWs is mainly confined on the continental shelf (i.e., coastally trapped).

The variables uH and η must be continuous over the entire margin and, in particular, at the shelf break. This implies that $\eta_1 = \eta_2$ at $x = L_1$, and $u_1 H_1 = u_2 H_2$ at $x = L_1$.

The coastal boundary condition is non homogeneous under wind forcing only, whereas offshore boundary and the continuity conditions remain the same; and the offshore boundary condition is non homogeneous under pressure gradients forcing only. A detailed description of boundary conditions is found in the Appendix B. The resolutions of equations was performed using Matlab$^{\text{TM}}$ program.

The velocity components, u and v, can be calculated from $\eta(x, y, t)$ solution and equations (2.1) and (2.2). The v velocity component was obtained from equation (2.1), and the u velocity component was calculated using equation (2.2) and the solutions of v and η. These expressions are found in the Appendix B.

Dispersion Relation

The wave properties (frequency and phase speed) are estimated by using a formula for the dispersion relation, which relates the frequency ω with the wavenumber l of the wave.The analytical solutions can be useful for comparing the characteristics of a region of the shelf to another, or for analyzing observational data [72]. As discuted by Huthance [17] and later by Sansón [73], there is no universal dispersion relation for waves over the arbitrary topography, but exact analytical solutions are calculated for idealized topographic shelf shapes. Some of these include solutions for a linearly varying [74], exponential concave-upward [75] and exponential convex-upward [51] shelf slope profile. Recently, Drivdal et al [52] derived a dispersion relation for CSWs in a shelf region with an unbounded flat outer ocean, a convex-upward exponential shelf, and an interior flat region of arbitrary width. In this chapter, a general dispersion relation was obtained for CSWs with a freely moving surface for the NCS of the Alborán

sea. The shelf was modeled by a depth profile with two single, constant slope regions (Figure 1.1, panel a).

Rearranging the expression $\mu = (fl/\omega - f^2/g\gamma_k)$ of equation (2.6), the dispersion relation for CSWs with this bottom topography becomes

$$\frac{\mu_n}{f} = \frac{lL}{\mu_n + f^2l^2/\gamma g} \tag{2.10}$$

The eigenvalues μ_n include a sequence of polynomials, that indicates the waves modes n. A necessary consequence of this is that each mode has its own unique dispersion relation.

Once the permissible values of μ are obtained, (2.10) can be used to find the dispersion relation $\omega = \omega_n(l)$. Equation (2.10) represents a cubic implicit dispersion relation to ω. Following [38], it can be shown that $\mu=2\nu+1$, and $\nu=0,1,2,...$ Rearranging the expression (2.10), and considering the nondimensional frequency $\sigma = \omega/f$ and the nondimensional wavenumber $k = lL$, this relation becomes

$$\sigma^3 - \left(1 + \frac{\gamma gk}{f^2}(2\nu+1)\right)\sigma + \frac{\gamma gk}{f^2} = 0 \tag{2.11}$$

For the case of CSW, $\nu \sim 1/2\sigma$ for $k \ll 1$, and $\sigma \ll 1$, and the above relation dispersion $\sigma(k)$ is determined with the Bessel function $J_0(2(k/\sigma)^{1/2})$. Then, ν_n should satisfy the Bessel function $J_0(\nu_n)$ for a countable infinite number of discrete $\nu = \nu_0, \nu_1, ...$ for a given l . Using the topography (2.4), the first three modes ν_{1-3} were calculated. Since (2.10) represents a cubic in ω, it follows that for each value of n, there are three roots j of $\omega(l)$. Then, corresponding of each ν_n, the cubic equation can be solved for the frequency function $\omega(j, l, \nu_n)$. Fore each mode of ν_n, the roots of $j = 1, 2$ correspond to edge waves and the mode $j = 3$ corresponds to CSWs [12].

By using the frequency data derived from observations and the continental shelf width, the wavelength l and the phase speed c of each mode can be calculated from the dispersion relation, which are used to solve equations (2.8) and (2.9).

2.4 Results

2.4.1 Observations

Wind transfer function

In attempting to study free waves, the wind driven component of each η_{adj} signal must first be removed using wind spectral transfer functions. Wind transfer function *TF* is calculated as the ratio of the co-spectrum of the adjusted sea level η_{adj} and the along-shore wind stress to the autospectrum of along-shore wind stress. The along-shore component of wind stress was calculated as F_y=$1 \cdot 10^{-3} \rho_a v_y |\mathbf{v}|$, where ρ_a is the air density (10^{-3} g/cm^{-3}) and v_y is the component of the wind speed $\mathbf{v}$ to the east (NCS) and west (SCS). According to the CSW propagation direction, westward winds were analyzed on the NCS and eastward winds on the SCS.

Figure 2.3 shows the gain of the *TF* (Fig. 2.3, $a - c$,$g - i$) and the coherence squared Φ^2 (Fig. 2.3, $d - f$,$j - l$) between the input alongshore wind stress and the output η_{adj} at the study stations as a function of frequency for the periods *P1* and *P2*. As a measure of statistical significance, the 95 % confidence levels are also shown, which were computed following Bendat [76]. The results indicate that the response to wind stress at $S1 - 6$ stations is small at the frequencies studied, suggesting the signal contained energy originating from a distant source. All frequencies where the wind stress and η_{adj} are significantly correlated (at 95 % level) were removed of the η_{adj}.
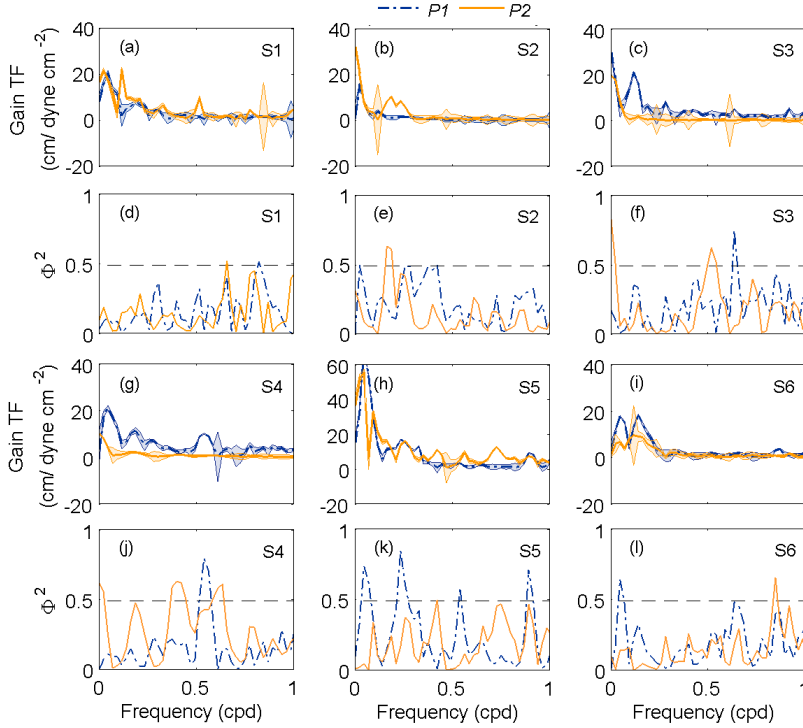
Figure 2.3: *The gain of the transfer function TF ($a - c, g - i$) and the coherence squared Φ^2 ($d - f, j - l$) between the input alongshore wind and the output sea level at the study stations in the periods P1 and P2. The 95% confidence limits for the gain are shown by the shaded areas, and for Φ^2 are shown by the dashed lines.*

Once isolated, the residual sea level η_{resi} was analyzed. Several clues indicated the existence of CSWs on the Alborán Sea (Fig. 2.4). This figure depicts the low-pass η_{resi} time series from the study stations ($a - b$), the atmospheric pressure p_{atm} (c), and the alongshore wind velocity data (d). The lags between the maximum sea level at the S1-3 stations are 9 h (between $S1 - S2$) and 31 h (between $S1 - S3$) (Fig. 2.4, a plot) for the NCS. For the SCS, the time lag between the maximum sea level at the $S5 - S6$ stations is 23 h (Fig. 2.4, b plot). Similar differences are not observed in p_{atm} (Fig. 2.4, c plot) nor in the wind velocity records (Fig. 2.4, d plot). The time lags between the maximum p_{atm} level and wind velocity are different than the time lags found between the study stations. These observations indicate that the speed with which weather systems move is different than the propagation speed of the residuals analyzed. Moreover, residual sea level fluctuations have no apparent association with weather systems, suggesting the residuals analyzed correspond to free waves.

The results suggest the presence of waves that travel westward and eastward on the NCS and SCS, respectively. To support this hypothesis and to gain insight into the propagation process, cross-correlations and cross spectrum analysis were performed on the data series.
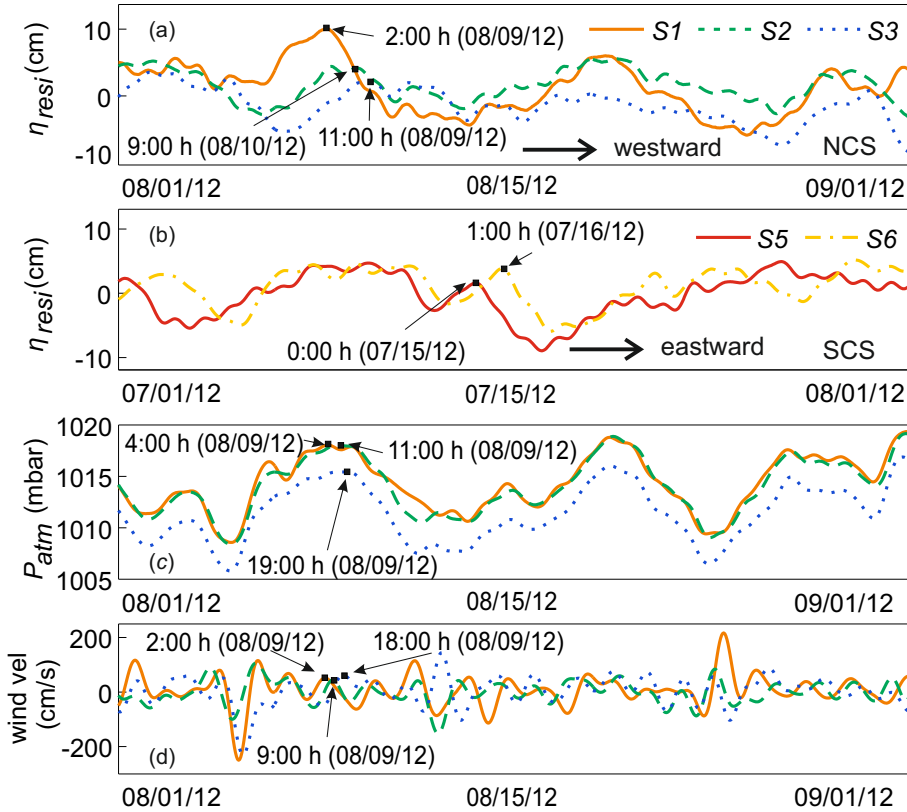
Figure 2.4: *A segment of the time series of the residual sea level data for the northern stations S1-3 (a), southern stations $S5 - 6$ (b), atmospheric pressure (c), and alongshore wind velocity data (d). Sea level data have been adjusted for the effect of the atmospheric pressure on sea level according to the isostatic approximation and the wind-coherent signal has been removed. The squares, which are depicted to guide the eye, indicate the dates on which a maximum peak is attained at the various stations. The propagation direction of the signal is also indicated.*

Figure 2.5 shows the autospectral density functions R of hourly sea level (both η and η_{resi}) at $S1 - 6$ stations for the $P1$ (upper plots) and $P2$ (lower plots) periods using the Welch method. In this figure the frequency was plotted against the logarithm of the energy spectral density. Dotted lines show the 95 % confidence limits of the spectra, which were computed according to the method of [76]. In general, the amplitudes of the η spectra exceed those of the η_{resi}. This is a consequence of removing the effects of atmospheric forcing. The most energetic
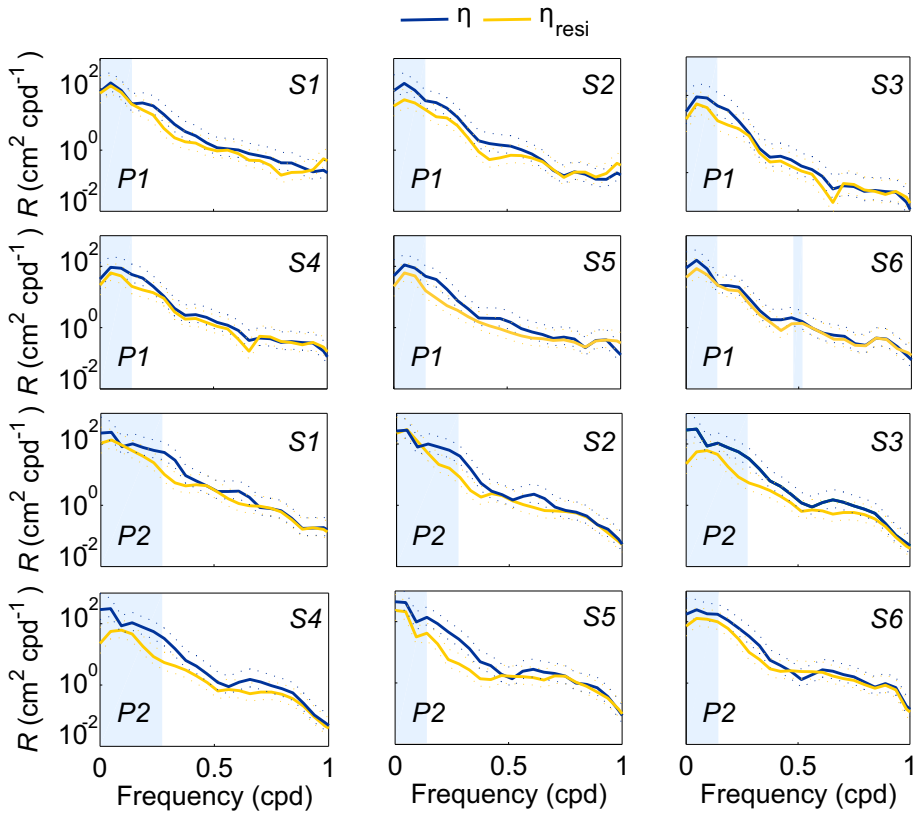
Figure 2.5: *Spectral density (cm²/cpd) at stations S1 − 6 of both the observed and residual sea level during P1 (upper plots) and P2 (lower plots) for frequencies lower than 1 cpd. The error bounds (dotted lines) in the spectra include the 95% confidence intervals. Shaded areas indicate the most energetic frequencies.*

peaks appear at the lowest frequencies for all stations in both periods. These peaks are found in η, and η_{resi} data. In the NCS, the most common energy in the $S1 − 4$ spectra is found in the frequency band 0-0.14 (0-0.28) cpd in the period $P1$ ($P2$). In the SCS, most of the common energy in the $S5 − 6$ stations is found in the frequency band 0-0.14 cpd in both the period $P1$ and $P2$, and there is a second peak with less energy in the 0.42-0.51 cpd in the period $P1$. The results indicate that the response to atmospheric forcing at the study stations is small at low frequencies, suggesting that the residual signal contains energy originating from a distant source.

For the study region, theory predicts that CSWs should travel westward on the NCS; in other words, the adjusted sea level at $S1$ should lead that at the $S4$

station. In contrast, on the SCS, this type of wave should travel eastward, and *S6* should behind at *S5*.

The following sections explain more results to support these behaviors.

Cross correlation

The propagation direction of the CSW and the time lags can be better determined from correlation functions of the lagged *CC* between the residual sea level at different stations [45, 77]. Figure 2.6 shows the *CC* between the residual sea level data from the study stations for both periods *P1* and *P2*. The positive or negative lags at the maximum *CC* indicate the propagation direction of the wave. Larger distances between stations are correlated with larger observed time lags (see Fig. 2.6).
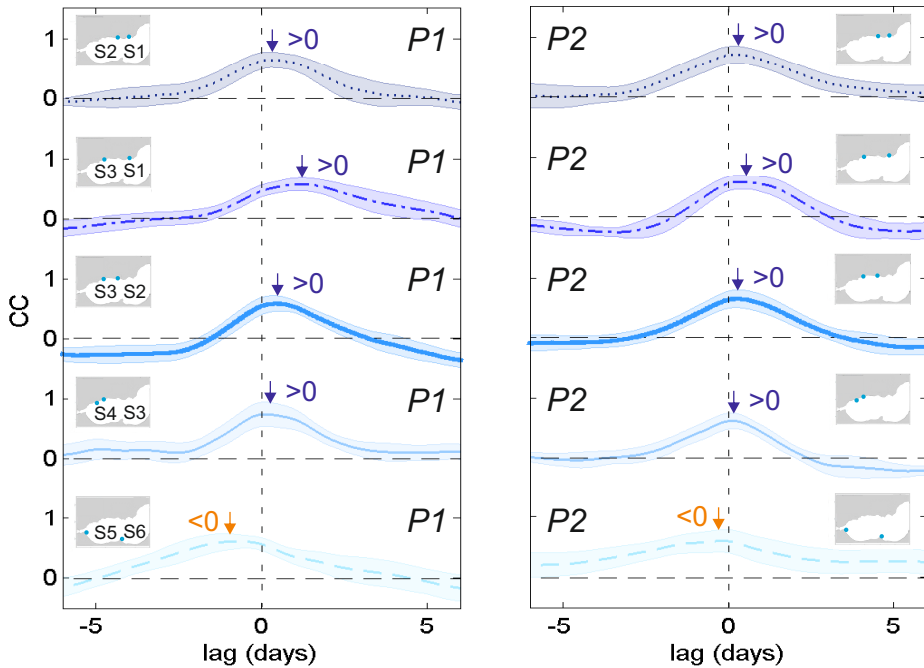
Figure 2.6: *Correlation functions of CC between the adjusted sea level at different stations (S1-S6) on the coast of the Alborán Sea for ±6 day time lags. The error bars (dashed areas) include the 95% confidence interval in cross correlation between study stations. Positive lags indicate that the western station of each pair lags relative to the eastern station.*

The maximum *CC* between *S3* and *S1* stations is located at a time lag of approximately 1.1 days and 0.4 days for *S3* and *S2*, respectively, whereas the

maximum CC between $S5$ and $S6$ appears at -0.8 days for the period $P1$ (see Fig. 2.6). Therefore, the propagation directions from the correlation functions between the residual sea level at adjacent stations were consistent with those of a travelling CSW in the study region. These results point to the presence of a westward-travelling signal on the NCS and a west-to-east-travelling signal on the SCS of Alborán Sea. A seasonal dependence in the correlation functions appeared to exist, with a maximum time lag occurring in the period $P1$.

Cross spectrum

The coherence squared Φ^2, which is analogous to the square of a correlation coefficient, and the phase difference τ between the residual sea level is determined to estimate the relationship and the time displacement between two records as a function of the frequency [77, 78]. This provides additional clues on the existence and propagation of CSWs at the study site. Figure 2.7 shows Φ^2 and τ between the residual sea levels as a function of the frequency. As a measure of statistical significance, confidence limits are also shown, which were computed following [79]. The phase differences are quite reliable when Φ^2 amplitudes are below the 90-95% confidence interval. Phase shifts τ are shown when Φ^2 has a significant value. Coherence squared Φ^2 has significant peaks, within the 95% confidence level, at frequencies 0-0.32 cpd for all pairs of stations on the NCS of the Alborán Sea for the period $P1$ ($S1 - 4$, left plots). For the pair of stations on the SCS, Φ^2 shows a peak within the frequency range 0.45-0.61 cpd ($S5 - S6$, left plot) for the period $P1$. For the period $P2$, Φ^2 is significant at the frequency range 0-0.28 cpd on the northern shelf ($S1 - 4$, right plots) and at 0.14 cpd on the southern shelf ($S5 - S6$, right plot).

The positive or negative sign of τ indicates the direction of propagation of the wave at the significant frequencies. A negative τ value at a frequency of 0-0.32 cpd for both $P1$ ($S1 - 4$ left plots) and $P2$ ($S1 - 4$ right plots) periods on the NCS indicates a westward-travelling signal, whereas the positive τ values at 0.45-0.61 cpd for the $P1$ period ($S5 - S6$ left plot) and 0.14 cpd for $P2$ ($S5 - S6$ right plot) on the SCS indicate an eastward-travelling signal in the Alborán Sea. These results are consistent with both the interpretation of the CC analysis and the continental shelf waves hypothesis previously described.

The phase differences, τ, between the study stations at the frequency of the maximum Φ^2 values are interpreted as lag times. The apparent wave phase speed c was evaluated and compared with the theoretical phase speed c_{th}. Different authors have developed some theoretical models to describe the CSW's, such as
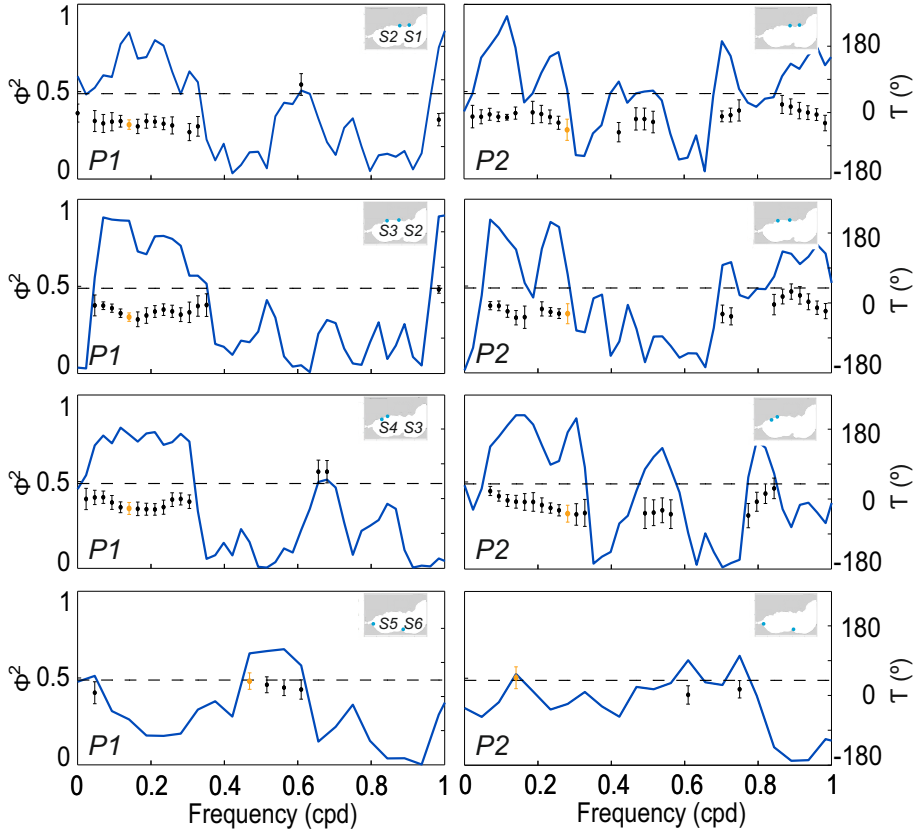
Figure 2.7: *Coherence squared Φ (solid) and phase τ (dots) versus frequency ω between residual sea levels at the study stations during the periods P1 (left) and P2 (right). Phase shifts are only shown when Φ² has a significant value. The horizontal dashed line represents the 95% confidence limit for the coherence. Error bars indicate the 95% confidence range for phase estimates when the coherence exceeded the 95% significance level. A negative phase means that the western station of each pair lags relative to the eastern station.*

[35],[51], [12], and [50]. Because of its simplicity, the theoretical phase speed c_{th} was calculated following Robinson's model (see Table 2.1). Robinson proposed a simple theoretical model for barotropic waves travelling in one direction only on a sloping finite width shelf (barotropic waves involve a lower Burger number, that is, a Burger number $<< 1$ [80]). The theoretical phase velocity, $c = \omega/k$ (where ω is the frequency and k is the wavenumber), is $c = fL/\gamma_j^2$ (where γ_j^2 (j=1,2,...) is defined as a part of the Bessel function of zero order $J_0(2\gamma_j)$. The first zero of J_0 lies at γ_j=1.2. For the fundamental mode of a CSW is $c = fL/1.44$, where L is the shelf width and f is the Coriolis parameter. Assuming typical shelf widths of the Alborán Sea $L \approx 22 - 40$ km and a Coriolis parameter of

$f = 7.51d^{-1}$, the phase velocity for the fundamental mode ranges between 1.32 and 2.5 m/s.

The phase differences, τ, indicate, for example, that the S1 sea level leads S2 by approximately 32° at approximately 0.14 cpd. This phase shift between these two stations, 90 km apart, implies a c of 1.63 m/s. This c value can be compared with the theoretical c_{th} value. For the period $P1$, the wave velocity at the frequency of the maximum coherence squared Φ^2 value appears to be on the same order as the c_{th} value (1.32-1.52 m/s) of a CSW travelling along the northern coast of the study region (see table 2.1). However, the waves appear to travel considerably faster than predicted by the theory along the southern shelf. For the period $P2$, the wave velocity between stations S1-S4 on the northern shelf is faster than that predicted by the theory (observed values of approximately 2.2-3 m/s) (see Table 2.1).

Table 2.1: *Comparison of the theoretical and observed phase relationships, τ_{th} and τ, respectively, for pairs of stations, during P1 and P2. The observed wave velocity c is evaluated at the frequencies of 0.14 (0.46) cpd during P1 and 0.28 (0.14) cpd during P2 on the NCS (SCS).*

Station pairs	c_{th} (m/s)	c (m/s) P1	c (m/s) P2	Time lag$_{th}$ (day)	Time lag (day) P1	Time lag (day) P2	τ (°) P1	τ (°) P2
S1-S2	1.32	1.63	2.2	0.8	0.63	0.48	32	47
S2-S3	1.43	1.2	3	0.56	0.67	0.27	35	27
S3-S4	1.52	1.67	2.5	0.57	0.52	0.35	26	35
S5-S6	2.5	8	2.7	0.97	0.31	0.92	41	46

2.4.2 Theoretical analysis

Dispersion relation

Figure 2.8 displays the dispersion diagram corresponding to the first three CSW modes. The dispersion curves are straight lines with a slope determined by the governing topographic inputs. The slopes of these lines also represent the theoretical average phase speed of the coastal waves propagating in the Alborán sea.

The same parameters were used to solve the different cases. Thus, a value of $8.69 \cdot 10^{-5}$ s^{-1} was chosen for f which is appropriate for the Alborán sea. Following the results of the observations, a period of T=3 days was used to study CSWs. For wind forced shelf waves, typical values of wind blowing in the Alborán sea were taken into account, so westward wind speeds of 5 and 10 m/s were used. A value of r=0.003 m/s was appropriate for this shelf.
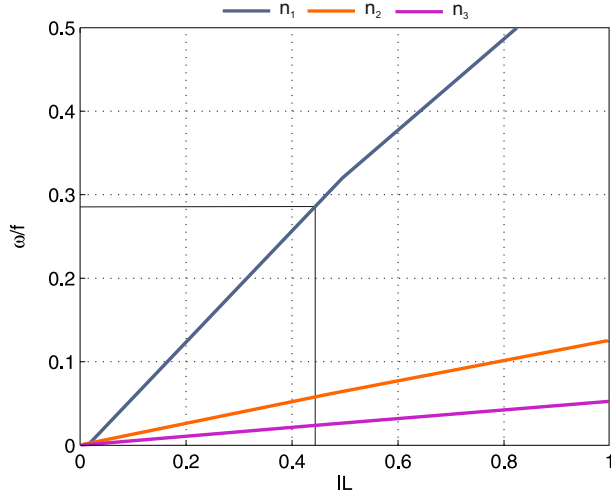
Figure 2.8: *Dispersion relation for the cross-shelf profile corresponding to the Alborán Sea continental shelf. First three modes are shown. The x-label is the nondimensional wavenumber l, namely, l multiplied by the width of the shelf, L; and the y-axis label is the nondimensional frequency ω, namely, ω divided by the Coriolis parameter, f. Black lines indicate the wavenumber and frequency corresponding to a period of 3 days.*

Case 1) Free continental shelf waves

By solving equation (2.8) the cross-shore behaviour of free CSWs modes were calculated. Each mode is composed of two regions, a smoother slope component and a steeper slope solution. Figure 2.9 shows the three first wave modes to a CSW propagating on a bottom topography similar to Alborán sea. Normalized wave amplitude is represented, which is calculated dividing by the maximum amplitude value at the coast. The parameters L, and γ_{1-2} correspond to a mean values of the NCS (Table 2.2). Cross- shelf amplitudes of all modes are maximum at the coast, and decrease rapidly with the distance from the coastline. The first mode presents a rapid decrease over the region 1, and a more smoothing decrease toward zero over the region 2 of the continental shelf. Moreover, additional oscillations with decreasing amplitudes appear with increasing mode number n. It can see that the $(2n+1)$th mode presents one more zero than the nth mode, consistent with the general eigenfunction theory [81]. It has also been seen by [72].

In nature, lower wave modes are the most energetic. Therefore, the next results of this chapter only take account the first mode. Figure 2.10 present the cross-shelf shape of the first wave mode for different regions of the Alborán continental shelf. This figure reveals that although the shape of amplitude
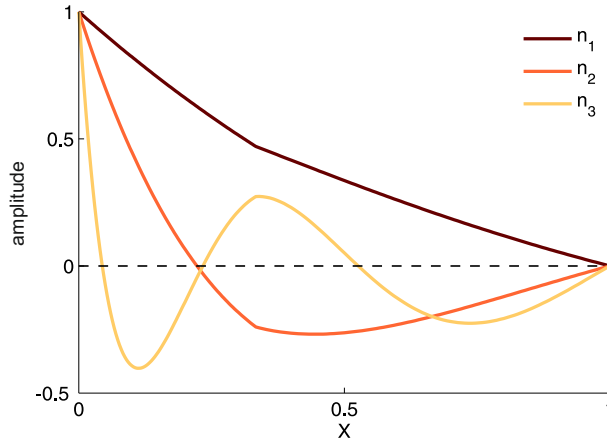
Figure 2.9: *Cross-shelf eigenmode structure of the first three free continental shelf wave modes. The amplitudes and the distance are normalized with values set to 1 at the coast and the edge of the continental shelf, respectively.*

Table 2.2: *Geometry of different regions of the NCS of the Alborán sea.*

Station	L_1 (Km)	L_2 (Km)	γ_1	γ_2
S1	4	27	0.02	0.04
S2	4	20	0.02	0.05
S3	8	30	0.01	0.04
S4	8	30	0.01	0.04

functions is the same for all cases, shorter waves are much more trapped by the coastline than longer waves. Geometrical parameters values used are presented in Table 2.2. Wavelengths were determined by the dispersion relation from a determined period. According to Figure 2.8, the waves with a period of 3 days have different wavelengths of depending on the width continental shelf. If the width of the shelf L is chosen as 23 km, the wavenumber of the wave is $1.95 \cdot 10^{-5}$ m^{-1}. Thus, the first free CSW mode in the Alborán sea correspond to wavelengths of 279, 349 and 418 Km for the $S1 - S2$, $S2 - S3$, and $S3 - S4$ regions, respectively, which are propagating with phase velocities of 1.2, 1.35, and 1.6 m/s, respectively. These phase velocities are quite similar to those calculated in Table 2.1.
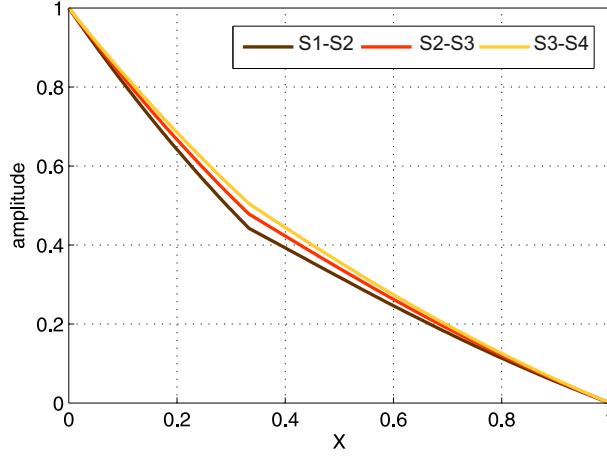
Figure 2.10: *Cross-shelf eigenmode structure of the first free continental shelf wave mode considering different regions in the NCS of the Alborán sea. The amplitudes and the distance are normalized with values set to 1 at the coast and the edge of the continental shelf, respectively.*

Case 2) Bottom frictional continental shelf waves

This case was solved using equation (2.9) to obtain the cross-shore behaviour of CSWs that have bottom friction and then, to know how free CSWs are modified by this parameter. In order to better interpret the results phase functions were defined for the surface displacement and the horizontal velocity components. Phase functions were defined by

$$\varphi_\eta(x,\sigma) = tan^{-1}(Imag\,\{\eta\}\,, Re\,\{\eta\}) \tag{2.12}$$

$$\varphi_{u,v}(x,\sigma) = tan^{-1}(Imag\,\{u,v\}\,, Re\,\{u,v\}) \tag{2.13}$$

which represent temporal phase differences between the response and the forcing. Since both η and horizontal velocity components are proportional to $e^{-i\omega t}$, $\varphi > 0$ ($\varphi < 0$) indicates that forced solutions lag (lead) free waves when $\omega < 0$ ($\omega > 0$).

Cross-shelf structures of the propagating mode 1 CSWs for no bottom friction (free solution) and different bottom friction values (frictional solution) were compared for amplitudes of sea level $\phi(x)$, and horizontal velocity components $u(x)$ and $v(x)$ for a wave propagating with a period of T=3 days. Figure 2.11 shows both the cross-shelf amplitudes and phases of $\phi(x)$, $u(x)$, $v(x)$. The amplitudes of $\phi(x)$ (Figure 2.11 a), $u(x)$ (Figure 2.11 b), and $v(x)$ (Figure 2.11 c)

were normalized dividing by its maximum value, and the cross-shelf distance was normalized dividing by the edge of the continental shelf.
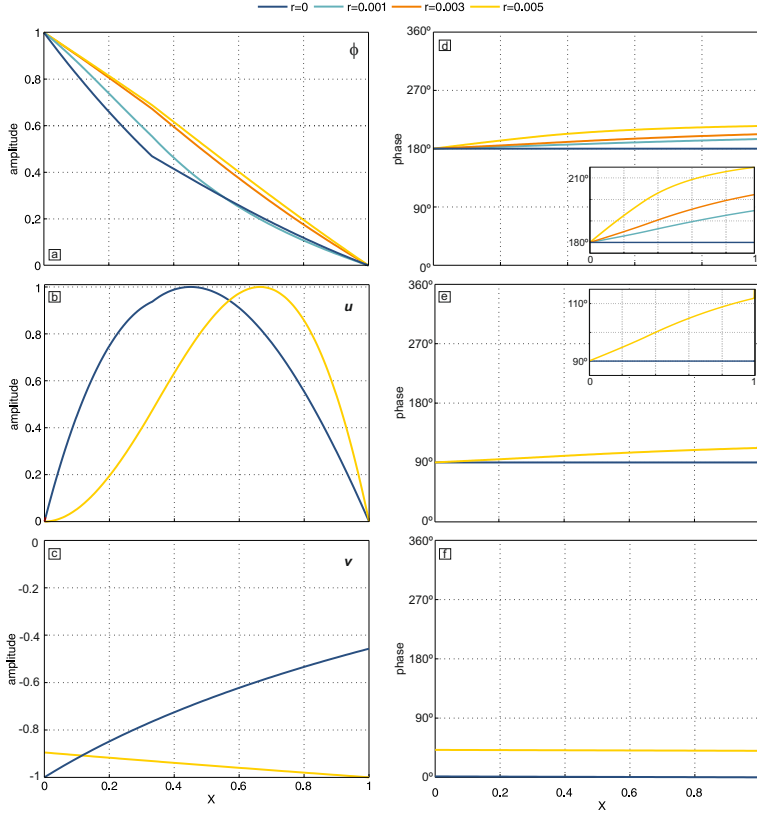
Figure 2.11: *Cross-shelf eigenmode structure of the first free continental shelf wave mode (r=0 m s^{-1}, dark blue line), and considering different values of bottom friction (r=0.01, 0.03, and 0.05 m s^{-1}, light blue, orange, and yellow lines, respectively) over a bilinear bottom topography. Surface displacement, ϕ, panel (a), and horizontal velocity components, u, v, panels (b) and (c), respectively, are displayed. Phase of ϕ, u, and v are also shown. Normalized amplitudes and the cross-shelf distance are shown.*

The phase of each solution was taken to be such that the phase of the surface elevation is 180º at the coast. The presence of bottom friction alters both the amplitude (Figure 2.11 a-c) and phases (Figure 2.11 d-f) of ϕ(x), u(x), and v(x) across the shelf. The amplitude of ϕ(x) is maximum at the coast for free and frictional solutions (Figure 2.11 a). Figure 2.12 also shows the cross shelf behaviour of the sea surface depending of bottom friction.In contrast, the amplitude of v(x) is maximum at the coast for the free solution, but this behaviour is different to the bottom friction, which increases from the coast to reach a maximum at the edge of the continental shelf (Figure 2.11 b). It can see that

phases of the frictional solutions increase seaward for all variables and then, their fluctuations at the coast lead those offshore (Figure 2.11 d-f). Moreover, phases of free solutions do not change along the same region, and these phases are lower than phases of the bottom friction solutions. Therefore, forced solutions delay free CSWs movement.
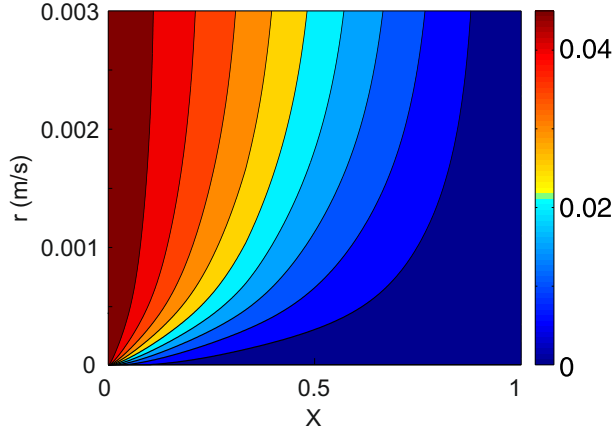
Figure 2.12: Behaviour of cross-shelf structure for surface displacement for the first mode of a CSW considering different values of bottom friction.

Case 3) Bottom friction and wind forced continental shelf waves

The wind forced circulation was examined for CSWs that have bottom friction by solving equation (2.9). The dependence of the response of the wind forcing, on its spatial structure, and on the amount of bottom friction, are interpretable using the mechanism of frictional CSWs [69]. It is assumed that variations of wind stress across the shelf are not important and the wind stress propagates alongshore in the form

$$\tau(y, t) = \tau_0 exp\left[i\left(ly - \omega t\right)\right] \tag{2.14}$$

where τ_0 is a constant that is determined as $\tau_0 = \rho_{air} C_D U_{10}^2$; ρ_{air} is the density of the air; C_d is a dimensionless quantity wind-drag coefficient; and U_{10}^2 is the wind speed at 10 meters above the water surface. The forcing function propagating with the coast on its left if wind is westward and then, a this wind direction was considered in the analysis. As it was mentioned above, a period of T=3 days, and wind speeds of 5 and 10 m/s parameters were used to compare wind forced and free waves.

First, cross- shelf behaviour of forced solutions were considered. Figure 2.13 shows cross-shelf structures for ϕ (Figure 2.13 a), u (Figure 2.13 b), and v (Figure 2.13 c) for mode 1 of a wind and bottom friction forced CSW. The amplitudes of $\phi(x)$, $u(x)$, and $v(x)$ were normalized dividing by its maximum value, and the cross-shelf distance was normalized dividing by the edge of the continental shelf. Maximum amplitudes of ϕ and v are found at the coast. Negative values of v indicate that the wave propagates with the coast on the left. Phases of forced solutions (Figure 2.13 d-f) are higher than those of free solutions, indicating that forced solutions are delayed with respect to free solutions, as expected. It can see that phases of forced solutions increase seaward and then, their fluctuations at the coast lead those offshore.
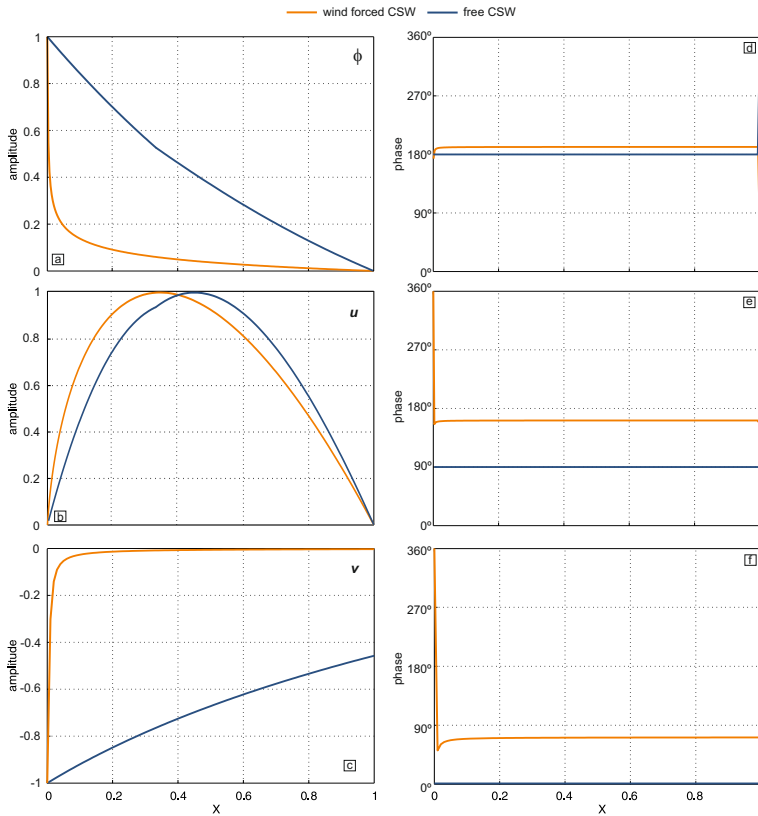
Figure 2.13: *Cross-shelf structure of the first free continental shelf wave mode (dark blue lines) for T=3 days, and a wind forced continental shelf wave considering a wind speed of 5 m/s (orange lines) over a bilinear bottom topography. Surface displacement ϕ (panel a), and horizontal velocity components u and v (panels b and c, respectively) are presented. Phase of surface displacement, u and v are also displayed (panels d-f, respectively). Normalized amplitudes and the cross-shelf distance are shown.*

Moreover, phase shifts of forced solutions across the continental shelf are more important near the coast because of the increase in frictional effects (Figure 2.13 d-f). The increase of wind velocity also generates an increase of sea surface ϕ, u, and v amplitudes (Figure 2.14a-c). Moreover, if r=0, the sea surface amplitude considering wind stress forcing is quite higher than free solution (Figure 2.14 a). In contrast, if bottom friction is increased, sea surface amplitude is decreased (Figure 2.14 d), and phases of η increase (Figure 2.13 d-f). This increasing indicate that forced solution slower the greater bottom friction. The cross-shelf structure of u (Figure 2.13 b, e) and v (Figure 2.13 c, f) is also altered considering wind stress forcing and bottom friction. By increasing the wind stress forcing current components also increase (Figure 2.14 b, c). In contrast, if bottom friction is increased, current components u and v are decreased (Figure reffig:wind2 e, f, respectively). Therefore, the presence of both wind stress and bottom friction alters both the amplitude and phases of ϕ, u, and v across the shelf.
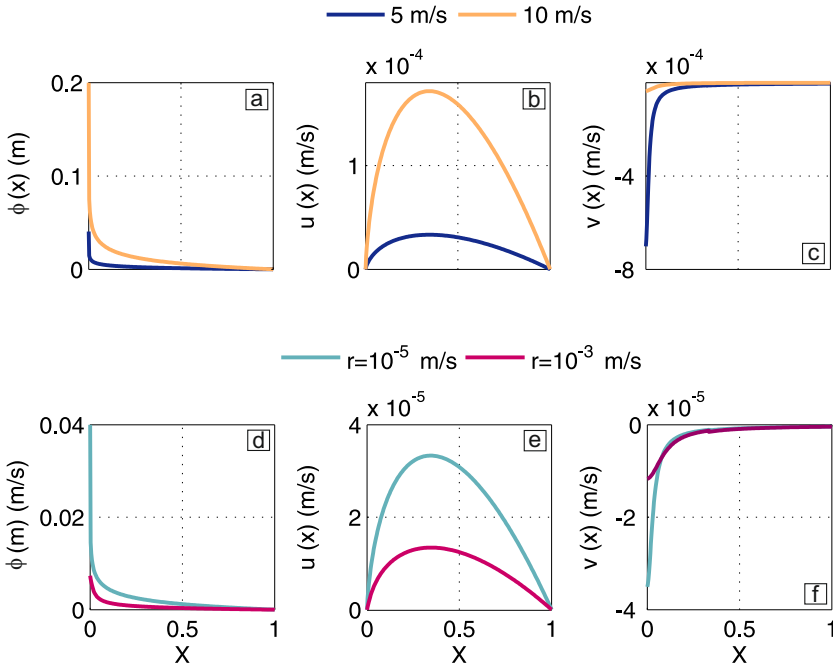
Figure 2.14: *Cross-shelf structure for surface displacement η, and horizontal velocity components u and v for the first mode of a wind forced continental shelf wave for T=3 days. Panels a-c: $\phi(x)$ (panel a), u(x) (panel b), and v(x) (panel c) considering no bottom friction and different values of wind speed (5 m/s (dark blue lines), and 10 m/s (orange lines)). Panels d-f: $\phi(x)$ (panel d), u(x) (panel e), and v(x) (panel f) considering a wind speed of 5 m/s and different values of bottom friction (r=10^{-5}m/s (light blue lines), and r=10^{-3}m/s (purple lines)). Normalized cross-shelf distance is shown.*

Considering oscillations travelling parallel to the coast, as previously described, the alongshore behaviour of forced waves were obtained. The coastline is coincident with the y-axis at x=0 . Figure 2.15 displays both the cross-shelf and along-shelf behaviour of the forced response to wind and bottom friction forcings on two different margins , first for forcing moving in a margin with constant slope (Figure 2.15 b), and also in a margin with a bilinear bottom topography similar to (2.4) (Figure 2.15 c). For the constant slope region, significant surface displacements are trapped in a nearshore band. However, in the two single, constant slope regions, significant surface displacements are found over the entire first region, because of the reduction in the volume of water overlying it. The wind generates a pressure response which is trapped nearshore. If the continental shelf occurs within this trapping length, then the shelf width becomes the effective trapping length.
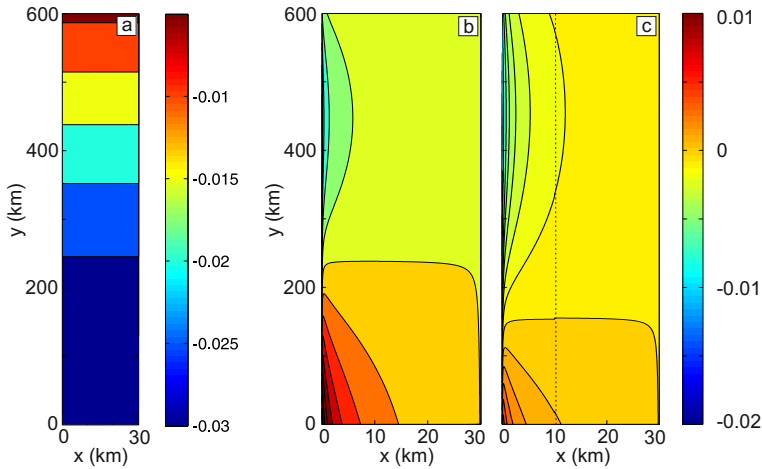
Figure 2.15: The response to a wind stress forcing (panel a) of a continental shelf wave for T=3 days propagating over a constant slope region (panel b), and a bilinear bottom topography (panel c). Surface displacement is presented. The horizontal axis is the cross-shelf component and the vertical axis is the along-shelf component.

Case 4) Alongshore pressure gradient forced continental shelf waves

The CSWs structure forced by an alongshore pressure gradient was examined by solving the equation (2.9) similar to the cases 2) and 3). It is assumed that pressure propagates alongshore in the form

$$P\left(y, t\right) = P_0 exp\left[i\left(ly - \omega t\right)\right] \qquad (2.15)$$

where P_0 is a constant, $P_0 = \eta_0 l$.

Figure 2.16 shows both cross-shelf structures of ϕ, u, and v of a CSW forced by an alongshore pressure gradient at the outer edge of the continental shelf, and bottom friction included (Figure 2.16 a-c, respectively).
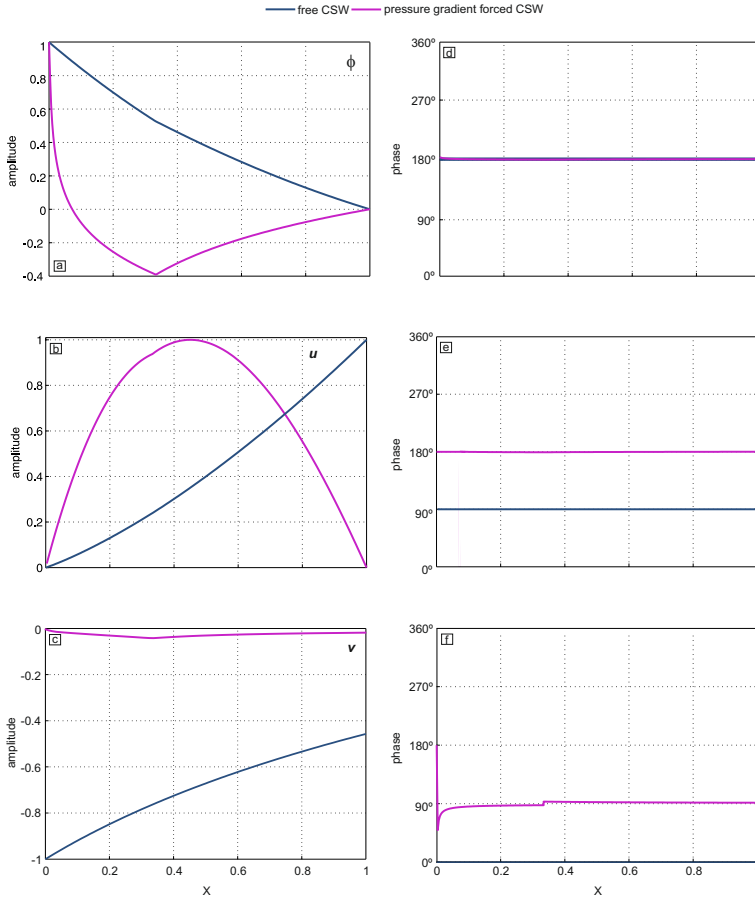
Figure 2.16: *Cross-shelf structure of the first free continental shelf wave mode (dark blue lines) for T=3 days, and a pressure gradient forced continental shelf wave considering a pressure gradient of 10^{-3} Pa/m (purple lines) over a bilinear bottom topography. Surface displacement (panel a), and horizontal velocity components u and v (panels b and c, respectively) are presented. Phase of surface displacement, u and v are also displayed (panels d-f, respectively). Normalized amplitudes and the cross-shelf distance are shown.*

Similar to previously cases, forced solutions are different to free solutions. Maximum ϕ is now at the coast, and a secondary maximum appears at the edge of the region 1 (Figure 2.16 a). The structure of the alongshore velocity field is also altered (Figure 2.16 c); it is zero at the coast, and increases linearly with distance offshore, and is maximum at the edge of the region 1. It can see that there is a

very little phase difference across the margin in η (Figure 2.16 d). Again, forced solutions lag free solutions in phase (Figure 2.16 d-f). Moreover, the increase of pressure gradients generates an increase of sea surface η, u, and v (Figure 2.17 a-c, respectively).
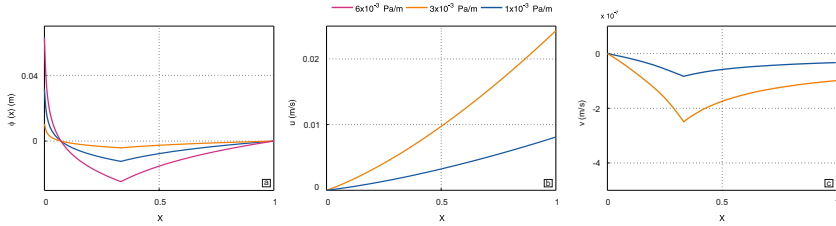
Figure 2.17: *Cross-shelf structure of surface displacement (panel a), and horizontal velocity components, u (panel b) and v (panel c), for the first mode of an alongshore pressure gradient forced continental shelf wave for T=3 days, considering different values of pressure gradients. Normalized cross-shelf distance is shown.*

Figures 2.18 and 2.19 show the effects of pressure gradients propagating over continental shelves with different width. The narrow continental shelf has a maximum ϕ at the coast with secondary over the outer region 1. Maximum alongshore velocities are also found near the outer region 1. When the width of the continental shelf increases, the sea surface amplitude ϕ shows a reduction at both the coast and the outer region 1 (Figures 2.18 and 2.19). Therefore, the effects of the pressure gradients are weaken with the continental shelf width.
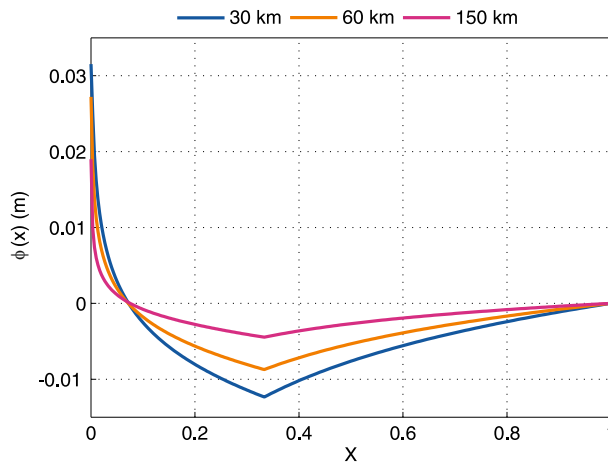
Figure 2.18: *Cross-shelf structure of surface displacement η for the first mode of an alongshore pressure gradient forced continental shelf wave for T=3 days, considering a pressure gradient of 10^{-3} Pa/m over a bilinear bottom topography with the shelf widths varying with L=30 km (blue line), L=60 km (orange line), and L=150 km (purple line). Normalized cross-shelf distance is shown.*
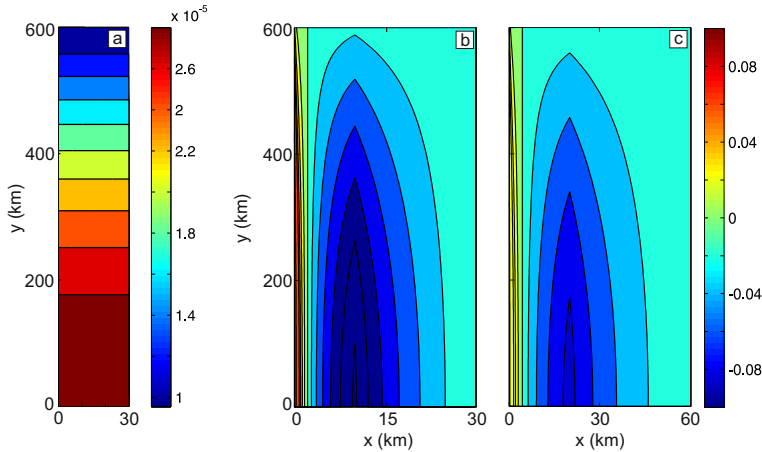
Figure 2.19: *The response to an alonshore pressure gradient forcing (panel a) of a continental shelf wave for T=3 days propagating over a bilinear bottom topography with the shelf widths varying with L=30 km (panel b), and L=60 km (panel c). The horizontal axis is the cross-shelf component and the vertical axis is the along-shelf component.*

2.5 Discussion

2.5.1 Observations

Our analyses and results suggest that travelling free CSWs exist on both the NCS and SCS of the Alborán Sea. The results of the spectral analysis R show energy peaks in the frequency band 0-0.14 and 0-0.28 cpd (0-0.14 and 0.42-0.51 cpd) on the NCS (SCS) for η_{resi}, after removing both the astronomical and meteorological influence. These results indicate the existence of a non-local sea level response to atmospheric influence for the studied frequencies. The cross-correlation between the residual sea level at different stations and the coherence and phase difference spectra indicate that a travelling westward (eastward) oscillation exists on the NCS (SCS), which is consistent with the propagation direction of the CSW. Similar analyses by [64] and [72] also showed low-frequency oscillations on the Oregon continental shelf and in the Mid- Atlantic Bight, respectively, which were attributed to the existence of CSWs.

The coherence squared Φ^2 and phase τ spectra indicate a CSW travelling with a phase velocity that appears to be in agreement with the CSW theory on the NCS (SCS) for the $P1$ ($P2$) period. In contrast, the free wave on the NCS (SCS) in the $P2$ ($P1$) period travels at a higher phase speed than the calculated theoretical wave speed. Discrepancies between the theory and our observations may be likely the result of the effects of local generation, density stratification, and irregular topography, which have not been considered. The effects of deep-sea

stratification on the free waves speed were studied by [36] and [13]. It was found that stratification increases frequency (hence wave speed) for a given wave mode [78]). The flow in the Alborán Sea is predominantly barotropic [**?**] and then, the stratification may not explain this higher phase speed. One of the factors driving the variability of the Alborán Sea is the temporal variability of the Atlantic inflow through the Gibraltar Strait (i.e., the Atlantic Jet) [4], which fluctuates in a north-south direction [82]. These displacements could explain the wave velocities anomalies observed in this study. Therefore, a possible cause of the higher wave speeds on the NCS during the $P2$ period could be the existence of cyclonic circulation forced by the Atlantic Jet along the northwestern shelf of the Alborán Sea because westerly winds strengthen the jet and trigger coastal upwelling [82, 83]. During the $P1$ period, the Atlantic inflow is higher [4], and part of the jet flows to the west and is incorporated into an anticyclonic gyre. The remainder flows southeast along the African coast forming the southern periphery of a cyclonic circulation [84], which could be the cause of the higher wave velocities observed on the SCS.

The observed time lags of the cross-correlation analysis in the period $P2$ are very small. The observed seasonal dependence on the time lag may be due to the seasonal variations in the surface speed of the currents in the Alborán Sea, but this hypothesis has not been corroborated. Simultaneous continuous records of current and sea level might be required to further explore this hypothesis.

Another point of interest is the study of possible interaction between CSWs travelling in opposite directions, because of the morphology of the back-arc study area. The presence of CSWs travelling in opposite directions on the northern and southern shelves of the Alborán Sea opens the possibility of interactions and the existence of amphidromic points associated with this type of waves. Since the amplitude decreases roughly exponentially with increasing distance from the coast and the NCS and SCS are relatively close to each other, the CSWs travelling on the two shelves might interact near the Gibraltar Strait. Simultaneous continuous records of current and sea level along transverse sections might be required to further explore this aspect. A possible leakage of a portion of the energy of a CSW on the NCS might occur through the Gibraltar Strait, but another portion might occasionally turn around and propagate from the Gibraltar Strait to the Mediterranean Sea.

Finally, it is worthy mention that a same weather system might generate winds in opposite directions and might therefore generate simultaneous CSW travelling in both continental shelves. Thus, space scales of the weather system

could be defining wind variations in two directions in both shelves. It should be necessary that the spatial scale of the weather system was the same as that of the study site. A detailed and broad study will be necessary to test this assumption.

2.5.2 *Theoretical analysis*

A simple, barotropic theoretical model for CSWs propagating over a bilinear continental margin, similar to NCS of Alborán sea, was developed for both free and forced, which varies sinusoidally in time and space alongshore, waves. Bottom friction, wind stress, and atmospheric pressure gradients were considered. The dispersion relation showed that frequency and wavenumber are dependent upon shelf width. For a determined frequency, the wider continental shelf, the lower wavenumber. By considering a shelf wave with a period of 3 days, the phase speeds of observations agree well with the theoretical first-mode dispersion curve.

For free waves, results showed that maximum sea surface and alongshore velocity component remain and the coast, and as wave mode increases, more and more nodes are squeezed onto the shelf. These results were also obtained by Schulz [72], who addressed the propagation of CSW in the Mid-Atlantic Bight considering a combined linear shelf, exponential slope bathymetry [85]. In practise, a CSW, in the absence of forcing, would lose energy by friction, interaction with small scale topographic variations, etc. Thus, when friction is included, maximum sea surface amplitudes remain at the coast but, in contrast, alongshore velocity component is constrained to be minimum at the coast because bottom friction introduces an alongshore decay. Bottom friction alters the structures of sea surface and velocity components of free shelf waves. Moreover, their altered structures exhibit phase differences across the continental shelf where the flow nearshore leads that offshore in time. These results were also determined by [85] and [69] in their perturbation solution to the frictional problem. Therefore, bottom friction affects the free CSWs.

The wind forced solutions indicated that the presence of wind stress and bottom friction also alters the amplitude and phases of the sea surface and the velocity components of a free CSW. When bottom friction is zero, there is a direct relationship between wind velocity and shelf waves parameters. Moreover, sea surface and velocity amplitudes of forced solutions are higher than those of free solutions, indicating that wind forcing amplifies the behaviour of free waves. In contrast, when bottom friction is included, amplitudes of sea surface and velocity components decrease, and again the nearshore response leads that offshore in

phase. On the other hand, results also displayed the importance of continental shelf width in determining the structure of the solutions. Thus, as also found by [71], if continental margin is within this trapping length, the shelf width becomes the effective trapping length.

The atmospheric pressure gradient solutions displayed that maximum sea surface amplitude occurs at the coast, with a nodal line at the edge of the continental shelf, and a secondary maximum at the edge of the region 1. Similar to previously cases, atmospheric pressure gradients alters cross shelf structure of free shelf waves. The atmospheric pressure solutions indicated that the flow is energetic from coast toward the region 1 edge. This is a characteristic that occurs as a result of the larger effect of bottom friction on depth averaged flow in shallow waters. By contrast, wind-driver flow are energetic near the coast and become weaker in deeper water because a greater mass of water is acted upon by the wind in deeper water. These results were also obtained by [86]. Otherwise, results indicated that for wider continental shelves, the effect of pressure gradients are weaken. Previously studies showed that the role of the alongshore atmospheric pressure gradients in driving coastal circulation appears to be important on narrow continental margins [87].

The slowing of the free waves by bottom friction is clearly evident in the forced solutions.

Results presented here describe the main characteristics of CSWs propagating on a continental shelf similar to NCS Alborán sea. Moreover, the presented theoretical model appears to clearly explain how different forcings modify the behaviour of free CSWs.

2.6   Conclusions

The general objective of this chapter is to identify and to characterize CSWs on the continental shelves of the Alborán sea. To achieve this objective, the existence of this type of waves was verified using a statistical approach and a theoretical work.

The following conclusions have been obtained:

1. The cross-correlation analyses indicated time lags that are consistent with the hypothesis of the propagation of the free shelf waves predicted by the continental shelf wave theory. Thus, the presence of a westward-travelling signal on the NCS and a west-to-east travelling signal on the SCS of the Alborán Sea was confirmed.

2. The cross spectra between residual sea level at the six locations showed significant coherence at long periods. For these periods, the phase difference spectra showed that the directions of propagation of the free waves are consistent with the interpretation of the cross correlation analysis. There is evidence of a seasonal variation in the phase speed of the waves, which may be related to variations in the speeds of currents in the Alborán Sea.

3. The observations suggested the presence of continental shelf waves on both coasts of the Alborán Sea. This discovery provides a promising line of research relating to the possible interaction between CSWs travelling in opposite directions, because of the morphology of the back-arc study area.

4. The main theoretical characteristics and properties of the CSWs were studied using an analytical model. The linear shallow water equations, considering some assumptions, were developed for a continental shelf with a bottom topography similar to Alborán sea. The main results were that the presence of bottom friction, alongshore wind stress, and atmospheric pressure gradient alter the structure of free CSWs.

5. The results from this theoretical analysis have important implications for the construction of numerical models of shelf circulation, and to help to understand how the solution structure depends on parameters and assumptions.

Part II

HYDRODYNAMICS PROCESSES IN A SUBMARINE CANYON

3

General circulation over submarine canyons

I*n this chapter, the general circulation of a narrow submarine canyon is described, which will be used to be compared to the results of the next chapters of this Thesis. This chapter also determines the essential dynamics of the Jolúcar submarine canyon by using a scaling analysis with a selected number of dimensionless numbers that reflect the importance of both stratification and rotation parameters. Results are compared to another submarine canyons around the world.*

3.1   Introduction and state of art

Continental margins around the world are often interrupted by submarine canyons. Submarine canyons, first spotlighted by [88], are steep-side V-shaped valleys of continental slopes that deeply incise the continental shelf [89]. They vary greatly in both shape and size. Thus, short canyons present a canyon head which reaches the depth of the continental shelf before the coast [28, 90]. In contrast, long canyons feature a canyon head that does not reach the continental

shelf depth before the coastline, and then extend far into the coastal region and continue in straits or estuaries [90].

The origin of submarine canyons is not fully understood and it has intrigued marine geologist for a long time and is still a matter of debate. Their formation was early related both to subaerial erosion during the sea level lowering, and to submarine erosion favoured by tectonic discontinuities [91]. The main processes involved in their origin include: subaerial erosion of the upper canyon; erosion by turbidity currents; erosion by the slow mass movement of sediment down-canyon by creep, progressive slumps, sand falls, and later redistribution of sediment by deep-sea bottom currents; erosion by bottom currents other than turbidity currents; and drowning by subsidence of valleys cut subaerially, and upbuilding of canyon walls [19].

Submarine canyons are regions of enhanced localized upwelling [28], and they are important for cross-shelf exchange of nutrient flux onto the continental shelf [21, 22, 92]. Therefore, they play and important role in regional ecosystems because they are often biologically active areas with a nutrient source that increases dense krill and fish aggregations during upwelling favourable conditions [29].

Submarine canyons are also important for the exchange of water and particles between the coastal area and the ocean basin, and therefore they play a crucial role in the global biochemical cycling and climatic changes [93].

Moreover, the presence of submarine canyons can modify and enhance the effects of other physical processes. Their bottom topography is likely to modify the internal waves field which causes intense turbulence and mixing [94–96]. The interaction of shelf flow with abrupt canyons topography is probable to result in the generation of trapped waves, and the energy of low mode coastal trapped waves found in the continental shelf may scattered into higher modes due to the change in the bottom topography [97].

Therefore, submarine canyons have been the subject of research for a long time due to their great importance. Thus, with the increasing variability of sampling and surveying technologies, submarine canyons studies have significantly increased (Figure 3.1). As a result of this increase in the number of researches, understanding of submarine canyon is gradually growing. The circulation in a submarine canyon has been investigated around the world using observations, theoretical, numerical and experimental studies. Hence, Klinck [98] showed that submarine canyons can enhance upwelling/ downwelling in coastal regions using a numerical model. She and Klinck [27] also applied a

numerical model to describe the circulation over submarine canyons driven by constant up/ downwelling wind stress. Vlasenko et al [24] showed that energy focusing greatly intensifies local diapycnal mixing that leads to local formation of a baroclinic eddy, using both observational data and numerical modelling, in the Petite Sole Canyon in the Celtic sea. Zhao et al [99] investigated the energetic characteristics of internal waves and turbulent mixing in the Monterey submarine canyons from observations. Palanques et al [100] studied the transport of suspended sediments in seven submarine canyons of the Gulf of Lion from observations. Hickey [28] studied the response of Astoria canyon to strong forcing using also observational data, and found that a cyclonic circulation pattern occurred in the canyon. Many of observational studies focused on tides and internal waves and the effect of currents in and near submarine canyons on sediment distribution and resuspension [94, 101, 102]. Moreover, these studies showed that canyons can influence circulation on the adjacent continental shelf [22]. Allen and Hickey [103] realized a theoretical study about the dynamics of upwelling over submarine canyons.
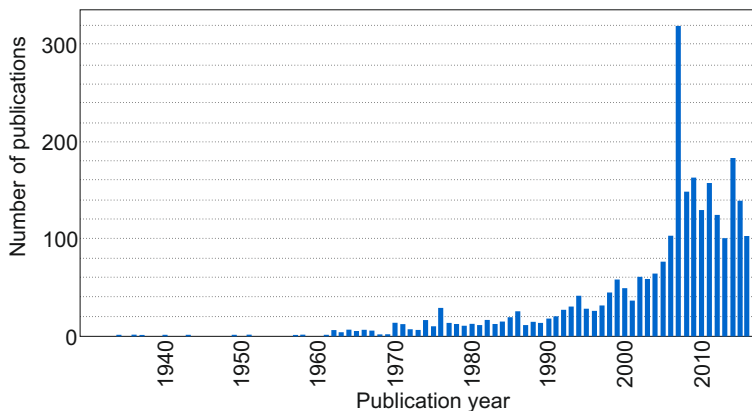
Figure 3.1: *Number of publications records in the Web of Science database related to the search topic 'submarine canyon' as of October 2016. Source: University of Granada.*

Accordingly, because it is know that when the flow passes over a submarine canyon it may generate cyclonic and anticyclonic eddies, upwelling and flow convergence, and internal waves, in this part of the Thesis the dynamic of the Jolúcar submarine canyon were analyzed. The main objective of this Part is to study the hydrodynamic processes of a submarine canyon in the Alborán sea using both observational data and theory, and their associated frequencies. The specific purposes are the following: 1) to study the general circulation of

the submarine canyon; 2) to know the main forcings that control the canyon circulation, concretely the role of the atmospheric forcing that includes the atmospheric pressure gradients; 3) to analyze the existence of internal waves and the vorticity in the canyon. Therefore, in this Part II the research questions 3. and 4. defined in section 1.2 are answered to achieve the main goal of this Thesis.

3.2 Flow dynamics in submarine canyons

The head of Jolúcar canyon reaches the depth of the continental shelf before the coast and then, it can be considered a short canyon [28]. Flow dynamics in short canyons have been quite studied and documented [28, 29, 104]. Figure 3.2 describes the general circulation over a submarine canyon during upwelling-favourable conditions. This Figure is recreated from the results of [103]. The near surface flow is unaffected by the canyon and passes directly over it [103]. As flow just above the depth of the canyon rim (shelf flow in Figure 3.2) crosses the canyon wall, its water columns drop into the canyon, fluid columns stretch, and cyclonic vorticity is generated due to conservation of potential vorticity [107].
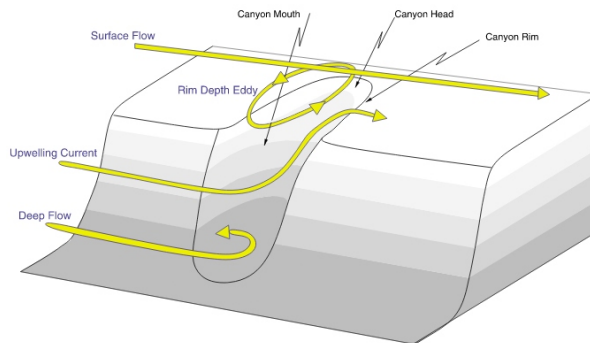
Figure 3.2: Schematic of the flow around a submarine canyon by Allen et al [29] , recreated from [103] . The surface flow, shelf flow (rim depth eddy), deep flow and upwelling current are shown.

The generation of cyclonic vorticity is also linked to separation of flow at the canyon mouth, which advects into the canyon [108]. Flow over the continental slope at the depth of the rim (upwelling current inf Figure 3.2) turns into the canyon and upwells over the downstream canyon rim near the head [104]. Below the slope water that is upwelled (deep flow in Figure 3.2), flow is stretched within the canyon leading to deep cyclonic vorticity [28]. Most upwelling processes in short canyons occur during upwelling favourable wind events [28]. Thus,

upwelling requires that shelf flow be in the direction opposite to the propagation of Kelvin and continental shelf waves.

In the next chapters, based on observational data analysis, the characterization and the analysis of the circulation of Jolúcar canyon were studied by analyzing the main processes affecting it. Results were compared with the general circulation of short canyons previously described. Understanding the flow dynamics will help to describe how local patterns and biology will be affected by this unique topographic feature and the region surrounding Jolúcar canyon.

3.3   Scaling analysis

In order to determine the dynamics in canyons, stratification and rotation parameters are necessary to be studied [104]. Dimensionless numbers can represent the essential dynamics of a submarine canyon because they reflect, among others, the importance of these parameters. Thus, in this section, a scaling analysis was realized, and the main dimensionless numbers were calculated for Jolúcar submarine canyon. These dimensionless numbers were used to compare with another canyons around the world. Moreover, a scale analysis of the governing equations of movement and continuity was realised to estimate the forces and thus the processes that are likely to be important. The dynamic parameters that were considered are the incident flow over the canyon U, the Coriolis parameter f, the stratification characterized by the buoyancy frequency N, and the coefficient eddy viscosity A_v. In addition, key parameters that describe the geometry of the canyon were also considered, canyon length L_c, canyon width W, the half width W_m, canyon width at the shelf break W_{sb}, the axial bottom depth H_c, the depth at the head of the canyon H_h, the depth at the shelf break, H_{sb}, the radius of curvature of the upstream isobaths $\mathcal{R}$, and continental shelf slope s. Geometrical parameters were estimated following Howatt and Allen [105]. Thus, L_c was considered as the length from the shelf break to the head of the canyon; W was estimated at half of the length of the canyon; an alternative to $\mathcal{R}$ is the width of the canyon at the canyon rim $\mathcal{R}_w$, which is measured at half of the canyon length, and it is bounded by the shelf break depth contour. Continental shelf slope was calculated by considering the topographic slope from the coast to the shelf break of the canyon. Geometric parameters were derived from the batymetric map (Figure 1.3b).

The nondimensional numbers formed on the basis of these scales that best characterize the dynamic of a submarine canyon are:

Rossby numbers Ro=$U/f\text{L}_c$ and Rc=$U/f\mathcal{R}$, are the ratio of magnitude of the inertial term to the Coriolis force on length scales of the canyon. Each Rossby number is characterized by the same horizontal velocity and rotational term.

Froude number Fr=U/NH_{sb}, which estimates the relative importance of the stratification in the canyon.

Burger number Bu=$(\text{Ro/Fr})^2=(NH_{sb}/f\text{L}_c)^2$, is the ratio of the above numbers squared, and it determines the significance of stratification. Burger number can also estimate from Bu=$(\text{Rc/Fr})^2=NH_{sb}/f\mathcal{R}_w$.

Ekman layer Ek=δ/H_{sb}, where δ is the thickness of the bottom Ekman layer, estimates the relative strengths of vertical viscous effects and rotational processes.

These numbers were used to determine the importance of Coriolis force, stratification, and frictional processes, and their impacts on flow dynamics of the Jolúcar canyon.

Characteristic values used to estimate dimensionless numbers for Jolúcar canyon and the approximate values of above numbers are included in Table 3.1. Nondimensional numbers for different submarine canyons around the world is displayed in Table 3.2.

Table 3.1: *Physical variables and nondimensional numbers for Jolúcar canyon.*

Physical variables and dimensionless numbers	Jolúcar canyon
Canyon length (km)	8
Canyon width$_{sb}$ (km)	3
Shelf break depth (m)	320
Canyon slope (°)	0.08
Buoyancy frequency (s^{-1})	0.01
Coriolis frequency (s^{-1})	$8.69x10^{-4}$
Rossby number $Ro = U/fL$	0.13
Rossby number $Rc = U/f\mathcal{R}$	0.7
Froude number $Fr = U/NH_{sb}$	0.17
Burger number $Bu = (Ro/Fr)^2$	0.15
Burger number $Bu = (Rc/Fr)^2$	4.4
Ekman number $Bu = (Rc/Fr)^2$	0.4

Numbers of Jolúcar canyon suggest that canyon Rossby numbers are less than unity. Therefore, rotational processes play an important role in the canyon processes, in agreement with previous studies [26, 28, 98]. The relative influence of the stratification varies from negligible (Bu=0.15) to relatively strong (Bu=4.4),

Table 3.2: *Nondimensional numbers for different submarine canyons around the world.*

Dimensionless numbers	Astoria	Juan de Fuca	Barkley	Tidra	Quinault
Ro	$0.05 - 0.6$	xx	xx	xx	xx
Rc	0.44	0.12	0.19	1.1	0.04
Fr	0.81	0.12	0.1	0.33	0.14
Bu_{Ro}	0.51	xx	1	xx	xx
Bu_{Rc}	1.2	0.17	0.1	0.33	0.14
Ek	0.33	xx	xx	xx	xx

and the canyon Froude is less than unity. Thus, stratification can be expected to have some influence of the canyon processes [106].

Another non-dimensional parameters were also considered: the aspect ratio (H_c/W_m) and the vertical aspect ratio or fractional height (h_m/H_c), the internal Rossby radius of deformation ($R_d=NH_c/f$), the stratification parameter ($S=NH_c/fW_m$), and the vertical stratification scale ($Tr=fW_m/N$). For Jolúcar canyon, the aspect ratio is 0.4, and the fractional height is 0.6. For the observed average incident flow over the period considered, R_d is about 60 km, S parameters varies from 20-40, and the Tr scale ranges from about 13 to 23 m.

Jolúcar canyon is very narrow, because the canyon width is much less than the internal Rossby radius of deformation. Jolúcar canyon is also deep, that is, the depth of the canyon below its rim is roughly three times the depth of the incident flow (450 m versus 150 m).

4

Atmospheric forcing in Jolúcar canyon

*T*his *Chapter determines the role of tides and, specially, small-scale atmospheric forcing, which includes both wind and atmospheric pressure gradient, on the vertical structure of currents in the Jolúcar submarine canyon. Results are obtained using data analysis of field observations. Regarding atmospheric forcing, an analytical model is also derived, that consists of the linearized hydrodynamic equations for non-homogeneous, rotating, viscous flows. The classical analytical solution of wind-induced current profile is extended to include the influence of pressure gradients.*

4.1 Field observations

The main processes affecting the circulation of Jolúcar submarine canyon were analyzed using data of two field studies (Figure 4.1). Specifically, in this chapter, tides, up/downwelling and atmospheric forcing were studied. Field measurements were recorded over a 7 day period in November, 2010 at various locations of the submarine canyon (Figure 4.1). Moreover, data from two 6 hours cruise were also obtained at the Jolúcar canyon on 7 June. Four transects were sampled repeatedly during the cruise (Figure 4.1, T1-T4) over a tributary of the canyon, near the canyon head. Simultaneous measurements of the

atmospheric forcing (barometric pressure and wind speed and direction) and the hydrodynamic response (free surface elevation and current profiles) were recorded during sampling periods. A detailed description of the field surveys, instruments, and measurements are found in the Appendix C.
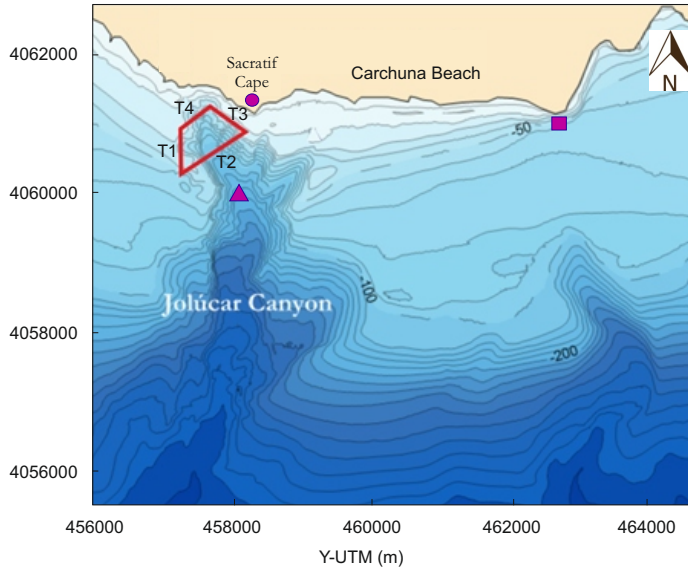
Figure 4.1: Contour map of the study site showing the bathymetry. Triangle and circle indicate the location of the instrument and meteorological station during the 7 days field survey. Additional atmospheric pressure data were obtained from the European Centre of Medium-Range Weather Fore Casts (ECMWF) (purple square). Red squares indicates the closed trajectory consisting of four transects T1-T4, respectively, during the 6 hours cruise.

4.2 Data analysis

Standard harmonic analysis of the complex current velocities [63] was applied to currents data to separate both tidal and atmospheric forcing. Rotary spectral analysis was applied to study the behaviour of tides with depth.

An Empirical Orthogonal Function (EOF) analysis was applied to decompose the vertically sheared horizontal currents into modes [109] to obtained the main dominant modes that drive the Jolúcar canyon circulation. The EOF analysis was applied to concatenated velocity components. The relationship between those dominant modes and both wind and atmospheric pressure gradients was expressed in terms of spectral analysis, wavelets, coherence squared Φ^2 and Cross Wavelet Transform (XWT) to identify the frequencies common variability

in the data records. The 95 % confidence levels were also determined following Koopmans [79] and Torrence and Compo [110] for statistical significance.

The detailed description of the analysis procedures is found in the Appendix A.

4.3 Circulation driven by wind stress and pressure gradient

The classical analytical solution of wind-induced current profile [111] was extended here by considering the superposition of bottom and surface Ekman layers, and including the influence of barotropic pressure gradients in a non-homogeneous water column. To derive an analytical solution, we assume the vertical eddy viscosity temporally and vertically constant and independent of the flow, and a flat bottom. Considering linear and stationary motion, and for simplicity's sake, the momentum equations on the f-plane can be written as:

$$-f\hat{v} = -\frac{1}{\rho}\frac{\partial P}{\partial x} + \frac{\partial}{\partial z}\left(A_v\frac{\partial \hat{u}}{\partial z}\right) \tag{4.1}$$

$$+f\hat{u} = -\frac{1}{\rho}\frac{\partial P}{\partial y} + \frac{\partial}{\partial z}\left(A_v\frac{\partial \hat{v}}{\partial z}\right) \tag{4.2}$$

where coordinates x, y are positive to South and East, respectively, and z is negative downward, with $z = 0$ at the surface; the horizontal components of the current $\hat{u}$ and $\hat{v}$ are functions of z; ρ is the water density; P is the pressure; and A_v is the vertical eddy viscosity coefficient. It was also assumed that ρ is a weak function of depth $\rho(z) = \rho_0 \exp(-z/z_0)$, where ρ_0 is $1027\,\mathrm{kg\,m^{-3}}$, and $z_0=$ 10^4 m is estimated from temperature and salinity data at various depths from the World Ocean Atlas (WOA) 2013 $1/4°$ x $1/4°$ monthly means at approximately $36.38°$ N, $3.12°$ W [112] (Figure 4.2). Since $z_0^4 \gg H$, where H is the canyon depth, the vertical gradient is small. The pressure gradient $\left(\frac{\partial P}{\partial x}, \frac{\partial P}{\partial y}\right)$ contains a barotropic component due to differences in water level. It also includes the atmospheric pressure gradient (barometric component) and a baroclinic component due to horizontal density gradients. Horizontal density gradients are on the order of 10^{-6} $\mathrm{kg\,m^{-3}}$, which were estimated using temperature and salinity measurements from WOA 2013. Then, baroclinic pressure gradients are negligible. The vertically integrated continuity equation is implicitly included in the model with the boundary conditions.

Surface boundary conditions are $\partial(\hat{u}, \hat{v})/\partial z|_{z=0} = \left(\tau_w^x, \tau_w^y\right)/(\rho\,A_v)$, where τ_w^x and τ_w^y denote the x and y components of the wind stress. Slip boundary
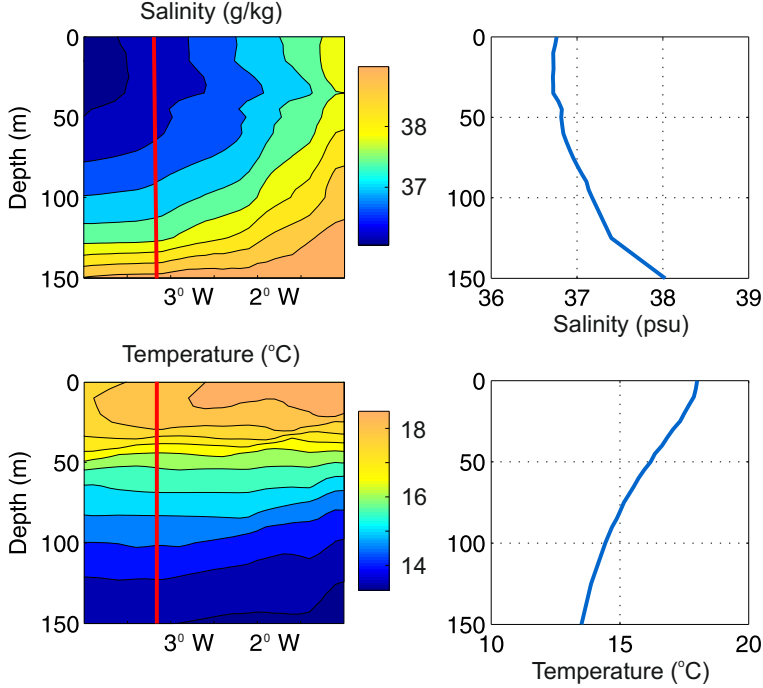
Figure 4.2: Left panels: temperature and salinity data at various depth estimate from the World Ocean Atlas 2013 1/4° x 1/4° monthly means at 35-40°N, 5-0°W. Right panels: temperature and salinity profiles at approximately 6.38° N, 3.12° W, which is indicated with red line in left panels.

conditions are assumed at the bed, i.e., $\left(\tau_b^x, \tau_b^y\right)$ = -$\rho A_v \partial(\hat{u}, \hat{v})/\partial z|_{z=-H}$, where bottom stresses $\tau_b^{x,y}$ are estimated using a quadratic drag law, $\left(\tau_b^x, \tau_b^y\right)$= $C_d(\hat{u}_b|U_b|, \hat{v}_b|U_b|)$, where $(\hat{u}_b, \hat{v}_b)$ are the northward and eastward current velocity components measured closest to the bottom, respectively, U_b is the current speed, and C_d=$3 \cdot 10^{-3}$ is the non-dimensional bottom drag coefficient. Combining equations (1) and (2) in favor of $\hat{u}$, the following governing equation is obtained

$$\frac{d^4\hat{u}}{dz^4} + \frac{f^2}{A_v^2}\hat{u} = -\frac{\partial P}{\partial y}\frac{f}{A_v^2\rho} + \frac{1}{A_v}\frac{\partial^2}{\partial z^2}\left(\frac{1}{\rho}\frac{\partial P}{\partial x}\right) \tag{4.3}$$

Equation (3) is a fourth order linear non-homogeneous differential equation for $\hat{u}$ assuming that the pressure gradient $(\partial P/\partial x, \partial P/\partial y)$ is prescribed. Scaling z as $D_E/\sqrt{2}\hat{z}$, where D_E=$\sqrt{2A_v/f}$ is the frictional layer depth or Ekman depth, equation (4.3) for $u(z)$ is simplified and its solution is given by

$$u(z) = -\frac{1}{\rho_0 f}\frac{\partial P}{\partial y}e^{z/D_E} + \sum_{n=1}^{4}\tilde{c}_n e^{\beta_n z/D_E} \tag{4.4}$$

Here $\beta_n = \cos[(2n+1)\pi/4]$, and $\tilde{c}_n$ are constants to be determined applying the four boundary conditions, and $n=0,1,...$ Thus, the homogeneous solution is related to wind forcing (consistent with Ekman dynamics), and a particular solution is associated to the pressure gradient. The v velocity component is obtained from $u(z)$ using equation (1)

$$v(z) = -\frac{1}{\rho_0 f}\frac{\partial P}{\partial x} - \frac{A_v}{f}\frac{\partial^2}{\partial z^2}\left(-\frac{1}{\rho_0 f}\frac{\partial P}{\partial y}e^{z/D_E} + \sum_{n=1}^{4}\tilde{c}_n e^{\beta_n z/D_E}\right) \tag{4.5}$$

The entire procedure of the equations development is found in the Appendix B. This analytical solution of the currents u and v will be compared with field measurements in the next section.

4.4   Results

4.4.1   Tides

To know the importance of tides in the circulation of Jolúcar canyon and the characteristics and spatial variability of surface tides, harmonic analyses were performed to horizontal current data. The harmonic tidal constituents account for about 10 % of the currents variability, whereas the residual part explains the remaining 90 % of the Jolúcar currents variability. The length of the time series were insufficient to separate M2 and S2, the most important semidiurnal constituents. In this chapter, their join contribution was considered, and is called M2. The tidal analysis provides the semimajor and semininor axis, ellipse orientation, and Greenwich phase for the two main tidal constituents M2 and K1 (Figure 4.3). Moreover, eccentricities (semiminor axis/ seminajor axis) and tidal ellipses are shown in Figure 4.4. Tidal ellipses display a range of eccentricities (Figure 4.4) and orientations (Figure 4.3c). However, there is a trend of decreasing tidal amplitude towards the bottom, consistent with dominance of bottom friction process (Figure 4.3 a). It is interesting to note that eccentricity of the semidiurnal tidal constituent varies in a wide range of -0.32 and 0.22 values (Figure 4.4, left panel). This means that the M2 tidal flow is influenced by the canyon walls [113]. Moreover, the eccentricity of ellipses is low, indicating the

ellipses are quite rectilinear. The Greenwich phase provides the tidal forcing local response at the reference longitude of the Greenwich Meridian. For the studied tidal constituents, phase changes are observed (Figure 4.3d). For the M2 tidal constituent the phase change is about 110° between 100-120 m depth, and 110° at about 60 m depth . For the K1 tidal constituent, the phase change is about 50° over 100-120 m depth, and about 50° at about 30 m depht. The observed phase changes with depth indicate that the tides have a baroclinic component, since a purely barotropic tide would have equal phase at all depths [114]. The phase changes with depth of the tidal constituents are also related to the position of the pycnocline. In general, ellipses are nearly rectilinear (Figure 4.4, right panels) and then, the seminimor axis is negligible compared to the semimayor axis.
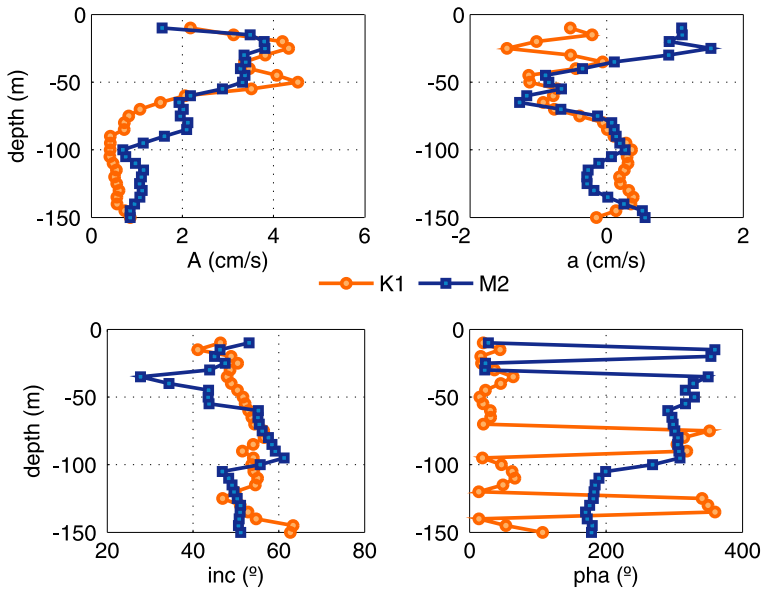
Figure 4.3: *Vertical profiles of (a) semimajor axis A, (b) semiminor axis a, (c) orientation ψ, and (d) Greenwich phase φ derived from harmonic analysis. Profiles for the M2 tide are shown in blue (square), and profiles for the K1 tide are shown in orange (circle).*
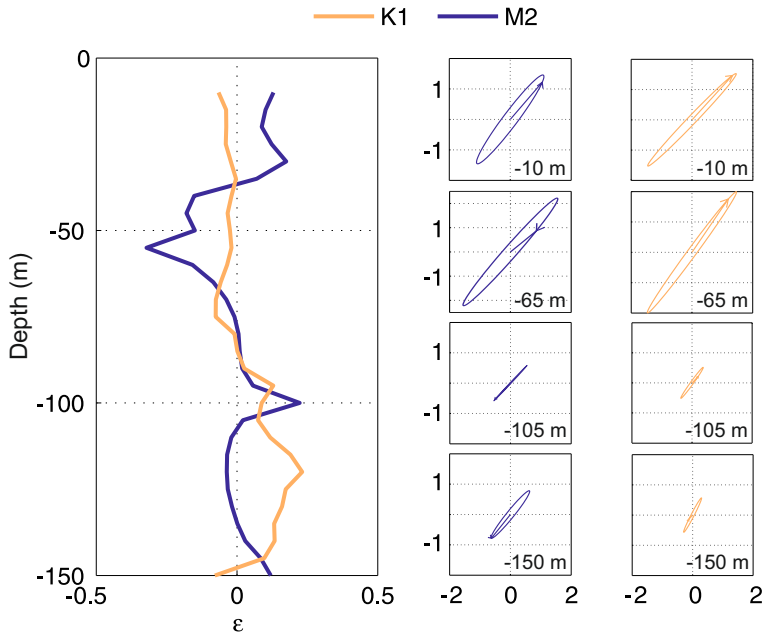
Figure 4.4: *Left panel: vertical profile of both diurnal and semidiurnal tidal constituents eccentricity (semi-major axis/ semi-minor axis). Rigth pannels: semidiurnal (left) and diurnal (right) tidal ellipses derived from harmonic analysis of the full length velocity records at 10, 65, 105, and 150 m depth.*

4.4.2 Atmospheric forcing

As commented above, the residual part from the harmonic analyses accounts for the 90% of the Jolúcar currents variability.

The general behaviour of the Jolúcar canyon currents is analyzed by studying the time series of currents and wind direction, and the current roses. Figure 4.5 shows that Western winds were predominant during the field survey. Eastern and Northern winds also blew during the time period studied.
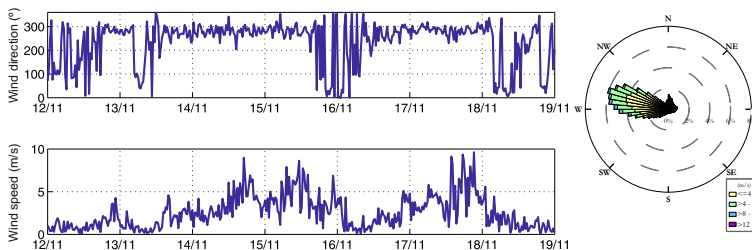
Figure 4.5: *Speed components and direction wind time series, and wind rose at 10 m above sea level. Data obtained from the meteorological station located in the Sacratif Cape (see Figure 4.1, circle).*

Current roses (Figure 4.6, left panels) display that the measured distribution of current direction and speed into the canyon shows a different behaviour of the current direction with depth. Significant changes in the speed currents profiles exist. During the westward wind period (Figure 4.6,right panel a), currents travel in the same direction than wind in the surface layer, at 10 m depth (surface flow in the Figure). In contrast, in the inversion layer, at about 60-75 m depth (intermediate flow in the Figure), currents travel in opposite direction than wind and are upwelled onto the shelf. In the bottom layer, at 140-150 m depth (deeper flow in the Figure), current travel in the same direction than wind and are downwelled within the canyon.
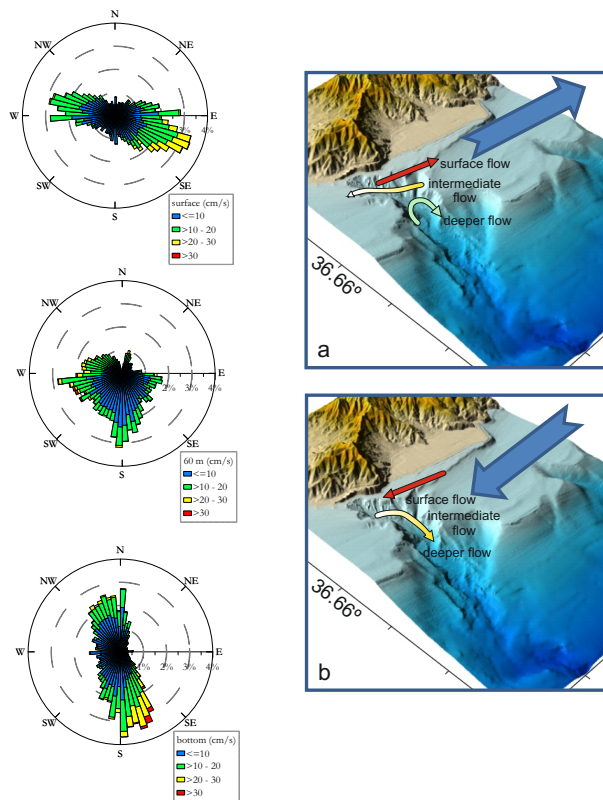
Figure 4.6: Left panels: current roses representing the measured distribution of canyon currents direction and speed at surface, 60-75 m depth, and bottom. Right panels: distribution of canyon currents directions with depth during both a predominant eastward wind (upper panel), and a westward wind (lower panel). Blue arrows indicate the wind direction.

On the other hand, during the eastward wind period (Figure 4.6, right panel b), a different behaviour of the canyon circulation is observed. Thus, currents also

travel in the same direction than wind in the surface layer (surface flow in Figure). In the inversion layer (intermediate flow in the Figure), current travel in opposite direction than wind but are downwelled onto the shelf. In the bottom layer, at 140-150 m depth (deeper flow in the Figure), current also travel in the same direction than wind and are downwelled within the canyon. It is interesting note that at 60-75 m depth, currents are downwelled into the basin for both western and eastern winds. Figure 4.7 also shows the behaviour of daily flow with depth during the field survey. Flow is downwelled into the canyon at 60 m depth. Then, the Jolúcar canyon might acts as a seaward pathway, during the field survey, to any type of substances. These results show that up/downwelling processes exist in the canyon, and that the circulation into the Jolúcar canyon could be affected by the wind forcing.
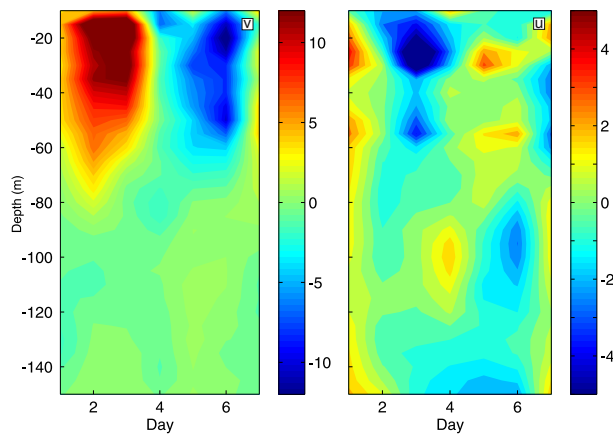
Figure 4.7: *Vertical behaviour of the daily averaged eastward v (left panel) and the northward u (right panel) currents components during the field survey.*

Figure 4.8 displays the relationship between u and $(1/f\ \partial^2 v/\partial z^2)$ terms of the Ekman dynamic equations for different depths. Data were fitted applying a least squares fitting technique, by using a polynomial curve of degree 1 of the form c(x)=p1(x)+p2, where p1 and p2 are the coefficients (with 95% confidence bounds) of fit results. The first coefficient p1(x) of fit results give the magnitude order of A_v. Results are shown in Table 4.1. If p1(x)≫p2, wind forcing could dominate currents variability in the canyon. Results show that the magnitude order of both p1 and p2 is similar ($O(10^{-3})$ m^{2}s^{-1}), indicating that there are another processes influencing the canyon circulation.

In order to obtain a more detailed information about the circulation in the study site, and thus to know the main forcings driving the circulation in the
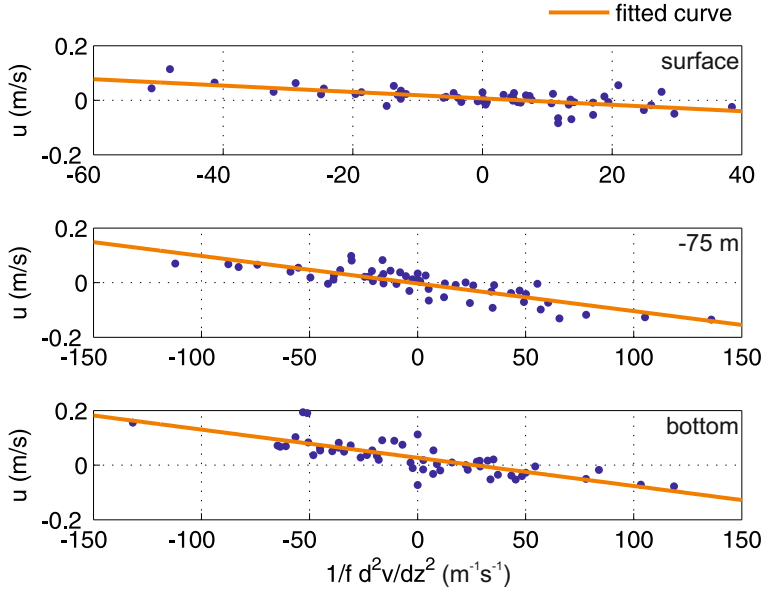
Figure 4.8: *Relationship between u and (1/f ∂²v/∂z²) terms of the Ekman dynamic equations at surface, 75 m depth, and bottom. Orange lines indicate fitted curves applying a least squares fitting technique, by using a polynomial curve of degree 1.*

Table 4.1: *Coefficients (with 95% confidence bounds) of fit results of Figure 4.8 using a polynomial curve of degree 1 as c(x)=p1(x)+p2. The coefficient of determination R^2 is also shown.*

Coefficients	Surface	75 (m) depth	Bottom
p1	-0.001	-0.001	-0.001
p2	0.006	-0.003	-0.002
R^2	0.5	0.70	0.62

Jolúcar canyon, an EOF analysis was realized. The EOF analysis was applied to decompose the vertically sheared horizontal currents into modes [109], and it was applied to concatenated velocity components. Figure 4.9a-b shows the vertical structure of the horizontal currents during the field deployment (in colours). Black contours represent re-constructed currents with only the first two eigenmodes. Figure 4.9c-d panels shows the time series of $g_1(t)$ and $g_2(t)$. Figure 4.10 (circles and squares) show that the first two eigenmodes of the current velocity ($v^{(1)}, v^{(2)}$, and $u^{(1)}, u^{(2)}$, for the eastward and northward components, respectively) represent the spatial structure of the observed currents. The EOF analysis indicates that the first and second eigenmodes account for 65 % of the variability (black contours in Figure 4.9a panel). No significant modes are found related to tides, whose vertical structures are expected to be barotropic.
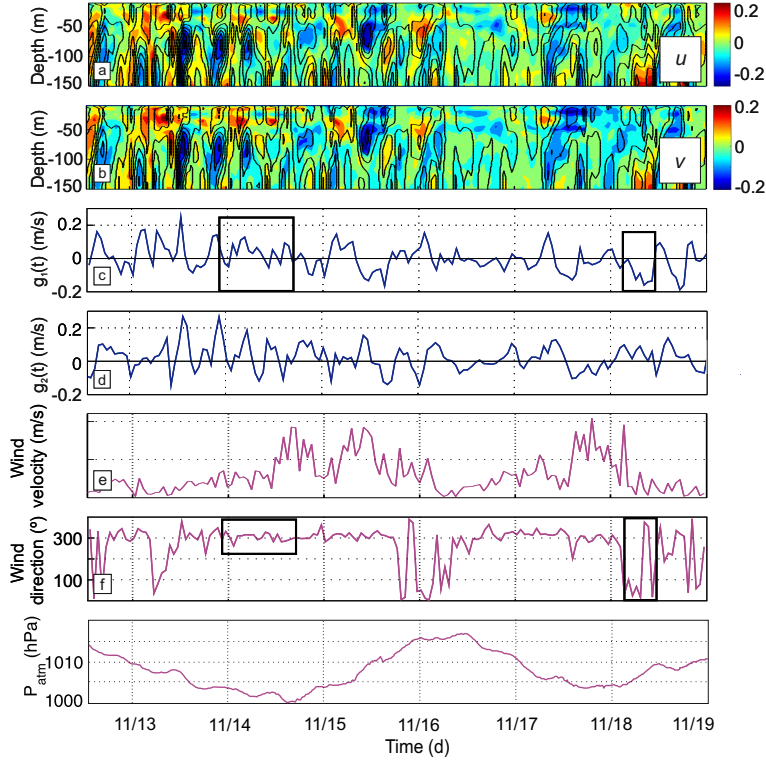
Figure 4.9: *Panels (a-b): vertical behaviour of the northward u (panel a) and the eastward v (panel b) current components during the field survey (colors). Black contours show re-constructed currents considering only the first two empirical orthogonal modes. Panels (c-d): time series of $g_1(t)$ and $g_2(t)$ associated with the first and second empirical modes, respectively. Panels (e-f): speed and direction wind atmospheric pressure time series (e and f, respectively). The rectangles in panels (c) and (f) indicate the events discussed in the text. Panel (g): atmospheric pressure time series.*
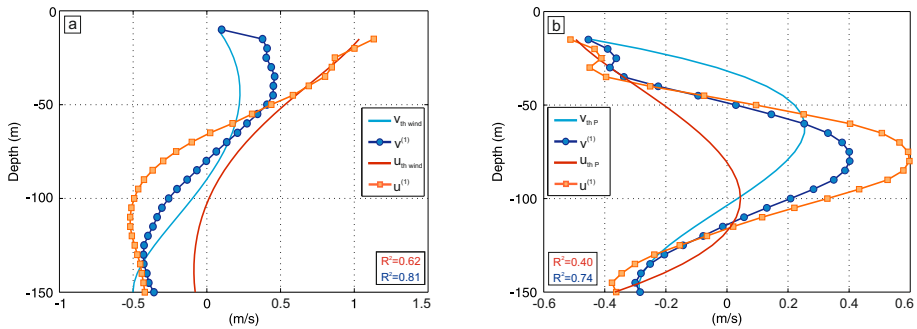
Figure 4.10: *Comparison between observations and analytical model results. Left panel: vertical structure of $u^{(1)}$ (squares) and $v^{(1)}$ (circles), and the theoretical u (orange line) and v (blue line) wind-induced current profiles calculated from the analytical model. The coefficient of determination R^2 is shown. Right panel: the same as left panel for vertical structure of $u^{(2)}$ (squares) and $v^{(2)}$ (circles), and the theoretical atmospheric pressure gradient induced profiles.*

Regarding the vertical structure of $u^{(1)}(z)$ and $v^{(1)}(z)$ (Figure 4.10a panel), a different behaviour is observed between the surface and the bottom. Negative values appear at the bottom and positive at the surface, for both u (Figure 4.10a panel, squares) and v (circles) components. These vertical structures reminisce the classical structure of Ekman dynamics [111]. This is confirmed by the time series, $g_1(t)$, of the first mode (Figure 4.9c panel). Although wind and atmospheric pressure were collected during a period of relatively calm conditions (Figure 4.9e-g panels), up/downwelling processes can be identified. Values of $g_1(t)$ covary with wind direction, showing up/downwelling alongshore processes (marked with black rectangles in Figure 4.9c,f panels).

The vertical structure of $u^{(2)}$ and $v^{(2)}$ present the same behaviour at the surface and at the bottom, showing negative values at both the surface and bottom, and positive values at intermediate depth, attaining their maxima at -75 m (Figure 4.10b panel, squares for u and circles for v). The vertical structures, along with the time variations of $g_2(t)$ (Figure 4.9d panel), show that mode 2 cannot be associated to tides or to wind forcing. The power spectra, wavelet, cross wavelet transform XWT and the coherence squared Φ^2 analyses provide clues on the driving mechanisms of the vertically-sheared currents described by this mode.

The XWT (Figure 4.11a$_1$-b$_1$) shows common spectral power between $g_1(t)$ and $g_2(t)$, and the wind and atmospheric pressure gradients time series (shown in Figure 4.9). The correlation between power spectra of these time series is represented by Φ^2 as shown in Figure 4.11a$_2$-b$_2$. The XWT and Φ^2 between $g_1(t)$ and the alongshore wind stress have three common peaks at 1, 2 and $\sim$6 d^{-1} (horizontal dashed lines in Figure 4.11a$_1$-a$_2$ panels), corresponding to periods of 24, 12 and 4 h, respectively. These results indicate that wind forcing and currents in the submarine canyon are closely related at specific frequencies, as already observed by [26, 115].
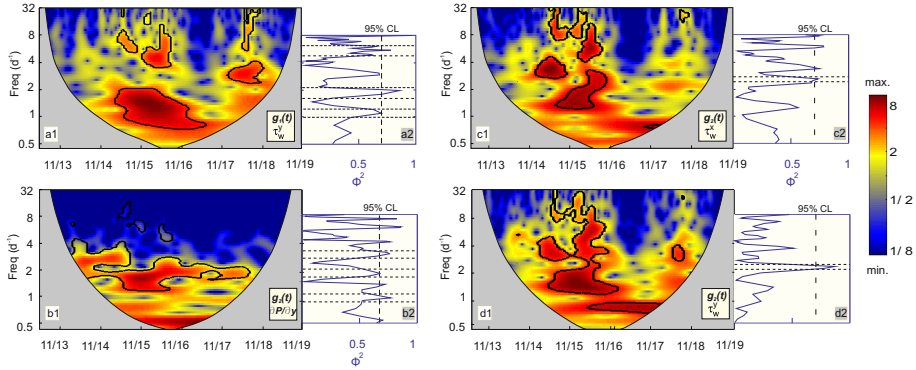
Figure 4.11: *Panel (a): Cross wavelet transform XWT (panel a_1) and coherence squared Φ^2 (panel a_2) of the temporal structure $g_1(t)$ and the alongshore τ_w^y time series. The 5% significance level against red noise is shown as a thick contour. The cone of influence where edge effects might distort the picture is shown as a gray shade. The units on the color bar scale are nominal (red is maximum and blue is minimum energy). The vertical dashed line on the right panels represents the 95 % confidence limits (CL) for the coherence. Horizontal dashed lines refer to the common significant frequencies between the time series. Panel (b): The same as panel (a) for $g_2(t)$ and the atmospheric pressure gradients time series. Panel (c): The same as panel (a) for $g_2(t)$ and the onshore τ_w^x time series. Panel (d): The same as panel (a) for $g_2(t)$ and the alongshore τ_w^y time series.*

Figure 4.12 shows the wavelet of the local atmospheric pressure gradient (panel a) and the spectral analysis of the mode 2 (panel b). Most of energy is concentrated in the 6-12 h band in both cases. This suggests a relation between the vertical structure of currents and the atmospheric pressure forcing generated locally. Moreover, Figure 4.11b_1-b_2 panels also show three common peaks at a frequency of 1, 2 and 3 d^{-1} (periods of 24, 12 and 8 h, respectively) between $u^{(2)}$ and $v^{(2)}$ of the second mode, and the local atmospheric pressure gradients. Mode $g_2(t)$ shows high common power and significant coherence with the atmospheric pressure gradients. Therefore, the circulation associated with mode 2 should be induced by local atmospheric pressure gradients. This suggests that $\lambda_{P_{\text{atm}}} \lesssim L$, where $\lambda_{P_{\text{atm}}}$ is the spatial scale of the local atmospheric pressure over the canyon length L. The argument for small scale of the atmospheric pressure gradients is supported by comparing the local atmospheric pressure near the canyon with the atmospheric pressure in Adra (Figure 4.13). It can be seen that the two time series are decoupled.

Figure 4.11c-d shows the relationship between $g_2(t)$ and both the onshore and alongshore wind stress using XWT and Φ^2. Across-shore wind stress and $g_2(t)$ display a significant peak at 3 d^{-1}, which is also found between $g_2(t)$

and atmospheric pressure gradients (Figure 4.11 b). These results suggest that atmospheric pressure gradients and local wind velocity are related to each other and that local atmospheric pressure gradients should be coupled with local wind velocity.
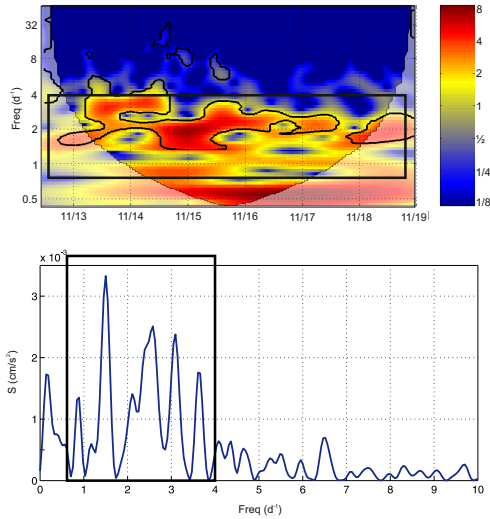
Figure 4.12: *Wavelet of the local atmospheric pressure gradient (panel a) and spectral analyses of the eigenvalues of the second EOF mode. Most of the energy signal is concentrated in the 6 h-24 h band (black squares).*
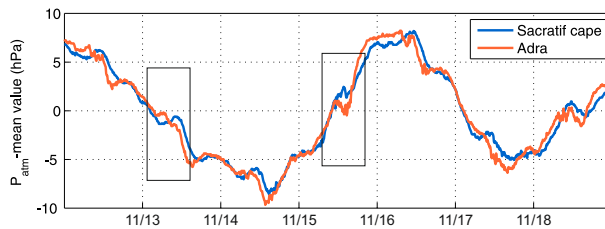
Figure 4.13: *Time series of atmospheric pressure data at Sacratif cape (blue line) and Adra (orange line) during the field survey. Black rectangles point maximum peaks in the atmospheric pressure at both regions.*

The stationary analytical solutions derived in section 4.3, equations (4.4) and (4.5), can be applied to examine the influence of both barotropic and barometric pressure gradients forcing on the vertical structure of currents in the submarine canyon. The XWT and Φ^2 analyses indicate that canyon circulation can be partly related to small-scale barometric pressure gradients. The influence of the barotropic pressure gradient component, however, remains unresolved because

of lack of measurements on water elevation at more than one point. Therefore, only barometric pressure gradients are taken into account in equations (4.4) and (4.5). Figure 4.10 shows the vertical profiles of $u^{(1)}$ and $u^{(2)}$ (squares, in panels a and b, respectively) and $v^{(1)}$ and $v^{(2)}$ (circles, in panels a and b, respectively) of horizontal current components determined from the EOF analysis of observations, and the theoretical currents induced by both wind (solid lines in panel a) and atmospheric pressure gradient (solid lines in panel b), as obtained from equations (4.4) and (4.5). The best match between the analytical profiles and those from the EOF analyses was obtained by applying a least squares fitting technique, using A_v and the bottom slip condition as fitting parameters. Best fits were calculated separately for the effect of wind and atmospheric pressure gradient forcings. Values of wind stress and atmospheric pressure gradients were prescribed from the prevailing atmospheric conditions in the study area during the field survey. These were wind velocity of 5 m/s with predominant eastward direction, and atmospheric pressure gradient of 10^{-2} Pa/m. The latter value was obtained from the difference between the meteorological station at the Sacratif Cape and the ECMWF (Figure 4.1, circle and purple square, respectively). The fitted A_v values were 0.004 m^{2}s^{-1}, and 0.006 m^{2}s^{-1} for wind (first mode) and barotropic pressure gradient forcing (second mode), respectively. The coefficient A_v is assumed independent of the depth and of the particular eigenmode. These values, that are calculated using the expression $A_v = 1.4 \cdot 10^{-4} \cdot v_w^2$ [116], where v_w is the wind speed, are comparable to the wind speed during the field survey. A_v values are of the same order than p1(x) and p2 coefficients obtained for the fit Ekman dymanics (Table 4.1). Coefficients of determination R^2 of 0.81 (0.74) and 0.62 (0.40) are obtained for the first (second) mode of the eastward and northward current components, respectively. Overall, the theoretical vertical structure of the currents reproduces the main features of the horizontal currents profiles in the submarine canyon; moreover, the analytical model reveals that the local atmospheric pressure gradient drives the horizontal circulation (mode 2) in the submarine canyon.

4.5 Discussion

The objective of this study is to determine the role of the local atmospheric forcing on the vertical structure of currents in a submarine canyon. Based on this objective, the main forcings that induce the circulation in the Jolúcar submarine canyon are identified by means of observations and analytical solutions. The

available observations show that tidal oscillations dominate the flow field in many submarine canyons [101, 102, 114, 117]. In contrast, results show that tides in the Jolúcar submarine canyon only account for 10% of the total current variability. These results are expected because currents in the Mediterranean basin are generally low from a tidal energy perspective [118].

The vertical structure of the current velocity is isolated applying EOF analysis. The first two empirical orthogonal modes explain most of the variability of the vertical structure of the circulation in the Jolúcar submarine canyon, representing the 65% of the currents. The first mode can be explained by wind forcing, as it has similar patterns to the classical structure of Ekman dynamics and shows up/downwelling related to wind forcing. Mode 2 is largely linked to the local atmospheric pressure gradients, as it shows highest power and coherence with atmospheric pressure gradients at specific frequencies.

The main spectral feature derived from the XWT and coherence squared Φ^2 analysis between the EOF modes and the atmospheric forcing is the presence of statistically significant common peaks at diurnal, semidiurnal, $\sim$ 4h and $\sim$ 8h periods. These periods are typically in the range of daily and local breezes. Even though 24h and 12h periods are known in nearby mountain ranges and coastal edges [11] during atmospheric anticyclones, the origin of both 8h and 4h periods in the atmospheric forcing is more challenging to explain. Possible non-linear mechanisms of local diurnal and semidiurnal wind and atmospheric pressure interactions, from the complex topography of the study area, could induce the spectral peaks at compound periods $\sim$ 8h and $\sim$ 4h. The non-linear terms related to atmospheric forcing in the equations of atmospheric dynamics could generate terdiurnal oscillations from diurnal and semidiurnal interactions, which may explain the period of $\sim$ 8h in the spectra of the atmospheric pressure gradients. These non-linear terms could also generate sixth diurnal oscillations from semidiurnal interactions, which may thus explain the spectral peak at the period of $\sim$ 4h of the wind forcing. Simultaneous continuous records of wind and atmospheric pressure data over longer periods might be required to further explore this hypothesis.

Part of the energy containing the $\sim$ 12h period in the current records is associated with the semidiurnal M2 tides. However, M2 are small compared with non-tidal components and even not detected by the EOF analysis. A standard harmonic analysis [63] shows that, as above mention, only 10% of the total variance resides in the tidal signal. Then, tidal influence on the vertical structure

of currents in the Jolúcar canyon is negligible compared with atmospheric forcing.

In addition to local atmospheric mechanisms, other potential mechanisms for super-inertial variability exist. Resonance could also occur within submarine canyons at super-inertial frequencies, which could explain the observed mode 2 of currents. Following the derivations of [23], Jolúcar submarine canyon is resonant at a frequency of 12 cpd, corresponding to a period of 2 h. Resonant frequency is calculated with temperature and salinity data from the World Ocean Atlas 2013, and a mean bottom slope on the canyon of about 0.08. This resonant frequency, however, is not observed in the mode 2 of currents. Therefore, super-inertial frequencies of the currents are likely related to atmospheric forcing acting directly over the water surface.

The analytical model in this study reproduces well the main features of both mode 1 and mode 2 associated with the wind and the local barometric pressure gradient, respectively. Discrepancies between the analytical and measured current profiles are likely related to the geometry of the canyon (longshore slope and lateral walls), which is not included in the analytical model. For example, Skliris et al [119] associated increases of both cross- shore and vertical transport to canyon topography. Other assumptions that could determine the differences between the model and eigenmodes are: non-linear momentum terms are not included in the equations, which other studies have found to be important in submarine canyons [27]; barotropic pressure component not included in the solutions, and the linear motion assumption; and variations in the vertical eddy viscosity (assumed to be independent of depth).

Notwithstanding, this chapter presents an approach to studying the atmospheric forced response (barometric pressure, wind speed, and direction) of circulation in a submarine canyon. The classical hydrodynamic wind-induced equations required inclusion of barometric pressure gradients in a non-homogeneus water column to emulate the observations.

4.6 Conclusions

This chapter analyzed the circulation of the Jolúcar submarine canyon, including the role of the atmospheric pressure gradient locally generated. The following conclusions can be derived from this research:

1. Only 10% of the total canyon circulation is driven by the tidal signal.
2. Circulation in a submarine canyon can be induced by small-scale (local) atmospheric pressure gradients.

3. Atmospheric pressure gradients induced 1/3 of the horizontal circulation in the Carchuna canyon.
4. The classical hydrodynamic equations required inclusion of barometric pressure gradients to emulate the observations.

5

Internal waves and Vorticity

In a review of submarine canyons, Hickey [97] points out that physical processes can be modified/ enhanced due to the presence of a submarine canyon. Some of these processes include internal waves and vorticity, which is associated with the presence of upward and downward flows. In this chapter, internal waves in the Jolúcar canyon are investigated using data analysis of field observations. Concretely, spectral analyses of echo intensity and currents data are applied to identify and characterize this kind of waves. In addition, the hydrodynamic structure of currents and vorticity parameters is studied using repeated velocity profile of field observations.

5.1 Field observations

The main processes affecting the circulation of Jolúcar submarine canyon were analyzed using data of two field studies (Figure 4.1). Specifically, internal waves were investigated using field measurements recorded over a 7 day period in November, 2010 in the submarine canyon (Figure 4.1, triangle and circle). Echo intensity and currents data were obtained. Regarding vorticity analysis, data from a 6 hours cruise were also obtained at the Jolúcar canyon on 7 June. Four transects were sampled repeatedly during the cruise (Figure 4.1, T1-T4, red

square) over a tributary of the canyon, near the canyon head. Simultaneous measurements of the atmospheric forcing (barometric pressure and wind speed and direction) and the hydrodynamic response (free surface elevation and current profiles) were recorded during sampling periods. Temperature and salinity data were also recorded. A detailed description of the field surveys, instruments, and measurements are found in the Appendix C.

5.2 Internal Waves

Canyons may be both effective conduits for funneling open-ocean internal wave energy onto the inner shelf and sites for generation of internal waves (IW) [94]. From solving the linear set of equations for IW [120], the band frequencies of IW is $f < \omega < N$, such that buoyancy frequency N provides the maximum frequency of IW, and f sets a lower bound of the wave frequency. In order to detect and identify the existence of IW in Jolúcar submarine canyon, currents and acoustic echo-amplitude data of field observations were analyzed.

Echo intensity (ECHO) data were normalized by applying the following transformation:

$$EA = 10log_{10}(ECHO) - \langle 10log_{10}(ECHO) \rangle \tag{5.1}$$

as done in [121]. The angle brackets denoted a time mean and this normalization of the echo intensity will be referred to as the echo anomaly (EA). A vertical gradient of the EA highlighted the possible presence of IW [122]. A spectral distribution of EA with depth was realized to detect the depth dependent structure in the dominant frequencies. Moreover, a wavelet analysis [110] was applied to the EA, and the vertical gradient of the EA. The spatial and temporal variability of the IW energy was found by extracting the amplitude of the wavelet at the IW frequency, which was calculated at each depth. This method of representing wavelet analysis results is called a power Hovmöller diagram [110]. The advantage of the power Hovmöller is that the temporal variations in IWs can be seen at different depths within the water column [122]. By computing the Fourier transform of the time series of the rotary velocity ($u+iv$) a rotary spectrum [123] was computed, with negative and positive frequencies indicating counterclockwise (ccw) and clockwise (cw) rotation in time, respectively. For linear IWs in the northern hemisphere, the cw rotating spectrum is greater than the ccw rotating spectrum [101].

The detailed description of the analysis procedures is found in the Appendix A.

5.3 Vorticity

Narrow canyons have a strong effect on circulation, and are normally characterized by a general cyclonic or anticyclonic circulation within the canyon because of the stretching of water parcels passing over the shelf break [97, 103, 124] (Figure 3.2). In order to analyze if the circulation of the Jolúcar canyon is in agreement with typical circulation of a short canyon, data analysis of field observations was used. These data were also used to calculate the vorticity , which is a physical quantity widely used to characterize fluid rotation.

In order to compute dynamic variables, observations were first compass-calibrated and corrected by the method of Joyce [125] using a Global Positioning System. Eastward and northward velocity components were also linearly interpolated onto a regular 170x170 grid of distance versus depth values [126]. The interpolation was carried out through Delaunay triangulations. The relative vorticity, ξ, was obtained solving numerically the following equations:

$$\xi = \frac{\partial v}{\partial x} - \frac{\partial u}{\partial y}$$
(5.2)

In order to obtain the relative vorticity of each transversal transect, longitudinal and vertical velocity components were used for each transect T1-T4.

The detailed description of the analysis procedures is found in the Appendix A.

5.4 Results

5.4.1 Internal Waves

The buoyancy frequency, N, was calculated from salinity and temperature data up to 150 m depth from the World Ocean Atlas (WOA) 2013 1/4° x 1/4° monthly means at approximately 36.38° N, 3.12° W [112] (Figure 4.2). Thus, the IW frequencies band in Jolúcar canyon is $0.83 < \omega < 130$ cpd, corresponding to periods of 1.2 day and 11 minute, respectively.

The time series of the acoustic echo amplitude (Figure 5.1a,b) are characterized by a diurnal variation in amplitude. The diurnal variation can be caused by the daily vertically migrating of zooplankton, which has a vertical scale of about 120 m depth (Figure 5.1b). The vertical gradient of the echo

anomaly showed sporadic patches of elevated signal around 50-100 m depth. These oscillations could indicate IWs in the Jolúcar canyon (Figure 5.1c). Thus, well defined IW packets were observed, for example, between days 15 and 16, 16 and 17, and 17 and 18 (Figure 5.1b, c, e).
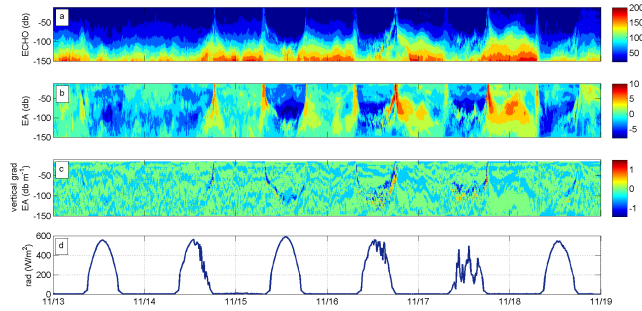
Figure 5.1: Panel a: Echo intensity signal directly from measurements. Panel b: Echo anomaly estimated from 5.1. Panel c: Vertical gradient of the Echo anomaly. Paned d: Radiation data during the field survey.

The time series of the EA and current components, which were band-pass filtered by a fifth-order Butterworth filter with 72-48 cpd cut off frequencies, displayed oscillations with periods between 20-30 minutes (Figure 5.2a-f). These periods are included in the band frequencies of IWs. Therefore, the time series of currents also indicated the presence of IWs with a period of about 20-30 minutes.
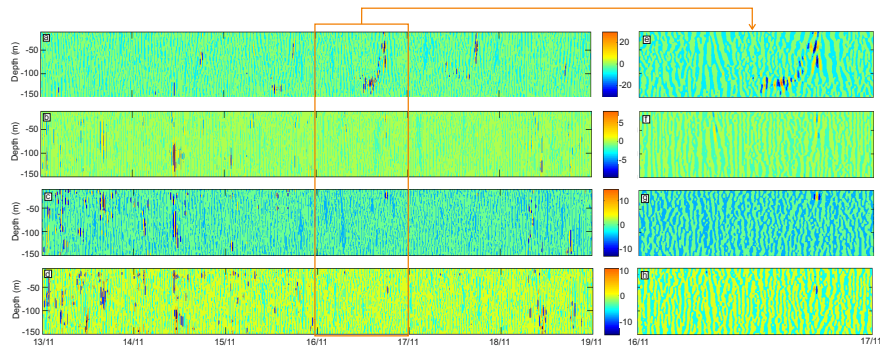
Figure 5.2: Time series of EA (panel a), upward velocity (panel b), eastward velocity (panel c), and northward velocity (panel d) band-pass filtered by a fifth-order Butterworth filter with 72-48 cpd cutoff frequencies. Panels e-h: The same as panels (a-d) for a 1-day segment.

Spectra of EA with depth (Figure 5.3) displayed hight variance at the IW frequency band (55-60 cpd). The highest energies at these frequencies were located between 50 and 120 m depth, and not in the entire water column. It could

see in chapter 4 that there also was a phase change of studied tidal constituents at these depths. There was no significant spectral peak at the inertial frequency (ω=0.83 cpd) (here not shown). The narrow width of the canyon likely suppresses inertial waves [101, 127].
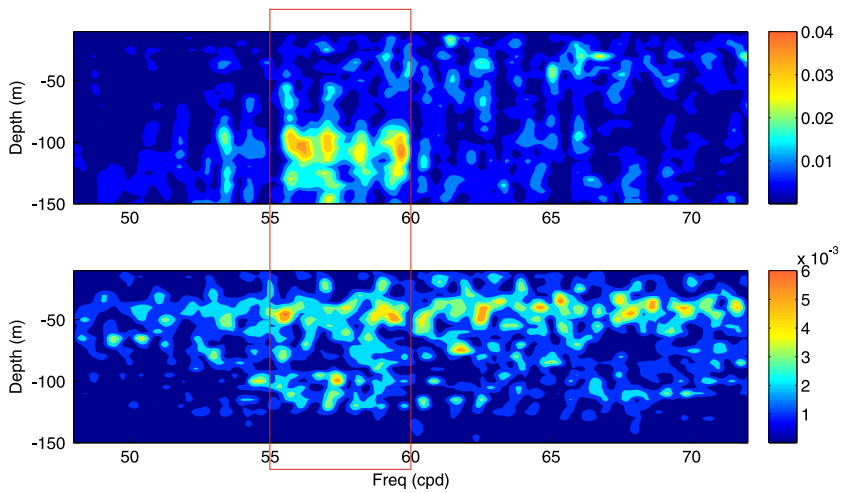
Figure 5.3: *Panel a: Spectra of vertical current component (cm^2s^{-2}/cpd) with depth. Panel b: The same as panel (a) for echo anomaly (db^2/cpd). Red rectangle indicates the most energetic frequency band.*

The rotary spectra showed that, as expected for free linear internal waves in the Northern Hemisphere, motions are clockwise polarized (cyclonic component) at the frequency of the IW (Figure 5.4). However, it can see that there is a small difference between cw and ccw motions. This departure suggests the importance of the nonlinearity, external forcing, and boundary effects in the Jolúcar submarine canyon.
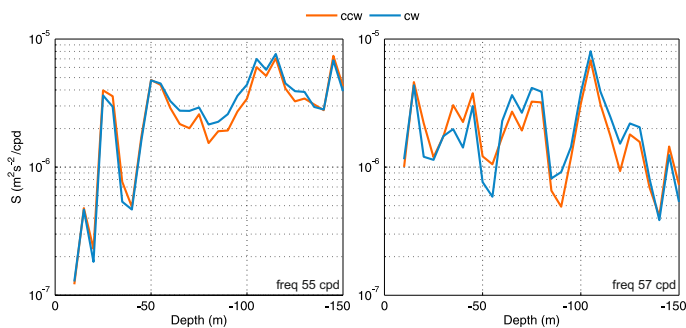
Figure 5.4: *Rotary spectrum of currents velocity with depth at 55 (left panel) and 57 (rigth cpd) frequencies. The blue and orange curves correspond to clockwise and counterclockwise motions, respectively.*

The power Hovmöller of the EA at a frequency of 56 cpd showed largest amplitude at this frequency occurring at 50-100 m depths for both the EA and the vertical gradient of EA (Figure 5.5a-f). For the EA the wavelet amplitude reached depths up to 120 m (Figure 5.5a). However, most energy was found at 50 and 100 m depth (Figure 5.5b). The wavelet of the vertical gradient of the EA also showed highest amplitudes at about 50 and 100 m depth (Figure 5.5e). Highest amplitudes for both the EA and the vertical gradient of EA are observed at infrequent time intervals (Figure 5.5c,f). Thus, the regions with most prevalent periods of high-frequency influence found in the wavelet of the EA and the vertical gradient of the EA were between days 14 and 15, 15 and 16, 16 and 17, and 17 and 18. Therefore, high-frequency IWs are observed, but only during daytime when zooplankton was concentrated at depth levels just below. These results might suggest that zooplankton may be using the IWs as feeding grounds and, perhaps, predator-risky free ride.
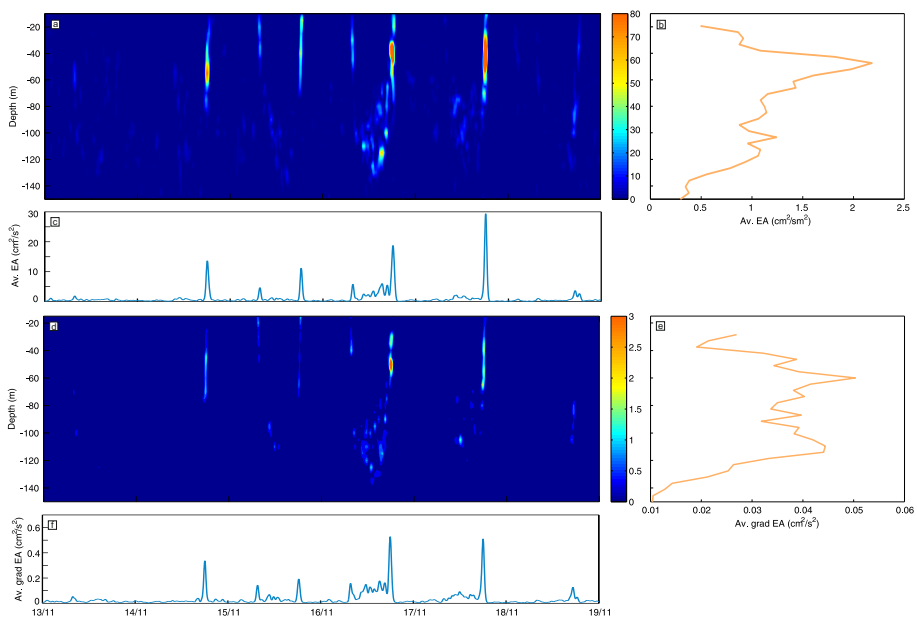
Figure 5.5: *Power Hovmöller diagrams showing the signal at 56 cpd obtained from wavelet anlaysis of echo anomaly (db^2s^{-2}) (panel a), where panels (b) and (c) are the depth and time average of panel (a), respectively. Panels d-f are the same as panel (a) for the vertical gradient of echo anomaly ($db^2s^{-2}m^{-2}$).*

5.4.2 Vorticity

Figure 5.6 shows both speed and direction wind during the field study. The values reported are for where the wind is coming from (meteorological

convection). Northwesterly were predominant the day before the field survey (Figure 5.6, June 7th). Easterly and northerly wind also blew during the time period studied (Figure 5.6, shaded area). Wind velocity during the cruise indicated a period of calm conditions.
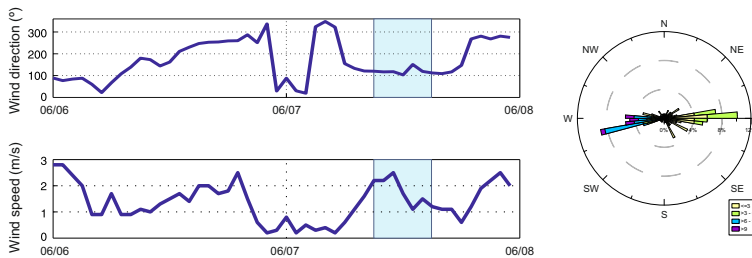
Figure 5.6: Speed components and direction wind time series, and wind rose at 10 m above sea level. Data obtained from the nearest hindcasting points of the model SIMAR (provided by Puertos del Estado (Ministerio de Fomento, Spain)). Shaded area displays the field survey period.

Figure 5.7 shows vertical profiles of density, temperature and salinity measured from a CTD in the Jolúcar canyon on June 13,2010. These profiles provide a good indication of the depth of the pycnocline during the field survey. Thus, density increases suddenly at 30 m depth, which indicates the depth of the pycnocline. Moreover, density also increases suddenly at 10 m depth.
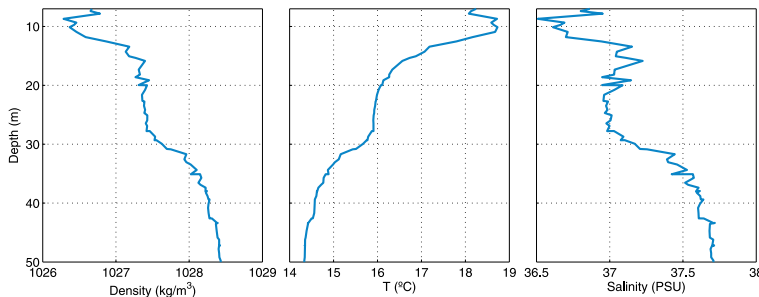
Figure 5.7: Vertical profiles of relative density (kg/m³) (panel a), temperature (° C) (panel b), and salinity (psu) (panel c) measured from a CTD in the Jolúcar canyon.

Contour plots of ADCP data throughout the sampling circuit show the exchange flow characteristics observed during the cruise (Figure 5.8). Here it is presented only the first (Figure 5.8 a-b) and tenth circuits (Figure 5.8 c-d). Results show that surface flow is in opposite direction to bottom flow. The vertical structure of horizontal flow, however, changes throughout the field survey. Two distinct layers are shown at the beginning. Although the flow is still vertically sheared in the tenth circuit, it is essentially in one direction, in contrast to

the first circuit. Up-canyon flow appears only at the beginning of sampling, with velocities < 10 cm/s. For the most part the flow is southeastward, or down-canyon.
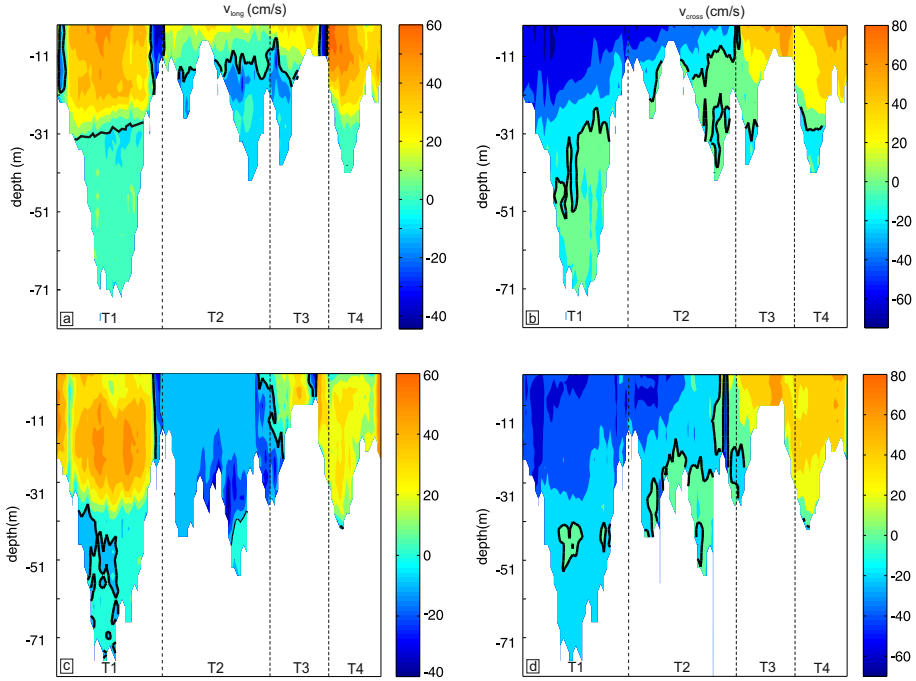
Figure 5.8: *Vertical sections of both longitudinal (v_{long}) and cross (v_{cross}) velocity components (in cm/s) of the first (panels a-b) and the tenth (panels c-d) cycles of the field survey. Transects T1-T4 were measured counter-clockwise around a four cornered circuit starting at the beginning of T1. Positive longitudinal and cross velocities indicate eastward and northward directions, respectively.*

Horizontal velocity fields associated with different depths are shown in Figures 5.9 and 5.10 for the first and tenth cycles, respectively. During the first cycle, the current's path is different at 20 m (Figure 5.9 b) than at the surface (Figure 5.9 a), and a cyclonic tendency is observed near the canyon rim. At 30 m and below (Figure 5.9 c, d) a different flow pattern is observed and velocity vectors are in opposite direction than in surface. During the tenth cycle, the cyclonic eddy is observed at about 30 m depth (Figure 5.10).
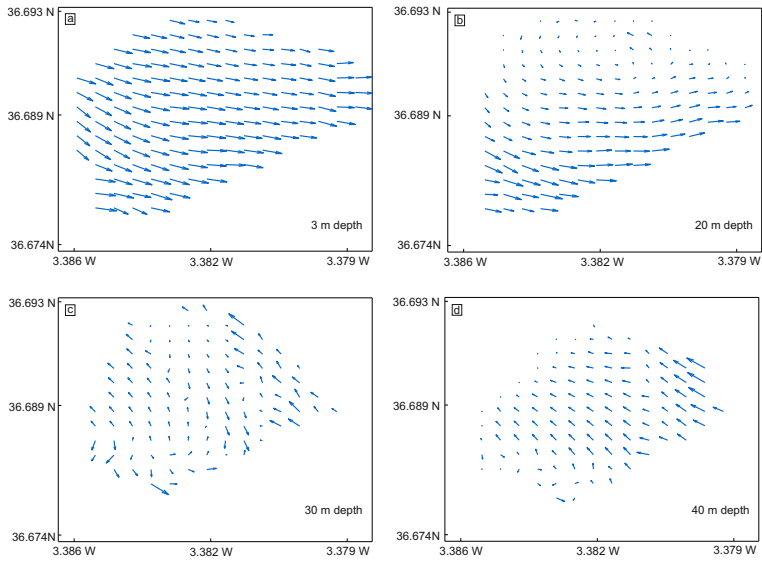
Figure 5.9: *Horizontal velocity vectors at 3 m (panel a), 20 m (panel b), 30 m (panel c), and 40 m (panel d) depths corresponding to the first cycle of the field survey. Units are cm/s.*
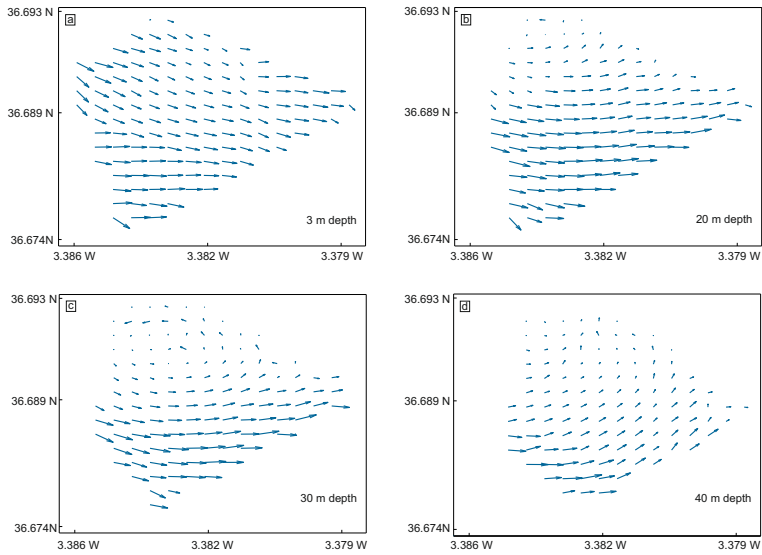
Figure 5.10: *Horizontal velocity vectors at 3 m (panel a), 20 m (panel b), 30 m (panel c), and 40 m (panel d) depths corresponding to the tenth cycle of the field survey. Units are cm/s.*

The vorticity field in vertical sections of transect T1 during the field survey is shown in Figure 5.12. A positive vorticity is displayed at about 20-40 m depth, which evolves over the time. This behaviour of the vorticity is closely related to the position of the pycnocline. The distribution of the echo anomaly also suggests the presence of a pycnocline around a depth of 30 m (Figure 5.13). The evolution of the pycnocline shows the oscillations of the internal waves that travel on the pycnocline.
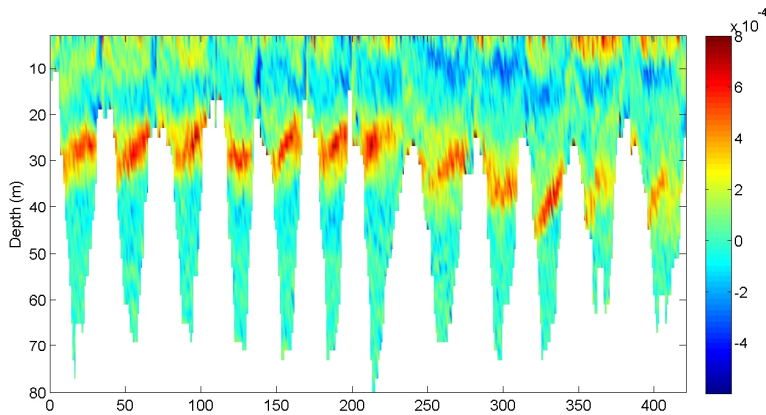
Figure 5.11: *Hovmöller diagram of vorticity corresponding to the T1 transect during the field survey period wiht depth. The 2-13 cycles are represented.*
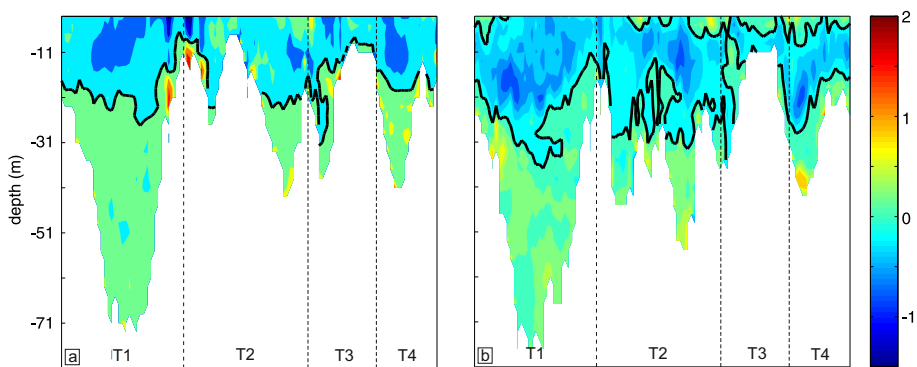
Figure 5.12: *Vertical sections of echo anomaly (dB) of the first (panel a) and the tenth (panel b) cycles of the field survey. Transects T1-T4 were measured counter-clockwise around a four cornered circuit starting at the beginning of T1.*

The vertical component of the vorticity at 30 m depth is shown in Figure 5.13. The vorticity field at about 30 m depth shows a cyclonic vorticity path,

with positive values of vorticity. Current speeds, streamlines (Figure 5.13, black lines), the area of positive vorticity (Figure 5.13, red contours), and the vortex of the cyclonic eddies (Figure 5.13 green cross) at about 30 m depth are shown in Figure 5.13 for different cycles during the field survey. A positive vorticity field (Figure 5.13 red contours) at about 30 m depth is displayed, showing a cyclonic circulation during the field survey. Streamlines also indicate the existence of the cyclonic eddy. This figure shows how the vortex translates over time. The area of the cyclonic eddy is about 1.4, 1.32, 0.98, and 1.31 km^2, and its circulation is about 0.0003, 0.0002, 0.00018, and 0.0002 m^2/s for the 10-13 cycles of the field survey, respectively. The existence of a cyclonic circulation is consistent with the circulation described in section 3.2 for a narrow canyon. Moreover, the cyclonic vorticity evolves over time, which is different for each circuit sampled. This results are consistent with Figures 5.11 and 5.12.
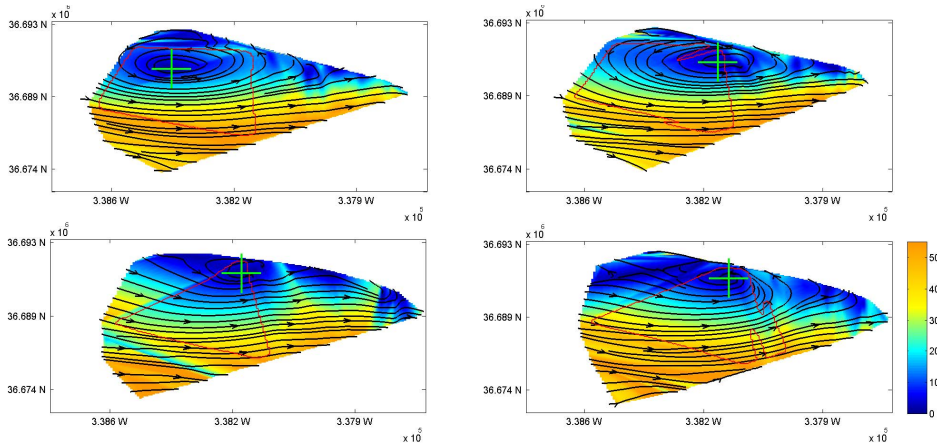
Figure 5.13: *Horizontal speed (cm/s) at 30 m depth during the tenth-thirteen cycles of the field survey. Streamlines are showed (black vectors). Area of positive vorticity is marked with a red contour, and the center of the cyclonic eddy is indicated with a green cross.*

Figure 5.14 displays the Hovmöller diagram of the vertical component of the vorticity corresponding to a middle section of the field survey area (Figure 5.14 b) at 30 m depth with time. Again, a positive vorticity is shown at 30 m depth, which varies little in time. In contrast, the intensity of positive vorticity varies with time. This variation of the intensity in the positive vorticity could indicate that internal waves oscillating along the pycnocline generate the cyclonic circulation in the canyon.
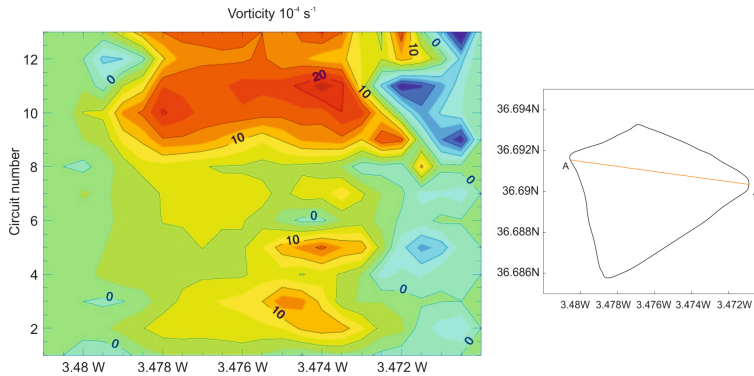
Figure 5.14: *Left panel: Hovmöller diagram of the vertical vorticity component corresponding to the section A-A' at 30 m depth during the field survey. Right panel shows the section A-A' chosen to display the Hovmöller diagram of vertical vorticity.*

5.5 Discussion

The objective of this chapter is to analyze the behaviour of currents, and to determine internal waves and vorticity in the Jolúcar submarine canyon by means of observations.

The echo intensity and the echo anomaly signals displayed the first indication of internal waves IWs propagating in the Jolúcar submarine canyon. Spectra of vertical current component and the echo anomaly data showed high variance at frequencies of 55-60 cpd at 50 and 100 m depths, approximately. At these depths, phase changes were observed for the main harmonic constituents (as shown in Chapter 4 of this Thesis). Therefore, these results suggested internal tides amplified in the pycnocline. Moreover, wavelet analysis showed that IWs were only visible during the daytime when zooplankton was concentrated at deepness. These observations suggested the existence of a relationship between physical water motions by IWs and zooplankton behaviour. Zooplankton might use the environmental variability of high-frequency IWs to feeding when the risk to be predated is higher. This relationship has been observed in other areas of the Alborán Sea [128]. Each analysis performed on the echo anomaly provided evidence of the presence of high-frequency internal waves located around the pycnocline of the Jolúcar canyon.

The vertical structure of horizontal currents suggests that two distinct layers exist over the canyon . The surface flow direction and the wind direction during the day before the cruise might suggest that canyon circulation respond to wind forcing with a time lag. Wind forcing was rather weak (<5 m/s). Pressure data in the study site, plus longer wind and currents time series are required to test this

assumption using correlation functions and a more complete dynamic analysis than that addressable here. The differences between the Echo anomaly signal at the beginning and the end of the cruise could be due to the zooplankton distribution. By increasing the light, zooplankton is concentrated at greater depths [128].

In general, near the surface the flow is only weakly affected by the canyon. At about 30 m depth, the flow reverses over the canyon rim with the development of a cyclonic gyre. This cyclonic circulation is consistent with the theoretical circulation of a narrow canyon described in section 3.2 and described by [103]. The vorticity that develops at and underneath the canyon rim could be due to both flow separation and vortex stretching mechanisms [108]. On one hand, vorticity could occur because of incident flow travelling along the slope, which is affected by friction against the slope and as a result, has a strong shear. Once past the canyon rim, part of the flow detaches from the slope and part of the flow follows the canyon [104]. Flow separation may ensue if the canyon is moderately or highly stratified. On the other hand, vorticity could also occur because of the stretching of water flowing from the adjacent shelf. Owing to conservation of potential vorticity these fluid columns turn cyclonically when entering the canyon. A positive vorticity is found at the same depth than pycnocline during the field survey, whose intensity varies in time. It suggests that the generation mechanism of the cyclonic circulation in the canyon could be the flow separation. Thus, pycnocline can oscillate as an internal wave propagating at 30 m depth and, when it enters into the canyon, generates a recirculation at this depth. A detailed and broad field study will be necessary to explore this aspect. In previous studies in other narrow submarine canyons around the world, cyclonic circulation has been reported. Allen et al [29] used a numerical model and revealed that, near the canyon rim, the vortex stretching generated over Barkley canyon was strong enough to produce a closed cyclonic eddy. Flexas et al [124], by using observational data, observed a cyclonic vorticity in Blanes canyon. Submarine canyon circulation simulated in general numerical and laboratory models [98, 129] are also in good agreement with the results present here. On the other hand, for the most part of field survey the flow is down-canyon. This result is consistent with those obtained in chapter 4 of this Thesis. This behaviour suggests that the canyon might act as an scape pathway.

Observations show that, in order to interpret the motions within the canyon in terms of theory, it is necessary to acquire flow and density field information from continental shelf and slope locations upstream of the canyon.

5.6 Conclusions

This Chapter analyzed both internal waves and vorticity in the Jolúcar submarine canyon. The following conclusions can be derived from this research:

1. High-frequency internal waves are identified in the Jolúcar canyon by means of observations. This kind of waves were found at 60 and 100 m depth, only during the daytime, and were not observed every day.

2. The power Howmöller diagrams of the echo anomaly and the vertical gradient of the echo anomaly signals were in good agreement, showing oscillations corresponding to a period of about 25 minutes at the same depths and times.

3. Results from observations suggest the existence of a relationship between physical water motions by internal waves and zooplankton behaviour.

4. A study of the flow has been conducted in Jolúcar submarine canyon using data from an oceanographic cruise. The study indicates that cyclonic flow (positive vorticity) appears in the vicinity of the canyon rim. Observations from this study are in good agreement with the theoretical circulation in a narrow submarine canyon.

5. Positive vorticity values are stronger at the pycnocline depth than in the rest of the water column. This behaviour might suggest that the pycnocline oscillates as an internal wave and, when it encounters the canyon, it generates a recirculation at this depth.

6. Although two distinct layers are observed in the canyon water column, which indicate both down and upcanyon flows, the net direction of the canyon flow is downcanyon. Net down-canyon flow suggests that the canyon might act as an escape pathway, at least during the period of observation, to any type of substances.

Part III

CONCLUSIONS AND FUTURE RESEARCH

6

Conclusions and future research

6.1   Conclusions

The aim of this Thesis was to study hydrodynamic processes in both continental shelves of Alborán Sea (regional scale) and a submarine canyon (local scale). To achieve this goal, a combination of observational data analyses and theoretical work has been performed.

The main conclusions are organised according to the research questions defined in section 1.2:

- Research question 1: *Are there free long-period waves propagating along the continental shelf of the Alborán Sea?*
  The existence of Continental Shelf Waves on the continental shelves of the Alborán Sea was verified using a statistical approach from observational data and a theoretical work. Cross correlation analyses and cross spectra calculations have confirmed the presence of a westward-travelling signal on the North Continental Shelf and an eastward-travelling signal on the South Continental Shelf of the Alborán Sea.

The cross spectra between residual sea level signals along Alborán Sea have showed significant coherence at long periods. Phase speeds of free Continental Shelf Waves were calculated from significant periods. There was evidence of a seasonal variation in the phase speed of the waves, which may be related to variations in the speeds of currents in the Alborán Sea.

The behaviour of free Continental Shelf Waves propagating over the continental shelf of the Alborán Sea was analysed using linear geostrophic shallow water equations .

- Research question 2: *How does the continental shelf of Alborán Sea respond to different external forcings?*

  The main theoretical characteristics and properties of forced Continental Shelf Waves were studied using an analytical model. The linear shallow water equations, considering some assumptions, such as an inviscid, barotropic, and coastal ocean on a Northern Hemisphere f-plane, were developed for a continental shelf with a bottom topography similar to Alborán sea. The main results were that bottom friction, alongshore wind stress, and atmospheric pressure gradient control the structure of free Continental Shelf Waves.

- Research questions 3 and 4: *What are the main hydrodynamic processes in the Jolúcar canyon, and what are their associated frequencies?*

  This Thesis attempts to identify the main forcings that induce the circulation in a submarine canyon of the Alborán Sea by means of observations, and with an analytical model that consists of the linearized hydrodynamic equations for non-homogeneous, rotating, viscous flows.

  Overall, the results from observations indicate that only 10 % of the total submarine canyon circulation is driven by tides, while local atmospheric forcing explains 65 % of the circulation variability. Regarding the atmospheric forcing, wind stress forcing explains 35 % of total canyon circulation, and, significantly enough, local atmospheric pressure gradients induce 30 % of the canyon circulation. Moreover, superinertial frequencies of the currents are likely related to small-scale atmospheric forcings (barometric, wind speed, and direction) acting directly over the water surface.

  The analytical solutions proposed in this Thesis reproduce well the spatial structure of currents associated with the wind and the local barometric pressure gradient. These results indicate that the governing equations in

a non-homogeneous water column, which usually only include the wind forcing, required the inclusion of barometric pressure gradients to emulate the observations.

Internal waves with a period of 25 minutes are identify in the Jolúcar submarine canyon. These waves were only observed at 60 and 100 m depth and were only visible during the daytime. These observations suggest the existence of a relationship between physical water motions by internal waves and zooplankton behaviour.

A sampling strategy is presented in this Thesis to further study the circulation and dynamics in submarine canyons. Results show that a positive vorticity, which indicates a cyclonic circulation appears at the pycnocline depth. Although two distinct layers are observed in the canyon water column, which indicate both down/ upcanyon flows, the net direction of the canyon flow is downcanyon. This might suggest that canyon might acts as a seaward pathway, at least during the experiment, to any type of substances.

6.2   Future research

Alborán Sea is considered an important oceanographic transition zone between the Mediterranean Sea and the Atlantic Ocean, resulting in different oceanographic characteristics, and a great diversity of species. It is an area with a great environmental and economic value to Andalusia and Spain. This work has intended to increase the knowledge of local and regional hydrodynamic processes of the Alborán Sea continental shelves. Therefore, this Thesis aims to assist in the development of an integral management of this important area. Three main lines of future research in this area are proposed:

1. The first one should be focused at local scales. A study should determine whether the model applied to Jolúcar canyon in this Thesis can be implemented to other submarine canyons of the Alborán Sea. Thus, questions 3 and 4 proposed in chapter 1 of this Thesis should be applied to other submarine canyons of Alborán Sea. Field studies would be required for this purpose.

2. The second line should be focused at the regional scale. This research line should focus two studies:

   - A first study should aim to research the interaction between submarine canyons and continental shelf dynamics of the Alborán Sea. Therefore, two questions should be addressed: How do submarine canyons in

the Alborán Sea alter the shelf dynamics? and How do the general shelf circulation modify the submarine canyons circulation? Field information should be required on hydrography and flow structures over the continental shelf and submarine canyons.

- Another study of interest should be the study of possible interaction between Continental Shelf Waves with the Alborán Gyres. In order to know if this type of waves are part of Alborán Gyres, simultaneous records of currents and sea level along transverse sections should be required to further explore this aspect.

3. Finally, the third line should focus on the global scale. In order to develop an integral management of the entire Alborán Sea area, an integrated study should be done that analyses the interaction of the circulation of Alborán Sea with both the Mediterranean Sea and the Atlantic Ocean using a numerical model.

A

Analysis techniques

This appendix describes a detailed description of the analysis procedures used in this Thesis.

1. **Standard harmonic analysis.**
   In order to extract the tidal signal form the observations, the tidal analysis package T $_{Tide}$ [63] was applied. Thus, the currents and sea level time series were fitted to different numbers of harmonics by the least-squares method [126]

$$(u, v, \eta) = (u_0, v_0, a_0) + \sum_{j=1}^{n} (u_{Aj}, v_{Aj}, \eta_{Aj}) cos(\omega_j t + (\tau_{uj}, \tau_{vj}, \tau_{\eta j}) \quad \text{(A.1)}$$

where t is the time; u_0, v_0, and a_0 are the average value of u, v, η, respectively; $u_{Aj}, v_{Aj}, \eta_{Aj}$ are the amplitudes of the harmonic j of frequency ω; and τ is the phase angle. Up to n harmonics may be fitted to the data.

2. **Spectral Transfer Function.**

The frequency-dependent transfer function, TF, estimates the linear casual relationship between any pair of variables at a given frequency. The gain (or admittance amplitude) function TF behaves like a spectral regression coefficient at each frequency. Given an input and output time series x(t), wind stress, and y(t), sea level, and their Fourier transforms, the TF between them can be obtained as [130]

$$TF(\omega) = \frac{S_{xy}(\omega)}{S_x(\omega)} \tag{A.2}$$

where $S_{xy}(\omega)$ is the cross power spectral density, and $S_x(\omega)$ is the power spectral density of the input time series.

3. **Cross correlation analysis.**

Cross correlation, CC, is a standard method of estimating the degree to which two series x and y are correlated in the time domain. The CC analysis is basically a generalization of standard linear correlation analysis [131]. It can be expressed as

$$CC_{x,y}(lag) = \frac{1}{N} + \sum_{j=1}^{N-lag} (x_j, \bar{x}_j)(y_j, \bar{y}_j) \tag{A.3}$$

for lag=0,1,...(N-1); where N is the series length, $(\bar{x})$ and $\bar{y}$ are the sample means. The sample CC function is the cross-variance function scaled by the variances of the two time series:

$$r_{x,y}(lag) = \frac{CC_{xy}(lag)}{\sqrt{CCxx(0)CCyy(0)}} \tag{A.4}$$

where $C_{xx}(0)$ and $C_{yy}(0)$ are the sample variances of x and y.

4. **Coherence squared.**

Squared spectral coherence, Φ^2, estimates the degree of linear association between the phases and amplitudes of two data records as a function of the frequency. It is defined as [132]

$$|\Phi(\omega)|^2 = \frac{|S_{xy}(\omega)|^2}{|S_x(\omega)||S_y(\omega)|} \tag{A.5}$$

where $|S_{xy}(\omega)|^2$ is the square of the absolute value of the cross spectrum, and $|S_x(\omega)|$ and $|S_y(\omega)|$ are the autospectral densities of the time series x and y, respectively.

The 95 % statistical significance level for the squared coherence is determined following [133] as

$$CL^2_{1-0.95} = 1 - 0.95^{2/(EDOF-2)} \tag{A.6}$$

where EDOF are the equivalent degrees of freedom. The EDOF for a Hanning window are calculated from EDOF= (8/3)(N/M), where N is the length of the time series, and M the half-width of the window in the time domain.

5. **Spectral analysis.**

The power spectrum of a signal shows how a signal's power is distributed through the frequency domain. The discrete Fourier Transform is defined by the equation

$$X(\omega) = \sum_{j=0}^{N-1} x(j)e^{2\pi ij\omega/N} \tag{A.7}$$

If a N-point sample of a time series x(t) is taken and the Fast Fourier Transform (FFT) is used to compute its discrete Fourier transform, then the power spectrum, using a periodogram, is defined at N/2+1 frequencies as

$$P(\omega) = \frac{1}{N^2} \left|X_{N/2}\right|^2 \tag{A.8}$$

Welch's method splits the data into overlapping segments, computes modified periodograms of the overlapping segments, and averages the resulting periodograms to produce the power spectral density estimate. The power spectral density is also smoothed with a Hanning window.

6. **Empirical Orthogonal Functions.**
   Using this method, the most efficient decomposition of the data into representative modes is determined by empirically finding the eigenfunctions that best describe the information. It can be proven that the EOF method describes the data in the most compact form in a sense to be described below. The EOF eigenmodes can be ordered in terms of the percentage of the total variance to be described by each mode and, in addition, the modes are statistically uncorrelated with one another. Additionally, each mode contains phenomena with differing spatial/temporal scales and thus can be isolated. It is supposed that a gridded data set composed of a space-time field X(t,x) represents the value of the field X at time and spatial position x. The observed field is then represented by a data matrix [134]. The covariance matrix is then defined by

$$\Sigma = \frac{1}{n-1} X'^T X' \tag{A.9}$$

which contains the covariance between any type par of grid points. The aim of EOF is to find the linear combination of all the variables. That is to find a direction $a=(a_1, ... \; a_p)^T$ such that $X'a$ has a maximum variance. Now, the variance of time series $X'a$ is calculated. To make the problem bounded the vector a is required to be unitary.

$$max_a(a^T \sum a), s.ta^T a = 1 \tag{A.10}$$

which solution is a simple eigenvalue problem:

$$\sum a = \lambda a \tag{A.11}$$

where λ are the eigenvalues.
the k'th EOF is simply the k'th eigenvector a_k of Σ after the eigenvalues, and the corresponding eigenvectors, have been sorted in decreasing order. The projection of the anomaly field X' onto the k'th EOF a_k, i.e., $c_k=X'a_k$ is the k'th principal component

$$c_k(t) = \sum_{n=1}^{p} x'(t, x) a_k(x) \tag{A.12}$$

7. **Wavelet analysis.**

The wavelet transform is a useful tool for extracting both time and frequency information from a time series. Continuous wavelet transform, using a mother wavelet function (the Morlet wavelet) and adopting the methods described by Torrence and Compo [110] is used. Assume that a time series, x_n is given, with equal time spacing $\triangle t$ and n=0, ..., N-1, the Morlet wavelet is given by

$$\chi(t_0) = \pi^{1/4} e^{i\omega_0 t_0} e^{-t_0^2/2} \tag{A.13}$$

where ω_0 denotes the dimensionless frequency of the Morlet wavelet, and t_0 is a nondimensional 'time' parameter. The term 'wavelet function' is used generically to refer to either orthogonal or nonorthogonal wavelets. The continuous wavelet transform of a discrete sequence x_n is defined as the convolution of x_n with a scaled and translated version of $\chi(t_0)$:

$$W_n(s) = \sum_{n'=0}^{N-1} \chi * \left[\frac{(n'-n)\triangle t}{s} \right] \tag{A.14}$$

where (*) indicates the complex conjugate. By varying the wavelet scale s and translating along the localized time index n, one can construct a picture showing both the amplitude of any features versus the scale and how this amplitudes varies with time [110].

The Cross Wavelet Transform (XWT). Given two time series $x(t)$ and $y(t)$ with wavelet transforms $W_n^x(s)$ and $W_n^y(s)$, the XWT is defined as

$$W_n^{xy}(s) = W_n^x(s) W_n^{y*}(s) \tag{A.15}$$

where $W_n^{y*}(s)$ is the complex conjugate of $W_n^y(s)$. The cross wavelet spectrum is complex, and hence the cross wavelet spectrum can be defined as $|W_n^{xy}(s)|$ [110].

8. **Rotary spectrum.**

Rotary spectrum analysis is a proven technique separate vector time series into clockwise and counter-clockwise rotating circular components. Basically, the method hinges on the fact that the spectral decomposition gives at each frequency a sinusoidal wave for each horizontal velocity component [123]. The components of the rotary spectrum as calculated following Gonella [123]. Given horizontal velocity components, u, v, the complex current, w, is calculated as

$$u(t) = \sum_n [a_n cos(\omega_n t) + b_n sin(\omega_n t)] \tag{A.16}$$

$$v(t) = \sum_n [c_n cos(\omega_n t) + d_n sin(\omega_n t)] \tag{A.17}$$

$$w(t) = u + iv = (a + ic)cos(\omega t) + (b + id)sin(\omega t) =$$
$$= A^+((cos(\omega t) + isin(\omega t) + A^-(cos(\omega t) - isin(\omega t) \tag{A.18}$$

Magnitudes of the rotary components are:

$$|A^+| = \frac{1}{2} \left[(a + d)^2 + (c - d)^2 \right]^{1/2} \tag{A.19}$$

$$|A^-| = \frac{1}{2} \left[(a - d)^2 + (c - d)^2 \right]^{1/2} \tag{A.20}$$

and the components of the rotary spectrum are:

$$|S^+| = \frac{(A^+)^2}{N \triangle t} \tag{A.21}$$

$$|S^+| = \frac{(A^-)^2}{N \triangle t} \tag{A.22}$$

B

Governing equations

This appendix describes the entire procedure of the analytical model derived in chapter 4.

- **Theoretical analysis of Continental Shelf Waves.**
    1. To calculate the structure and dispersion relationship of a CSW, only large-scales, subinertial and non-divergent motions were considered. In order to apply these considerations, $\omega/f \sim kL \sim r/fH \ll 1$. Non-dimensionalization of governing hydrostatic equations of motion and continuity is performed in order to ensure that these considerations can be applied in the theoretical study of this Thesis. Considering the expressions

$$\frac{\partial}{\partial t} \sim \omega$$

$$\frac{\partial}{\partial x} \sim \frac{1}{L}$$

$$\frac{\partial}{\partial y} \sim k$$

$$\frac{\partial h}{\partial x} \sim \frac{dh}{dx} \sim\sim \frac{h_s}{L}$$

$$u, v \sim U$$

(B.1)

From vorticity

$$\frac{\partial u}{\partial y} \sim \frac{\partial v}{\partial x}$$

$$kU \qquad \frac{U}{L}$$

$$u = kLU$$

$$v = U$$

(B.2)

and then,

$$\eta = \frac{\partial u}{\partial y} - \frac{\partial v}{\partial x}$$

$$\frac{U}{L} \qquad kkUL$$

$$\eta \sim \frac{\partial v}{\partial x}$$

(B.3)

Dimensionless form of transverse equation of motion is

$$\frac{\partial u}{\partial t} - fv = -g\frac{\partial \eta}{\partial x} - \frac{ru}{H}$$

$$\omega kLU \quad fU \quad \frac{fUL}{L} \quad \frac{rkLU}{H}$$

$$(\frac{\omega}{f})(kL) \quad 1 \quad 1 \quad (\frac{r}{fH})(kL)$$

$$\ll 1 \qquad\qquad\qquad \ll 1 \qquad\qquad (B.4)$$

Thus, $\omega/f \sim kL \sim r/fH \ll 1$, and then

$$\frac{\partial u}{\partial t} \ll fv$$

$$\frac{\partial u}{\partial t} \ll g\frac{\partial \eta}{\partial x}$$

$$\frac{ru}{H} \ll fv$$

$$\frac{ru}{H} \ll g\frac{\partial \eta}{\partial x} \qquad\qquad (B.5)$$

and the terms $\partial u/\partial t$, and ru/H can be negligible in the cross-shelf momentum equation, and then, only large- scale, subinertial motions are considered.

Dimensionless form of equation of continuity is

$$H\left(\frac{\partial u}{\partial x} + \frac{\partial v}{\partial y}\right) = \frac{\partial \eta}{\partial t}$$

$$h_s KU \quad h_s KU \quad \frac{\omega fUL}{g}$$

$$1 \qquad\quad 1 \qquad \frac{\omega fL}{h_s kg} \qquad\qquad (B.6)$$

where

$$\frac{\omega fL}{h_s kg} = \frac{\frac{\omega}{f}f^2L^2}{h_s kLg} \sim \left(\frac{\frac{\omega}{f}}{kL}\right)\left(\frac{f^2L^2}{gh_s}\right) \qquad\qquad (B.7)$$

Thus,

$$\frac{\partial \eta}{\partial t} \ll \frac{\partial (uh)}{\partial x}$$
$$\frac{\partial u}{\partial t} \ll \frac{\partial (vh)}{\partial y}$$

$$\text{(B.8)}$$

and the term $\partial \eta / \partial t$ can be negligible of the continuity of mass equation, i.e., the motion is horizontally nondivergent.

2. The coastal boundary condition under wind forcing, and the offshore boundary condition under pressure gradients forcings, are:
The coastal boundary condition under wind forcing is

$$\frac{d\eta}{dX} = \frac{\tau f L}{rgL}$$
$$\frac{d\eta}{d\zeta} = \frac{\tau H}{rgL} (ie)^{1/2}$$

$$\text{(B.9)}$$

where $e = f/f\gamma L$
The offshore boundary condition under pressure gradient forcing is

$$\eta(L) = \frac{P_0}{iL}$$

$$\text{(B.10)}$$

where $P = P_0(i(ly - \omega t))$; and P_0 is a constant.

3. Expressions of velocity components, u and v, obtained from equations (2.1)-(2.2), and the η solution, are

$$v = -\frac{g}{f}\frac{\partial \eta}{\partial x}$$
$$u = -\frac{g}{f}\frac{\partial \eta}{\partial y} + \frac{rg}{f^2 H}\frac{\partial \eta}{\partial x} - \frac{g}{f^2}\frac{\partial^2 \eta}{\partial x \partial t} + \frac{F}{gH}$$

$$\text{(B.11)}$$

- **Circulation driven by wind stress and pressure gradient.**

The classical analytical solution of wind-induced current profile [111] was extended here by considering the superposition of bottom and surface Ekman layers, and including the influence of barotropic pressure gradients in a non-homogeneous water column. To derive an analytical solution, we assume the vertical eddy viscosity temporally and vertically constant and independent of the flow, and a flat bottom. Considering linear and stationary motion, and for simplicity's sake, the momentum equations on the f-plane can be written as:

$$-f\hat{v} = -\frac{1}{\rho}\frac{\partial P}{\partial x} + \frac{\partial}{\partial z}\left(A_v \frac{\partial \hat{u}}{\partial z}\right) \tag{B.12}$$

$$+f\hat{u} = -\frac{1}{\rho}\frac{\partial P}{\partial y} + \frac{\partial}{\partial z}\left(A_v \frac{\partial \hat{v}}{\partial z}\right) \tag{B.13}$$

where coordinates x, y are positive to South and East, respectively, and z is negative downward, with $z = 0$ at the surface; the horizontal components of the current $\hat{u}$ and $\hat{v}$ are functions of z; ρ is the water density; P is the pressure; and A_v is the vertical eddy viscosity coefficient. It was also assumed that ρ is a weak function of depth $\rho(z) = \rho_0 \exp(-z/z_0)$, where ρ_0 is $1027\ \mathrm{kg\,m^{-3}}$, and $z_0 = 10^4$ m.

Combining equation 4.1 and B.2 in favour of $\hat{u}$, the following governing equation is obtained:

$$\frac{d^4 u}{dz^4} + \frac{f^2}{A_v}u = -\frac{f}{A_v \rho}\frac{\partial P}{\partial y} + \frac{1}{A_z}\frac{\partial^2}{\partial z^2}\left(\frac{1}{\rho}\frac{\partial P}{\partial x}\right) \tag{B.14}$$

Equation B.14 is a fourth order linear non-homogeneous differential equation for u assuming that the pressure gradient $(\partial P/\partial x, \partial P/\partial y)$ is prescribed. The procedure to solve it is showed here.

1. First, the homogeneous part $(u_H(z))$ of equation is solved.

$$\frac{d^4 u}{dz^4} + \frac{f^2}{A_v}u = 0 \tag{B.15}$$

$$\lambda^4 + \frac{f^2}{A_v} = 0 \tag{B.16}$$

Equation B.16 is a fourth order equation, which solution is

$$\lambda = \left(-\frac{f^2}{A_v^2}\right)^{1/4} \tag{B.17}$$

and then,

$$\lambda_1 = \sqrt{\frac{f}{A_v}} \left(cos\left(\frac{\pi}{4}\right) + isin\left(\frac{\pi}{4}\right)\right) = \sqrt{\frac{f}{2A_v}} (1+i) \quad \text{(B.18)}$$

$$\lambda_2 = \sqrt{\frac{f}{A_v}} \left(cos\left(\frac{3\pi}{4}\right) + isin\left(\frac{3\pi}{4}\right)\right) = \sqrt{\frac{f}{2A_v}} (-1+i) \quad \text{(B.19)}$$

$$\lambda_3 = \sqrt{\frac{f}{A_v}} \left(cos\left(\frac{5\pi}{4}\right) + isin\left(\frac{5\pi}{4}\right)\right) = \sqrt{\frac{f}{2A_v}} (-1-i) \quad \text{(B.20)}$$

$$\lambda_4 = \sqrt{\frac{f}{A_v}} \left(cos\left(\frac{7\pi}{4}\right) + isin\left(\frac{7\pi}{4}\right)\right) = \sqrt{\frac{f}{2A_v}} (1-i) \quad \text{(B.21)}$$

Expressions B.18-B.10 are the solutions of equation B.16. Thus, scaling z as $D_E/\sqrt{2}\hat{z}$, where $D_E = \sqrt{2A_v/f}$ is the frictional layer depth or Ekman depth, the homogeneous solution $u_H(z)$ of equation B.14 can be expressed as

$$u_H(z) = \tilde{c}_1 e^{\frac{z}{D_E}(1+i)} + \tilde{c}_2 e^{\frac{z}{D_E}(1-i)} + \tilde{c}_3 e^{\frac{z}{D_E}(-1+i)} + \tilde{c}_4 e^{\frac{z}{D_E}(-1-i)} \quad \text{(B.22)}$$

$$u_H(z) = \sum_{n=1}^{4} \tilde{c}_n e^{\beta_n z/D_E} \tag{B.23}$$

Here $\beta_n = cos[(2n+1)\pi/4]$, and $\tilde{c}_n$ are constants to be determined applying the four boundary conditions, and $n=0,1,...$ Thus, the homogeneous solution is related to wind forcing (consistent with Ekman dynamics).

2. The particular solution $u_P(z)$ is associated to the pressure gradient, and its solution is obtained applying the methods of undetermined

coefficients. By comparing the terms of $u_P(z)$ it can see that $\frac{1}{A_z}\frac{\partial^2}{\partial z^2}\left(\frac{1}{\rho}\frac{\partial P}{\partial x}\right)$ is negligible compared to $-\frac{f}{A_v\rho}\frac{\partial P}{\partial y}$

$$\frac{\frac{1}{A_z}\frac{\partial^2}{\partial z^2}\left(\frac{1}{\rho}\frac{\partial P}{\partial x}\right)}{\frac{f}{A_v\rho}\frac{\partial P}{\partial y}} \sim \frac{\frac{1}{z_0^2}}{\frac{f}{A_v}} \sim |\frac{A_v}{fz_0^2}| \sim \frac{10^{-2}m^2s^{-1}}{10^8m^210^{-5}s^{-1}} \ll 1 \qquad (B.24)$$

Therefore,

$$\frac{d^4u}{dz^4} + \frac{f^2}{A_v}u = -\frac{f}{A_v\rho}\frac{\partial P}{\partial y} \qquad (B.25)$$

The particular solution has the general form $u_P(z)=Be^{z/z_0}$, where B is an unknown coefficient. It is an exponential function, which does not change form after differentiation. The expresion of B is found by deriving four times $u_P(z)$ and substituting it back into the equation B.25

$$\frac{d^4u}{d\hat{z}^4} + \frac{f^2}{A_v}u = \frac{1}{f\rho_0}\frac{\partial P}{\partial y}e^{z/z_0} \qquad (B.26)$$

$$\frac{B}{z_0^4}e^{z/z_0} + Be^{z/z_0} = \frac{1}{f\rho_0}\frac{\partial P}{\partial y}e^{z/z_0} \qquad (B.27)$$

$$(1+z_0^4)B = \frac{1}{f\rho_0}\frac{\partial P}{\partial y}z_0^4 \qquad (B.28)$$

$$B \simeq \frac{1}{f\rho_0}\frac{\partial P}{\partial y} \qquad (B.29)$$

Hence,

$$u_p(z) = \frac{1}{f\rho_0}\frac{\partial P}{\partial y}e^{z/z_0} \qquad (B.30)$$

Therefore, the solution of equation B.25 is

$$u(z) = \frac{1}{f\rho_0}\frac{\partial P}{\partial y}e^{z/z_0}\sum_{n=1}^{4}\tilde{c}_n e^{\beta_n z/D_E} \qquad (B.31)$$

The pressure gradient term includes

$$-\frac{1}{\rho}\frac{\partial P}{\partial x} = -\frac{1}{\rho}\left[\underbrace{\frac{\partial P_{atm}}{\partial x}}_{barometric} - \underbrace{\rho(0)g\frac{\partial h}{\partial x}}_{barotropic} + \underbrace{g\int_{-h}^{0}\frac{\partial \rho(z)}{\partial x}dz}_{baroclinic}\right] \qquad \text{(B.32)}$$

and the same for $\partial P/\partial y$.

C

Field surveys

This appendix describes a detailed description of the two field surveys, instruments, and measurements analyzed in this Thesis.

(a) A 250 kHz SonTek Acoustic Doppler Profiler (ADP) was deployed on the bottom, over 175 m of water near the head of the Jolúcar submarine canyon (triangle on Figure 4.1). Data were recorded at 5 m bins from 12 to 17 November 2010 (winter season). Water levels and current velocity profiles were obtained every 60 s. Simultaneous wind speed and direction, and atmospheric pressure data were measured every 10 s with a meteorological station located at the Sacratif Cape, near the head of the canyon (circle on Figure 4.1). Additional atmospheric pressure data were obtained from the European Centre for Medium-Range Weather Forecasts (ECMWF) at $36.4°$ N, $3.25°$, 3 km away from Sacratif Cape (purple square on Figure 4.1), which were used to obtain local atmospheric pressure gradients. Atmospheric pressure data were also obtained from a meteorological station of the Junta de Andalucía (Consejería de Medio Ambiente, Spain)at Adra (Almería). Figure C.1 shows a photograph of the meteorological

station and the ADP current profiler mounted on its structure, prior to deployment in the field. A Coastal Acoustic Release Transponder (CART) was used to recover the ADP.

Figure C.1: Photographys of the instruments used in the first field study. Left panel: structure of the ADP deployed on the bottom of the submarine canyon. Right panel: meteorological station located at the Sacratif Cape.

(b) A 6 hours cruise was carried out on 7 June 2016 in order to obtained the hydrodynamic structure of currents and vorticity parameters. Current velocity measurements were obtained with a towed, downward pointing 300 kHz acoustic Doppler current profiles (ADCP) mounted on a metal bar. ADCP was towed around a closed trajectory consisting of a four-cornered circuit near the main tributary of the submarine canyon (Figure 4.1). The vertical resolution of the data was given by a bin size of 2 m, and data were obtained every 12 s. The sampling interval of the closed circuit was approximately 25 minutes. A total of 13 trajectory repetitions were carried out during the field survey. Profiles of conductivity-temperature were obtained with a SBE-37 CT. Figure C.2 shows a photograph of the ADCP current profiler mounted on its structure, prior to begin the field study.
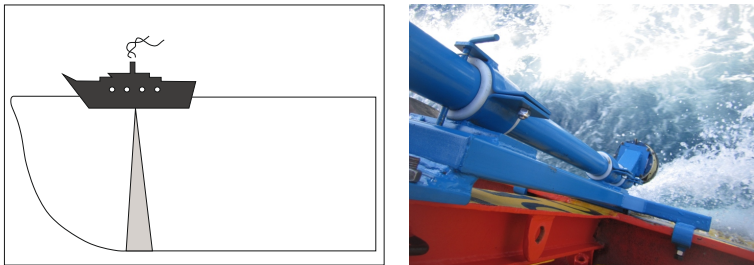
Figure C.2: *Photographys of the ADP used in the secong field study.*

References

[1] FJ Lobo, LM Fernández-Salas, I Moreno, JL Sanz, and A Maldonado. The sea-floor morphology of a Mediterranean shelf fed by small rivers, northern Alboran Sea margin. *Continental shelf research*, 26(20):2607–2628, 2006.

[2] CL Iacono, E Gràcia, S Diez, G Bozzano, X Moreno, J Dañobeitia, and B Alonso. Seafloor characterization and backscatter variability of the Almería Margin (Alborán Sea, SW Mediterranean) based on high-resolution acoustic data. *Marine Geology*, 250(1):1–18, 2008.

[3] MC Comas, JP Platt, JI Soto, and AB Watts. 44. The origin and Tectonic History of the Alborán Basin: Insights from Leg 161 Results. In *Proceedings of the Ocean Drilling Program Scientific Results*, volume 161, pages 555–580, 1999.

[4] L Renault, T Oguz, A Pascual, G Vizoso, and J Tintoré. Surface circulation in the Alborán Sea (western Mediterranean) inferred from remotely sensed data. *Journal of Geophysical Research: Oceans (1978–2012)*, 117(C8), 2012.

[5] J García-Lafuente, JM Vargas, F Plaza, J Candela, and B Baschek. Tide at the eastern section of the Strait of Gibraltar. *Journal of Geophysical Research-Oceans*, 105(C6):14197–14213, 2000.

[6] M Vargas-Yáñez, F Plaza, J García-Lafuente, T Sarhan, JM Vargas, and P Vélez-Belchi. About the seasonal variability of the Alborán Sea circulation. *Journal of Marine Systems*, 35(3):229–248, 2002.

[7] D Macías, M Bruno, F Echevarría, A Vázquez, and CM García. Meteorologically-induced mesoscale variability of the North-western Alborán Sea (southern Spain) and related biological patterns. *Estuarine, Coastal and Shelf Science*, 78(2):250–266, 2008.

[8] A Defant. Physical oceanography; volume 2. 1961.

[9] J García-Lafuente, N Cano, M Vargas, JP Rubín, and A Hernández-Guerra. Evolution of the Alborán Sea hydrographic structures during July 1993. *Deep-Sea Research Part I*, 45(1):39–65, 1998.

[10] P Bárcenas, FJ Lobo, J Macías, LM Fernández-Salas, and V Díaz del Río. Spatial variability of surficial sediments on the northern shelf of the Alboráan sea: the effects of hydrodynamic forcing and supply of sediment by rivers. *Journal of Iberian Geology*, 37(2):195, 2011.

[11] M Ortega-Sánchez, S Bramato, E Quevedo, C Mans, and MA Losada. Atmospheric-hydrodynamic coupling in the nearshore. *Geophysical Research Letters*, 35(23), 2008.

[12] LA Mysak. Recent advances in shelf wave dynamics. *Reviews of Geophysics*, 18(1):211–241, 1980.

[13] KH Brink. Coastal-trapped waves and wind-driven currents over the continental shelf. *Annual Review of Fluid Mechanics*, 23(1):389–412, 1991.

[14] J Kämpf. Lee effects of localized upwelling in a shelf-break canyon. *Continental Shelf Research*, 42:78–88, 2012.

[15] Liping Yin, Fangli Qiao, and Quanan Zheng. Coastal-Trapped Waves in the East China Sea observed by a mooring array in winter 2006. *Journal of Physical Oceanography*, 44(2):576–590, 2014.

[16] SM Pearce. *Coastal Trapped Waves Generated By Hurricane Andrew on the Texas-Louisiana Shelf*. PhD thesis, Texas A&M University, 2011.

[17] JM Huthnance. On trapped waves over a continental shelf. *Journal of fluid mechanics*, 69(04):689–704, 1975.

[18] JS Allen. Coastal trapped waves in a stratified ocean. 1975.

[19] Maurizio Würtz. *Mediterranean submarine canyons: Ecology and governance*. IUCN, 2012.

[20] SE Allen and X Durrieu de Madron. A review of the role of submarine canyons in deep-ocean exchange with the shelf. *Ocean Science*, 5(4):607–620, 2009.

[21] Matthew H Alford and Parker MacCready. Flow and mixing in Juan de Fuca canyon, Washington. *Geophysical Research Letters*, 41(5):1608–1615, 2014.

[22] Thomas P Connolly and Barbara M Hickey. Regional impact of submarine canyons during seasonal upwelling. *Journal of Geophysical Research: Oceans*, 119(2):953–975, 2014.

[23] Allan J Clarke and Stephen Van Gorder. Subinertial canyon resonance. *Geophysical Research Letters*, 43(8):3872–3879, 2016.

[24] V Vlasenko, N Stashchuk, ME Inall, M Porter, and D Aleynik. Focusing of baroclinic tidal energy in a canyon. *Journal of Geophysical Research: Oceans*, 2016.

[25] HJ Freeland and KL Denman. A topographically controlled upwelling center off southern Vancouver Island. *Journal of Marine Research*, 40(4):1069–1093, 1982.

[26] J Kämpf. Transient wind-driven upwelling in a submarine canyon: A process-oriented modeling study. *Journal of Geophysical Research: Oceans*, 111(C11), 2006.

[27] J She and JM Klinck. Flow near submarine canyons driven by constant winds. *Journal of Geophysical Research*, 105(C12):28671–28694, 2000.

[28] BM Hickey. The response of a steep-sided, narrow canyon to time-variable wind forcing. *Journal of Physical Oceanography*, 27(5):697–726, 1997.

[29] SE Allen, C Vindeirinho, RE Thomson, M GG Foreman, and DL Mackas. Physical and biological processes over a submarine canyon during an upwelling event. *Canadian Journal of Fisheries and Aquatic Sciences*, 58(4):671–684, 2001.

[30] R Mirshak and SE Allen. Spin-up and the effects of a submarine canyon: Applications to upwelling in Astoria Canyon. *Journal of Geophysical Research: Oceans*, 110(C2), 2005.

[31] J Tintoré, DP Wang, and PE La Violette. Eddies and thermohaline intrusions of the shelf/slope front off the northeast Spanish coast. *Journal of Geophysical Research: Oceans*, 95(C2):1627–1633, 1990.

[32] M Ortega-Sánchez, FJ Lobo, A López-Ruiz, MA Losada, and LM Fernández-Salas. The influence of shelf-indenting canyons and infralittoral prograding wedges on coastal morphology: The Carchuna system in Southern Spain. *Marine Geology*, 347:107–122, 2014.

[33] C Mans, S Bramato, A Baquerizo, and MA Losada. Surface seiche formation on a shallow reservoir in complex terrain. *Journal of Hydraulic Engineering*, 137(5):517–529, 2011.

[34] E Quevedo, A Baquerizo, MA Losada, and M Ortega-Sánchez. Large-scale coastal features generated by atmospheric pulses and associated edge waves. *Marine Geology*, 247(3):226–236, 2008.

[35] AR Robinson. Continental shelf waves and the response of sea level to weather systems. *Journal of Geophysical Research*, 69(2):367–368, 1964.

[36] LA Mysak. On theory of continental shelf waves. *Journal of Marine Research*, 25(3):205, 1967.

[37] JK Adams and VT Buchwald. The generation of continental shelf waves. *J. Fluid Mech*, 35(4):815–826, 1969.

[38] PH LeBlond and LA Mysak. Waves in the ocean, 602 pp, 1978.

[39] S Thiebaut and R Vennell. Observation of a fast continental shelf wave generated by a storm impacting Newfoundland using wavelet and cross-wavelet analyses. *Journal of Physical Oceanography*, 40(2):417–428, 2010.

[40] EH Schumann and KH Brink. Coastal-trapped waves off the coast of south africa: generation, propagation and current structures. *Journal of Physical Oceanography*, 20(8):1206–1218, 1990.

[41] BM Båth. *Spectral analysis in geophysics*. Elsevier, 2012.

[42] LA Mysak. Topographically trapped waves. *Annual Review of Fluid Mechanics*, 12(1):45–76, 1980.

[43] BV Hamon. The spectrums of mean sea level at Sydney, Coff's Harbour, and Lord Howe Island. *Journal of Geophysical Research*, 67(13):5147–5155, 1962.

[44] BV Hamon and EJ Hannan. Estimating relations between time series. *Journal of Geophysical Research*, 68(21):6033–6041, 1963.

[45] BV Hamon. Continental shelf waves and the effects of atmospheric pressure and wind stress on sea level. *Journal of geophysical research*, 71(12):2883–2893, 1966.

[46] WR Crawford and R E Thomson. Diurnal-period continental shelf waves along Vancouver Island: A comparison of observations with theoretical models. *Journal of Physical Oceanography*, 14(10):1629–1646, 1984.

[47] JH Middleton, TD Foster, and A Foldvik. Low-frequency currents and continental shelf waves in the southern Weddell Sea. *Journal of physical oceanography*, 12(7):618–634, 1982.

[48] DE Cartwright. Extraordinary tidal currents near St Kilda. *Nature*, 223:928–932, 1969.

[49] DA Brooks and CNK Mooers. Wind-forced continental shelf waves in the Florida Current. *Journal of Geophysical Research*, 82(18):2569–2576, 1977.

[50] G Kaoullas and ER Johnson. Fast accurate computation of shelf waves for arbitrary depth profiles. *Continental Shelf Research*, 30(7):833–836, 2010.

[51] VT Buchwald and JK Adams. The propagation of continental shelf waves. In *Proceedings of the Royal Society of London A: Mathematical, Physical and Engineering Sciences*, volume 305, pages 235–250. The Royal Society, 1968.

[52] M Drivdal, JEH Weber, and JB Debernard. Dispersion Relation for Continental Shelf Waves When the Shallow Shelf Part Has an Arbitrary Width: Application to the Shelf West of Norway. *Journal of Physical Oceanography*, 46(2):537–549, 2016.

[53] G Kaoullas and ER Johnson. Geographically localised shelf waves on curved coasts. *Continental Shelf Research*, 30(16):1753–1760, 2010.

[54] AE Gill and E H Schumann. The generation of long shelf waves by the wind. *Journal of Physical Oceanography*, 4(1):83–90, 1974.

[55] JH Middleton and A Cunningham. Wind-forced continental shelf waves from a geographical origin. *Continental Shelf Research*, 3(3):215–232, 1984.

[56] AE Gill and AJ Clarke. Wind-induced upwelling, coastal currents and sea-level changes. In *Deep Sea Research and Oceanographic Abstracts*, volume 21, pages 325–345. Elsevier, 1974.

[57] JM Huthnance. Circulation, exchange and water masses at the ocean margin: the role of physical processes at the shelf edge. *Progress in Oceanography*, 35(4):353–431, 1995.

[58] V Echevin, M Albert, Aurélie-Lévy, M Graco, O Aumont, A Piétri, and G Garric. Intraseasonal variability of nearshore productivity in the Northern Humboldt Current System: The role of coastal trapped waves. *Continental Shelf Research*, 73:14–30, 2014.

[59] JEH Weber and M Drivdal. Radiation stress and mean drift in continental shelf waves. *Continental Shelf Research*, 35:108–116, 2012.

[60] F Giorgi and P Lionello. Climate change projections for the mediterranean region. *Global and Planetary Change*, 63(2):90–104, 2008.

[61] MA Losada. Procesos de múltiple escala en la evolución de la línea de costa. 2007.

[62] U Ulbrich, P Lionello, D Belušic, J Jacobeit, P Knippertz, FG Kuglitsch, GC Leckebusch, J Luterbacher, M Maugeri, P Maheras, et al. Climate of the Mediterranean: synoptic patterns, temperature, precipitation, winds, and their extremes. 2012.

[63] R Pawlowicz, B Beardsley, and S Lentz. Classical tidal harmonic analysis including error estimates in MATLAB using T_TIDE. *Computers & Geosciences*, 28(8):929–937, 2002.

[64] DL Cutchin and RL Smith. Continental shelf waves: Low-frequency variations in sea level and currents over the Oregon continental shelf. *Journal of Physical Oceanography*, 3(1):73–82, 1973.

[65] HW Ou, RC Beardsley, D Mayer, WC Boicourt, and B Butman. An analysis of subtidal current fluctuations in the Middle Atlantic Bight. *Journal of Physical Oceanography*, 11(10):1383–1392, 1981.

[66] SY Kim. A statistical description on the wind-coherent responses of sea surface heights off the US West Coast. *Ocean Dynamics*, 64(1):29–46, 2014.

[67] H Hukuda and LA Mysak. On the damping of second-class trapped waves on a sloping beach. *Journal of Physical Oceanography*, 12(12):1527–1531, 1982.

[68] H Mitsudera and K Hanawa. Effects of bottom friction on continental shelf waves. *Continental Shelf Research*, 7(7):699–714, 1987.

[69] I Webster. Frictional continental shelf waves and the circulation response of a continental shelf to wind forcing. *Journal of physical oceanography*, 15(7):855–864, 1985.

[70] SB Power, JH Middleton, and RHJ Grimshaw. Frictionally modified continental shelf waves and the subinertial response to wind and deep-0cean forcing. *Journal of physical oceanography*, 19(10):1486–1506, 1989.

[71] SB Power, RHJ Grimshaw, and JH Middleton. Large-scale, low-frequency barotropic circulation on continental margins. *Journal of Physical Oceanography*, 20(5):769–785, 1990.

[72] WJ Schulz, RP Mied, and CM Snow. Continental shelf wave propagation in the Mid-Atlantic Bight: a general dispersion relation. *Journal of Physical Oceanography*, 42(4):558–568, 2012.

[73] LZ Sansón. Simple models of coastal-trapped waves based on the shape of the bottom topography. *Journal of Physical Oceanography*, 42(3):420–429, 2012.

[74] J Pedlosky. *Geophysical fluid dynamics*. Springer Science & Business Media, 2013.

[75] FK Ball. Edge waves in an ocean of finite depth. In *Deep Sea Research and Oceanographic Abstracts*, volume 14, pages 79–88. Elsevier, 1967.

[76] JS Bendat and AG Piersol. Random data analysis and measurement procedures, 1986.

[77] J Candela, R Castro, A Mascarenhas, CA Collins, et al. Effect of coastal-trapped waves and wind on currents and transport in the Gulf of California. *Journal of geophysical research*, pages 5123–5139, 2014.

[78] LA Mysak and BV Hamon. Low-frequency sea level behavior and continental shelf waves off North Carolina. *Journal of Geophysical Research*, 74(6):1397–1405, 1969.

[79] LH Koopmans. *The spectral analysis of time series*. Academic press, 1995.

[80] PH LeBlond and LA Mysak. *Waves in the Ocean*. Elsevier, 1981.

[81] Eo L Ince. Ordinary differential equations dover publications. *INC. New York*, 1956.

[82] T Sarhan, J García, M Vargas, JM Vargas, F Plaza, et al. Upwelling mechanisms in the northwestern Alborán Sea. *Journal of Marine Systems*, 23(4):317–331, 2000.

[83] J Ruiz, D Macías, MM Rincón, A Pascual, IA Catalán, and G Navarro. Recruiting at the edge: kinetic energy inhibits anchovy populations in the western Mediterranean. *PloS one*, 8(2):e55523, 2013.

[84] Jacques CJ Nihoul. *Hydrodynamics of semi-enclosed seas*. Elsevier, 2000.

[85] KH Brink and JS Allen. On the effect of bottom friction on barotropic motion over the continental shelf. 1978.

[86] GT Csanady. The arrested topographic wave. *Journal of Physical Oceanography*, 8(1):47–62, 1978.

[87] JH Middleton. Steady coastal circulation due to oceanic alongshore pressure gradients. *Journal of physical oceanography*, 17(5):604–612, 1987.

[88] FP Shepard. The underlying causes of submarine canyons. *Proceedings of the national academy of sciences*, 22(8):496–502, 1936.

[89] JM Spurgin. *Flow dynamics around downwelling submarine canyons*. PhD thesis, University of British Columbia, 2014.

[90] Susan E Allen. On subinertial flow in submarine canyons: Effect of geometry. *Journal of Geophysical Research*, 105(1):1285–1297, 2000.

[91] M Canals. *Estructura sedimentaria y evolucion morfologica del talud y el glacis del Golfo de Leon: fenomenos de desestabilizacion de la cobertera sedimentaria*. PhD thesis, Ph. D. thesis, Barcelona University, Barcelona, Spain, 1985.

[92] J Kämpf. On preconditioning of coastal upwelling in the eastern Great Australian Bight. *Journal of Geophysical Research: Oceans*, 115(C12), 2010.

[93] J Kämpf and H Fohrmann. Sediment-driven downslope flow in submarine canyons and channels: Three-dimensional numerical experiments. *Journal of physical oceanography*, 30(9):2302–2319, 2000.

[94] E Kunze, LK Rosenfeld, GS Carter, and MC Gregg. Internal waves in monterey submarine canyon. *Journal of Physical Oceanography*, 32(6):1890–1913, 2002.

[95] M Bruno, A Vázquez, J Gomez-Enri, JM Vargas, J García Lafuente, A Ruiz-Canavate, L Mariscal, and J Vidal. Observations of internal waves and associated mixing phenomena in the Portimao canyon area. *Deep Sea Research Part II: Topical Studies in Oceanography*, 53(11):1219–1240, 2006.

[96] DJ Wain, MC Gregg, MH Alford, R-C Lien, RA Hall, and GS Carter. Propagation and dissipation of the internal tide in upper Monterey canyon. *Journal of Geophysical Research: Oceans*, 118(10):4855–4877, 2013.

[97] BM Hickey. Coastal submarine canyons. *Topographic effects in the ocean*, pages 95–110, 1995.

[98] JM Klinck. Circulation near submarine canyons: A modeling study. *Journal of Geophysical Research: Oceans*, 101(C1):1211–1223, 1996.

[99] Z Zhao, MH Alford, RC Lien, MC Gregg, and GS Carter. Internal tides and mixing in a submarine canyon with time-varying stratification. *Journal of Physical Oceanography*, 42(12):2121–2142, 2012.

[100] Albert Palanques, Xavier Durrieu de Madron, Pere Puig, Joan Fabres, Jorge Guillén, Antoni Calafat, Miquel Canals, Serge Heussner, and Jerôme Bonnin. Suspended sediment fluxes and transport processes in the gulf of lions submarine canyons. the role of storms and dense water cascading. *Marine Geology*, 234(1):43–61, 2006.

[101] IH Lee, RC Lien, JT Liu, and W Chuang. Turbulent mixing and internal tides in Gaoping (Kaoping) submarine canyon, Taiwan. *Journal of Marine Systems*, 76(4):383–396, 2009.

[102] RA Hall and GS Carter. Internal tides in Monterey submarine canyon. *Journal of Physical Oceanography*, 41(1):186–204, 2011.

[103] SE Allen and BM Hickey. Dynamics of advection-driven upwelling over a shelf break submarine canyon. *Journal of Geophysical Research: Oceans*, 115(C8), 2010.

[104] AF Waterhouse, SE Allen, and AW Bowie. Upwelling flow dynamics in long canyons at low Rossby number. *Journal of Geophysical Research: Oceans*, 114(C5), 2009.

[105] TM Howatt and SE Allen. Impact of the continental shelf slope on upwelling through submarine canyons. *Journal of Geophysical Research: Oceans*, 118(10):5814–5828, 2013.

[106] J Kämpf. On the magnitude of upwelling fluxes in shelf-break canyons. *Continental Shelf Research*, 27(17):2211–2223, 2007.

[107] SE Allen, MS Dinniman, JM Klinck, DD Gorby, AJ Hewett, and BM Hickey. On vertical advection truncation errors in terrain-following numerical models: Comparison to a laboratory model for upwelling over submarine canyons. *Journal of Geophysical Research: Oceans*, 108(C1), 2003.

[108] N Pérenne, JW Lavelle, DC Smith IV, and DL Boyer. Impulsively Started Flow in a Submarine Canyon: Comparison of Results from Laboratory

and Numerical Models. *Journal of Atmospheric and Oceanic Technology*, 18(10):1698–1718, 2001.

[109] PK Kundu, JS Allen, and RL Smith. Modal decomposition of the velocity field near the Oregon coast. *Journal of Physical Oceanography*, 5(4):683–704, 1975.

[110] C Torrence and GP Compo. A practical guide to wavelet analysis. *Bulletin of the American Meteorological society*, 79(1):61–78, 1998.

[111] AE Gill. *Atmosphere-ocean dynamics*, volume 30. Academic press, 1982.

[112] JI Antonov, RA Locarnini, RA Boyer, AV Mishonov, and HE Garcia. World ocean atlas 2005. Vol. 2, Salinity. 2006.

[113] JP Xu and MA Noble. Currents in Monterey submarine canyon. *Journal of Geophysical Research: Oceans*, 114(C3), 2009.

[114] NC Swart, Susan E Allen, and BJW Greenan. Resonant amplification of subinertial tides in a submarine canyon. *Journal of Geophysical Research: Oceans (1978–2012)*, 116(C9), 2011.

[115] GA Cannon. Wind effects on currents observed in Juan de Fuca submarine canyon. *Journal of Physical Oceanography*, 2(3):281–285, 1972.

[116] HD Mclellan. *Elements of physical oceanography*. Pergamon Press, 2013.

[117] YH Wang, IH Lee, and JT Liu. Observation of internal tidal currents in the Kaoping Canyon off southwestern Taiwan. *Estuarine, Coastal and Shelf Science*, 80(1):153–160, 2008.

[118] TM El-Geziry and IG Bryden. The circulation pattern in the Mediterranean sea: issues for modeller consideration. *Journal of Operational Oceanography*, 3(2):39–46, 2010.

[119] N Skliris, G Lacroix, and S Djenidi. Effects of extreme meteorological conditions on coastal dynamics near a submarine canyon. *Continental Shelf Research*, 24(9):1033–1045, 2004.

[120] J Lighthill. *Waves in fluids*. Cambridge university press, 2001.

[121] A Valle-Levinson, AT Castro, GG de Velasco, and R Armas. Diurnal vertical motions over a seamount of the southern Gulf of California. *Journal of Marine Systems*, 50(1):61–77, 2004.

[122] L Ross, I Pérez-Santos, A Valle-Levinson, and W Schneider. Semidiurnal internal tides in a Patagonian fjord. *Progress in Oceanography*, 129:19–34, 2014.

[123] J Gonella. A rotary-component method for analysing meteorological and oceanographic vector time series. In *Deep Sea Research and Oceanographic Abstracts*, volume 19, pages 833–846. Elsevier, 1972.

[124] MM Flexas, DL Boyer, Juan Espino, MP, A Rubio, and JB Company. Circulation over a submarine canyon in the NW Mediterranean. *Journal of Geophysical Research: Oceans*, 113(C12), 2008.

[125] TM Joyce. On in situ calibration of shipboard ADCPs. *Journal of Atmospheric and Oceanic Technology*, 6(1):169–172, 1989.

[126] A Valle-Levinson and T Matsuno. Tidal and subtidal flow along a cross-shelf transect on the East China Sea. *Journal of oceanography*, 59(5):573–584, 2003.

[127] FS Hotchkiss and C Wunsch. Internal waves in Hudson Canyon with possible geological implications. *Deep Sea Research Part A. Oceanographic Research Papers*, 29(4):415–442, 1982.

[128] Hans VH. Internal wave–zooplankton interactions in the Alboran Sea (w-mediterranean). *Journal of Plankton Research*, 36(4):1124–1134, 2014.

[129] DL Boyer, AS Sommeria, VKC Pakala, SA Smirnov, and D Etling. The effects of boundary turbulence on canyon flows forced by periodic along-shelf currents. *Journal of physical oceanography*, 36(5):813–826, 2006.

[130] D G MacMynowski and E Tziperman. Testing and improving ENSO models by process using transfer functions. *Geophysical Research Letters*, 37(19), 2010.

[131] C Chatfield. The analysis of time series, 2004.

[132] CA Biltoft and ER P. Spectral coherence and the statistical significance of turbulent flux computations. *Journal of Atmospheric and Oceanic Technology*, 26(2):403–409, 2009.

[133] R ORY Thompson. Coherence significance levels. *Journal of the Atmospheric Sciences*, 36(10):2020–2021, 1979.

[134] A Hannachi. A primer for EOF analysis of climate data. *Department of Meteorology, University of Reading*, pages 1–33, 2004.